ALMA MATER STUDIORUM · UNIVERSITY OF BOLOGNA

School of Science
Department of Physics and Astronomy
Master Degree in Physics

Study and Characterization of Silicon Photomultiplier for the outer Time of Flight layer of the future ALICE 3 experiment

Supervisor:
Prof. Andrea Alici

Co-supervisor:
Dr. Bianca Sabiu

Submitted by:
Gaia Fabbri

Academic Year 2023/2024

Abstract

In this thesis, Silicon Photomultipliers (SiPMs) have been characterized for potential implementation in the future ALICE 3 experiment at the Large Hadron Collider (LHC), which will replace the current ALICE detector. ALICE 3 is an innovative experiment with a key focus on minimizing the material budget, as it will consist entirely of silicon, resulting in a highly lightweight structure. SiPM sensors are being studied for use in the outer Time Of Flight layer, where radiation levels are lower, and a time resolution of 20 ps is required. However, SiPMs are also excellent photon detectors, and their characterization involved both photon beam tests from a laser source and charged particle beam tests at CERN's Proton Synchrotron.

The preliminary analysis includes an estimation of the Dark Count Rate (DCR) and measurements of current and capacitance as a function of voltage. Time resolution was assessed using both a laser photon source in the laboratory and charged particles at CERN's beam facilities at different beam energies. Additionally, an initial attempt to integrate the sensors into the full electronic readout chain, comprising the LiROC (Lidar ReadOut Chip) front-end ASIC and picoTDC, is presented.

The analyzed sensors differed in the thickness of the resin cover (3 mm, 1.5 mm, 1 mm, or no resin) and the presence of a thin metal layer in the trenches isolating the Single-Photon Avalanche Diodes (SPADs) (NUV-HD standard vs. NUV-HD-MT). While the metal layer was expected to improve isolation, no significant reduction in DCR was observed, and the time resolution appeared to worsen compared to standard sensors. The time resolution obtained with the laser source was approximately 120 ps, while values as low as 40 ps were achieved with charged particles beams.

Introduction

ALICE 3 is the next-generation detector meant to replace the current ALICE experiment at the LHC in 2032, advancing the study of heavy-ion collisions. The primary goal of ALICE 3 is to build a nearly-massless detector, made from cylindrical silicon layers mounted on ultra-thin curved wafers. The use of Monolithic Active Pixel Sensors (MAPS) technology enables a low material budget (0.05% X_0 per layer) and the placement of ultra-thin particle sensors directly within the beam pipe. This approach dramatically improves vertexing and tracking capabilities, allowing the sensors to be positioned as close as 5 mm from the beam pipe, which enhances secondary vertex detection and the tracking of low transverse momentum charged particles. Additionally, ALICE 3 can handle the higher luminosities expected in Ar-Ar, Kr-Kr, and Pb-Pb collisions, outperforming the current generation of detectors in managing these conditions. This capability, combined with advanced photon and electron identification, allows for precise measurements of particles with extremely low transverse momentum, including those carrying charm and bottom quarks.

A crucial aspect of ALICE 3's design is its ability to identify charged particles over a large range of transverse momenta. TThe Time-Of-Flight (TOF) system plays a key role in this respect. The system foresees a barrel detector and forward disks, with the barrel detector divided in a inner and an outer layer. However, the physics objectives of the experiment and its compact size demand a time resolution for the TOF system of about 20 ps which is beyond the state-of-art of current silicon-based sensor technologies.

In this context, Silicon Photomultipliers (SiPMs) emerge as promising candidates for the outer TOF layer. Operating in Geiger mode, SiPMs have high internal gains, making them sensitive to single photons and highly effective as photodetectors. Moreover, thanks to a protective resin coating, these sensors can also detect charged particles through the Cherenkov photons emitted as the particles pass through the resin. However, they are unsuitable for use in the inner TOF layer due to their limited radiation tolerance. Their main drawback is the high Dark Count Rate (DCR), which worsens after irradiation, although this does not significantly degrade their time resolution. In this thesis work, measurements of the time resolution by means of a laser and with beams of charged particles of different types of SiPMs manufactured by FBK will be presented.

Contents

List of Figures

Chapter 1

The ALICE 3 experiment at the LHC

1.1 QGP formation and evolution

The goal of this section is to describe head-on collisions between two ultra-relativistic nuclei; each incident nucleus is a Lorentz contract disc which contains many coloured quarks and antiquarks, which are in turn sources of strong fields carrying colour charges. In high-energy heavy-ion collisions, the system has the maximum energy density as soon as the interaction occurs, leading the system far from equilibrium conditions. As a result, a system with a large energy density and entropy is obtained, in which quarks and gluons are so strongly coupled to each other that such a system behaves as a collective medium; it expands and flows as relativistic hydrodynamic fluid with a very low viscosity to entropy density ratio η/s. This state of matter is called Quark Gluon Plasma (QGP) ([1]-[3]) and its formation as a consequence of the collision is evident in picture 1.1.

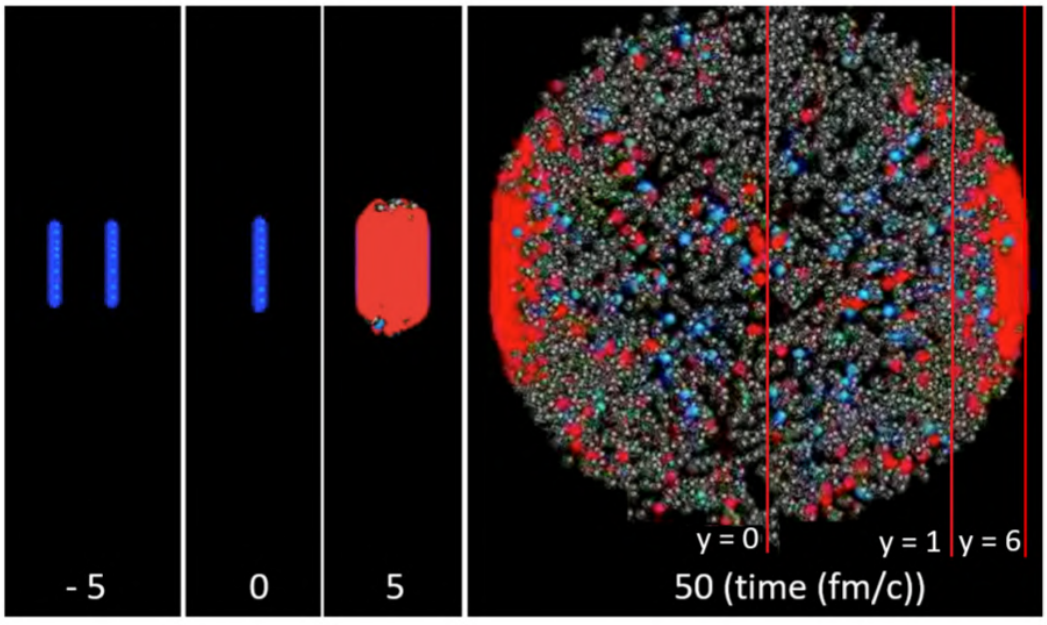

Figure 1.1: A schematic of heavy-ion collisions at different time, where blue and grey spheres are the hadrons colliding while the red ones indicate QGP. The hottest region are found at high rapidity value and the red lines indicate the regions of rapidity y = 0, y = 1, and y = 6, respectively.

The system continuous to expand, driven by a pressure gradient, acquiring a transverse velocity up to half the speed of light; while the system is cooling, partons sep-

arate. The inelastic interaction stops at the chemical freeze-out temperature $T_{chemical}$, when compositions are fixed; the only possible interaction remains elastic scattering until the kinetic freeze-out temperature T_{kin} is reached, which fixes the particles momenta. The result is a particle production mechanism involving the creation of an intermediate state of matter in which quarks and gluons are deconfined and highly interacting; such state is described by two parameters: the critical temperature T_c and the baryochemical potential $\mu_B = \frac{\partial}{\partial n_B} E$ where $n_B = n(B) - n(\bar{B})$ is the net baryon number. In reality, not all nuclei participate to the collision (nuclei do not collide are called spectators) and the not-central (peripheral) collisions are responsible for deviations from circular symmetry in the initial stage of GQP, together with fluctuations of incident nuclei: as a consequence, anisotropies in the pressure of the hydrodynamic fluid emerge, resulting in anisotropies in the expansion velocity and thus in the azimuthal momentum distributions of final products.

To conclude, it is worth to underline the importance of hard collisions between two partons in the incident nuclei carrying an high transverse momentum; high-energy partons are produced, evolve and then radiate, producing in turn jet of hadrons, heavy $\bar{q}q$ pairs, but also high energetic photons and leptons; they are able to cross the QGP during its evolution phase, carrying in this way a lot of information on how partons interact with the medium.

1.1.1 Why do we study ultrarelativistic heavy-ion collisions?

The overarching answer is that studying ultrarelativistic heavy-ion collisions is a precious tool to deeply understand the particle productions in high-energy collisions in QCD. In the following, several reasons are presented, going beyond the mere understanding of collision dynamics.

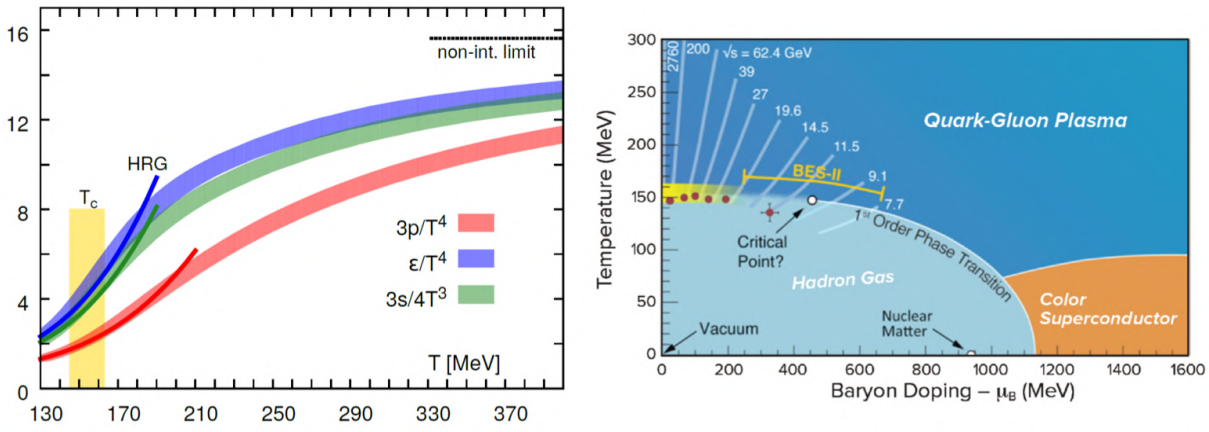

Figure 1.2: In the left picture are reported the lQCD calculations of the pressure p, the energy density ϵ and the entropy density s of the hot QCD medium at thermal equilibrium at temperature T. On the right picture, our current knowledge of the expected features of the phase diagram of QCD as a function of temperature and baryon doping, parametrized by the chemical potential μ_B.

1. **QCD in cosmology:** heavy-ion collisions are an effective tool to recreate the universe just after the Big Bang. At that time, the matter has a temperature above Λ_{QCD}[1] and every hadrons could be formed, so primordial matter existing at those temperatures should be of a different kind. One of the primary purposes of these

[1] the fundamental energy scale in QCD of the order of a few hundred MeV

collisions then is to recreate droplets of Big Bang matter in laboratory where we can learn about its material properties and its phase diagram in ways that we will never be able to do through observations made with telescopes or satellites. In picture 1.2 the rise in $\frac{\epsilon}{T}$ and $\frac{s}{T^3}$ is a manifestation of the transition between an hadron gas to QGP which has more degrees of freedom since partons are deconfined; it is also evident a continuous cross over [4], [5] at $T \approx 150\ MeV$ from a hadron resonance gas (HRG) at lower temperatures to QGP at higher temperatures.

2. **Phase diagram in QCD:** is represented as a function of baryon doping [2] and temperature (see picture 1.2); the baryon doping is parameterized by μ_B. At this point we set $\mu_B = 0$, meaning that our system as an equal number of quarks and antiquarks. This approximation works very well at RICH and LHC and represents well the early universe conditions; in all cases, hadronic matter is formed from the QGP expansion and cooling.

3. **Emergence of complex quantum number:** the QGP was the first complex form of matter that populates the primordial universe; however, at earlier times and at hotter temperature, the universe was filled by a weakly coupled plasma of quark and gluons. The liquid QGP can also be considered the simplest form of complex matter that gets closer to the fundamental lows governing matter in the universe. From that, it seems naturally explained the strongest motivation to develop experimental techniques to investigate the structure of liquid QGP at different scale.

1.2 Observables in heavy-ion collisions

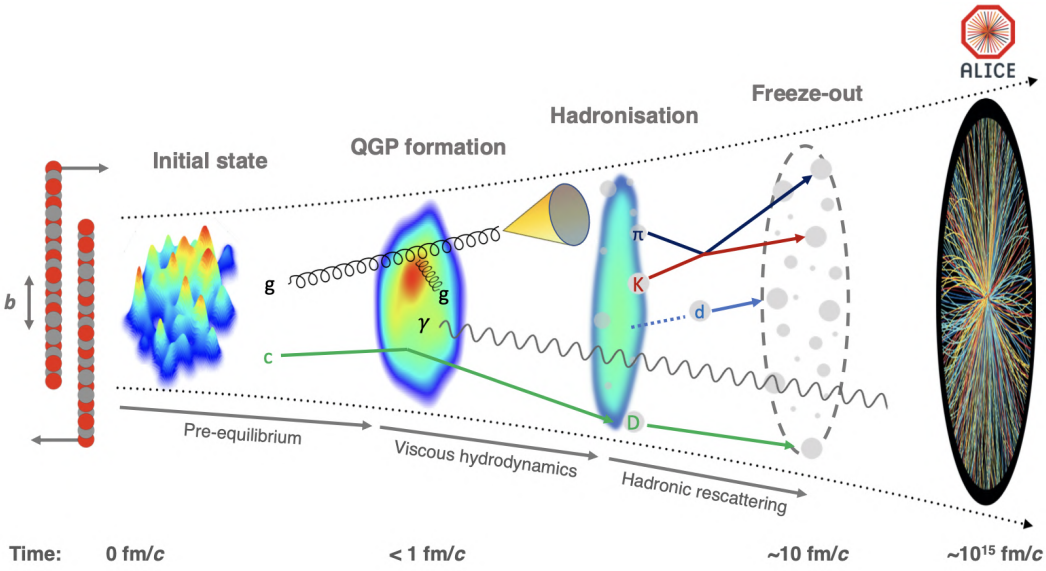

Figure 1.3: Different stages of evolution of the state created in heavy-ion collisions.

There are three main phases that needs to be investigated (see picture 1.3): the initial state (appendix), the QGP phase and the final hadronic phase (appendix); each

[2] or net baryon number density, the excess of quarks over antiquarks in the hot matter.

of them is characterized by different quantities. The Lorentz-invariant differential yield of final states[3] is, however, a fundamental quantity common to all the phases:

$$E\frac{d^3N}{dp^3} = \frac{1}{2\pi p_T}\frac{d^2N}{dp_T dy} \tag{1.2.1}$$

Different physical processes occur depending on the momentum range considered; we can therefore distinguish between low momentum where $p_T \lesssim 2\ GeV/c$, intermediate momentum for $2 \lesssim p_T \lesssim 8\ GeV/c$ and high momentum for $p_T \gtrsim 8\ GeV/c$.

1.2.1 QGP phase

The radial and anisotropic flow are sensible to the collective behaviour exhibited by the system; at low momenta, radial flow boosts massive particles to higher p_T so measuring the transverse momentum offers an idea of the amount of the radial flow in the system. The anisotropic flow indeed is analyzed via the azimuthal angular dependence of the transverse momentum vector:

$$\frac{dN}{d\phi} \propto 1 + 2\sum_{i=1}^{\infty}\nu_n \cdot cos(\phi - \Psi_n) \tag{1.2.2}$$

where ν_n are the anisotropic flow coefficients and are determined experimentally; the subscript "n" indicates the order of the anisotropic flow and Ψ_n is the angular direction of the anisotropic flow at the order of interest. For the major part of cases the ν_n of produced hadrons are different from zero indicating an hydrodynamic response of QGP.

Another useful tool is the nuclear modification factor R_{AA} which investigates hard probes produced in the earlier stages of the collisions. It is sensitive in changes in dynamics of hard processes in heavy-ion collisions when compared to elementary pp collisions. It is defined as:

$$R_{AA} = \frac{1}{\langle T_{AA}\rangle} \cdot \frac{dN_{AA}(p_T)/dp_T}{d\sigma_{PP}(p_T)/dp_T} \tag{1.2.3}$$

where $\langle T_{AA}\rangle$ is the average nuclear overlap function obtained by dividing the average number of colliding particle in the collision N_{coll} by the inelastic nucleon-nucleon cross section. If $R_{AA} = 1$ the production from heavy-ion collisions is considered an overlapping of many nucleon-nucleon collisions, assuming QGP does not form in pp collisions; every deviation from 1 indicates the presence of processes different from the pp case. In particular, $R_{AA} < 1$ is expected for inclusive hadrons at high p_T coming from partons undergoing energy loss. Jets are a very helpful tool in heavy-ion collisions as well, in particular for the angle-ordering phenomenon whereby hadrons with higher p_T in the shower are on average more aligned with the axis of the nominal jet. A fundamental parameter is the "jet radius" R, i.e. the size of the aperture by means the shower is seen; the measured jet yields is a way to determine R_{AA} while the dependence of the latter on R is a way to gain information about the medium modifications of the quark and gluon radiation patterns. Moreover, measuring ν_n at high p_T provides an insight on the path length dependence of the energy loss; high p_T partons lose less energy in the Ψ_n directions where the path is smaller, resulting in a larger abundance of hadrons in that direction and, in turn, non-zero values of ν_n. Differential measurements of R_{AA} and ν_n of heavy quarks gives access to different QGP features, since their corresponding hadrons are associated with the earliest stages. In particular:

[3] the number density of the particle three-momentum scaled by the particle energy E

- ν_n at low p_T represents the degree to which heavy quarks participate to the collective motions and approach thermalization;
- R_{AA} at high p_T gives information on the energy loss by heavy quarks, which is smaller for light quarks and gluons;
- for quarkonia, R_{AA} and ν_n allow to investigate suppression and regeneration processes, with the latter being favoured at low momenta due to larger quark multeplicity in the kinematic range.

1.3 An insight on QGP

1.3.1 Hydrodynamic properties

The QGP expands hydrodynamically and undergoes an hadronic rescattering phase which is proven by the flattering of transverse momentum distribution with increasing mass, especially at low p_T. In this region there is the overlapping between the thermal motion, which depends on the decoupling temperature, and of the collective flow, which pushes particles with a common velocity field so they acquire an additional transverse momentum proportional to their masses.

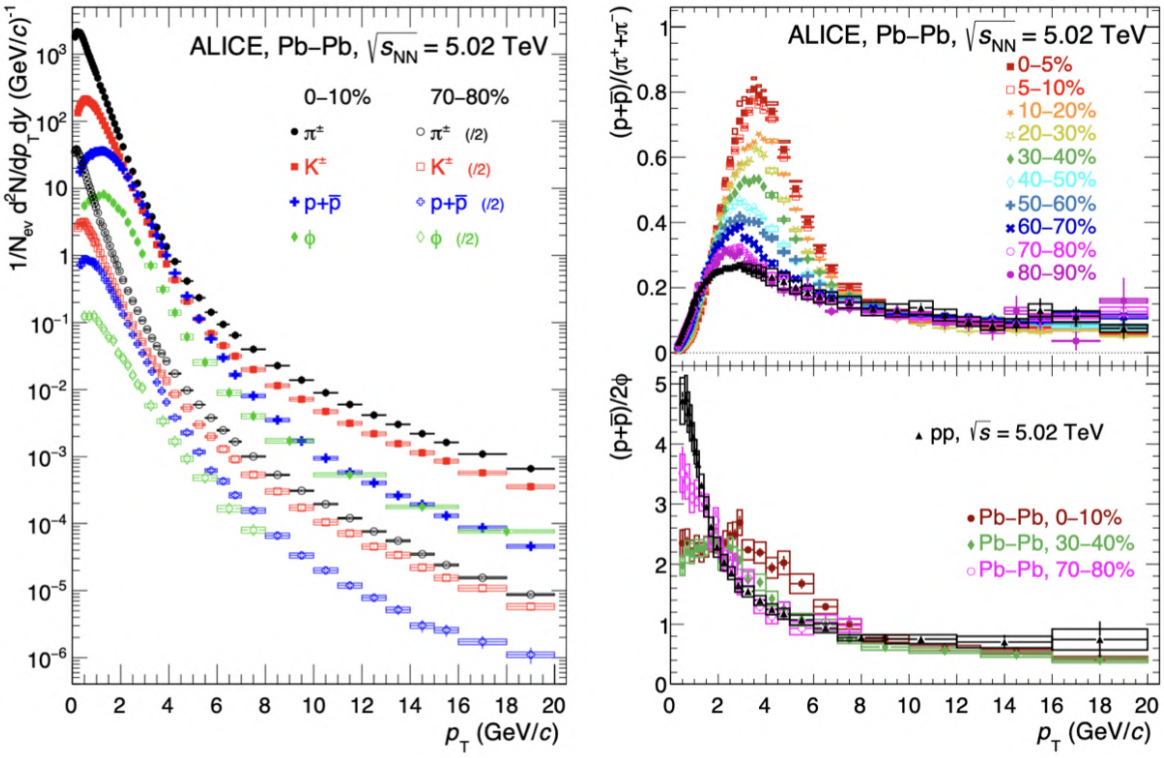

Figure 1.4: Transverse momentum distribution of π^+, K^+, p, K^0_s, Λ and ϕ in the centrality ranges of 0-5% and 80-90% in Pb-Pb collisions at $\sqrt{s_{NN}} = 2.76\ TeV$ (left). The kinetic freeze-out temperature T_{kin} as a function of the radial flow velocity βT according to Blast-Wave model. The values extracted take into account simultaneous fits to π, K and p spectra and ν_2 in Pb-Pb collisions (right).

The p_T spectra shown in figure 1.4 (left) are centrality dependent, with the maximum located at higher momenta for central collision; furthermore, the flattering of spectra in the low p_T region is more pronounced for more massive particle, which is in agreement

with the prediction of increasing radial flow with the collision centrality. The hadron spectra are studied throughout the Boltzmann-Gibbs Blast-Wave (BG-BW) parameterisation: particles are produced thermally in a medium which expands radially and is subject to an instantaneous kinetic freeze-out at T_{kin}. More complex approaches are taken into account to include the short-lived hadronic resonances that dominates the momentum range (BW FastReso) together with the anisotropic flow, focusing on the ν_2 for different particle species. In figure 1.4 (right) emerges that radial velocity seems to be quite unaffected by the choice of the BW parameterisation in more central collisions. The kinetic freeze-out temperature on the contrary depends strongly on the BW parameterisation; the BG-BW approach determines T_{kin} directly, while BW FastReso assumes the chemical and kinematic freeze-out temperatures, which in this way are kept as two different free parameters.

1.3.2 The statistical Hadronisation Model

The abundances of several hadron species containing light quarks were analysed, finding to be well described by the statistical hadronisation model (SHM), supporting the thermal particle production hypothesis. The parameters extracted from the model in Pb-Pb collisions at $\sqrt{s_{NN}} = 2.76\ TeV$ provide $T_{chem} \approx 156\ MeV$ and $\mu_B \approx 0$.

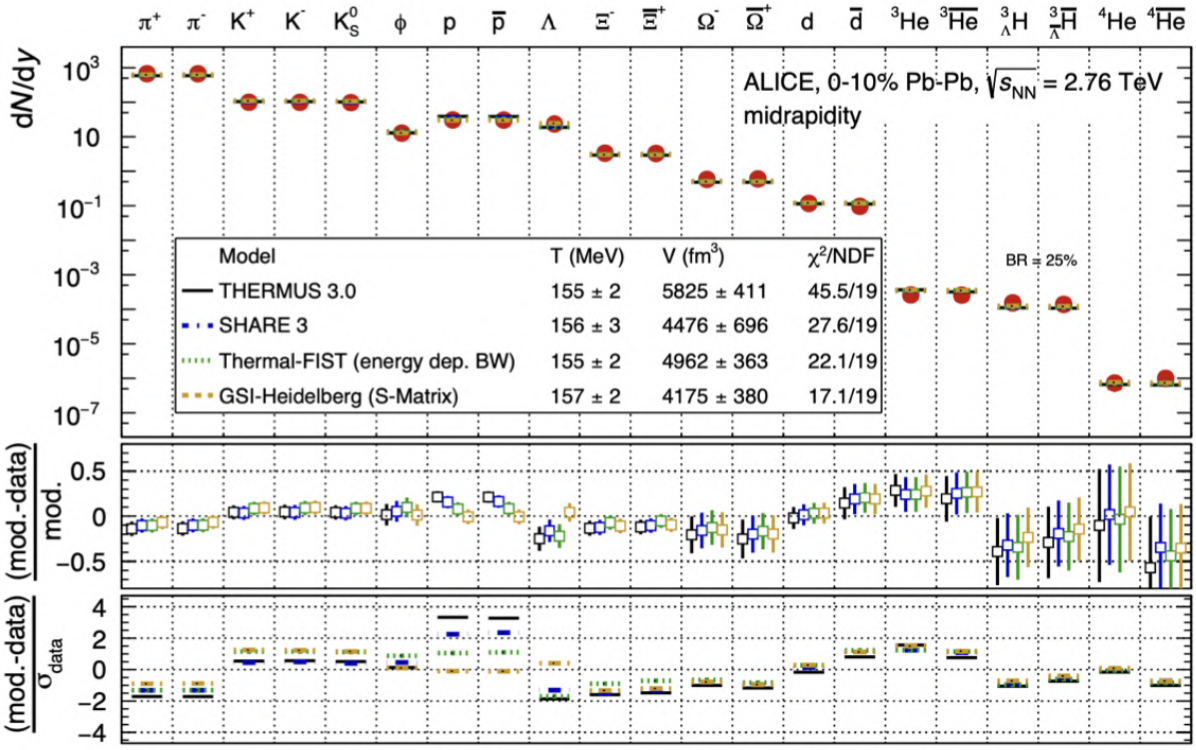

Figure 1.5: Measured multiplicity per unit of rapidity of different hadron species and light nuclei are displayed in the figure, compared to SHM model. In the bottom panel, the deviations between calculations and obtained yield are reported.

However, there are several aspects to deal with (figure 1.5):

- **the "snowball in hell" problem:** the binding energies of light nuclei are smaller than the temperature of the hadron gas at the chemical freeze-out so they should not survive the hadronisation phase. There are two possible explanation: the first assumes that nuclei are created and regenerate at the same rate ([6]-[8]), while

the second is based on the formation of compact colourless states that survive within a short hadronic phase [9];

- **the "proton yield anomaly"** consists in a significant disagreement between the measured p/π ratio and the one predicted by the SHM model, with the former larger than 25%. A possible explanations is the annihilation of baryons and antibaryons in the hadronic phase after chemical freeze-out [10] [11], or the presence of different particle eigenvolumes for different hadron types [12]; the latter is implemented in the Thermal-FIST model where an energy dependent Breit-Wigner scheme has been introduced to include effects of finite resonances width. Even if the results obtained in this way are the best possible up to now, a universal solution is not available yet;

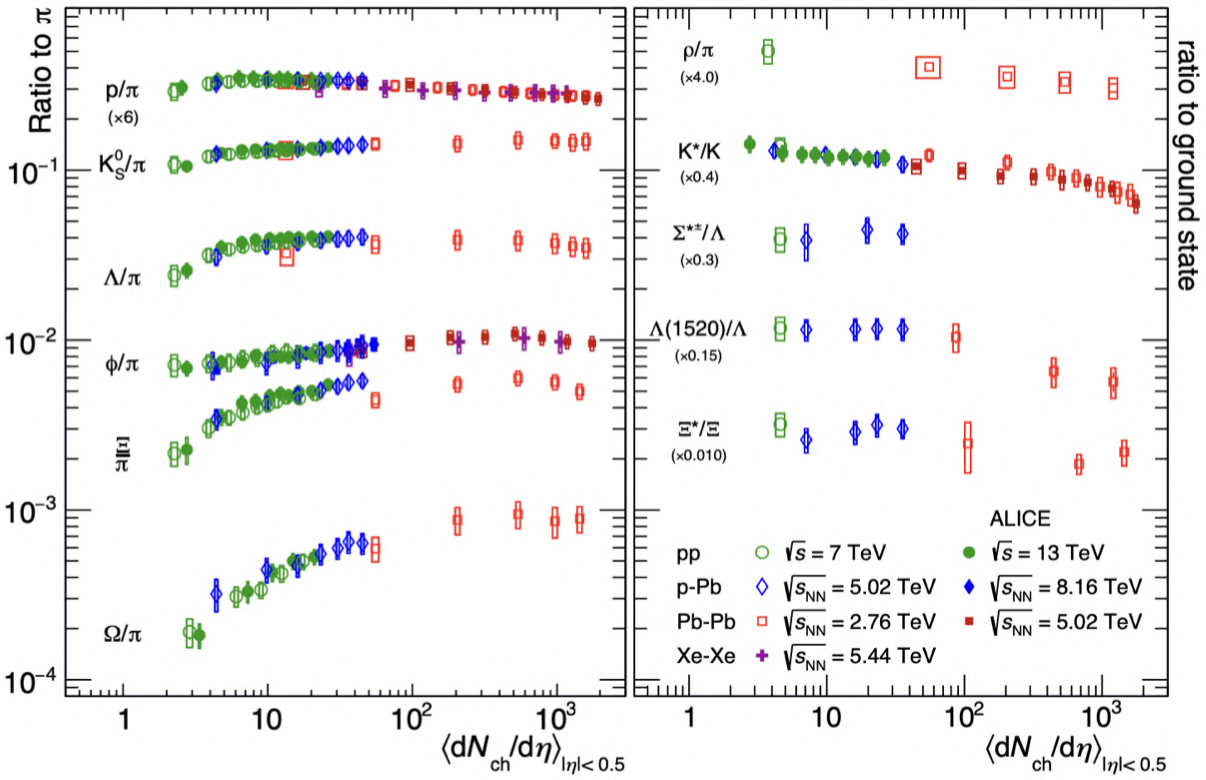

Figure 1.6: In the left panel the ratios of the different particles respect to pions are reported as a function of $\langle \frac{dN_{ch}}{d\eta} \rangle$ measured in $|\eta| < 0.5$ at different colliding energies and collision system. Similarly, in the right panel the ratios between resonances and the corresponding ground states are shown, all obtained at $|y| < 0.5$

- **strangeness enhancement:** The relative production rates of particles containing strange quarks is measured using Λ/π, Ξ/π and Ω/π ratios (figure 1.6), indicating a faster increase with multiplicity than hadrons containing only u and d quarks.This effect is more pronounced for hadrons with higher numbers of s quarks, such as Ω, while the ϕ meson, having hidden strangeness $s\bar{s}$, displays a growth that is halfway between the ones for Ξ^- and Λ. According to the PYTHIA pp event simulator, hadrons are produced as a consequence of incoherent break-up of colour flux tubes called "strings", which is not able alone to reproduce real data; it is necessary to include more complex physical processes as "colour-ropes"[4][13]. In term of SHM model, two ways are available:

[4]colour flux tubes with increased tension that are created when several strings overlap before hadro-

for pp-event, the canonical statistical model (including baryon number, electric charge and strangeness) is able to reproduce quite well the data observed; for ion collisions the passage to the grand-canonical limit occurs (the pp collisions represents the canonical limit, see [14] for more details) and in the deconfined state, light quark are expected to reach the equilibrium earlier, since less energy is needed to produce a $s\bar{s}$ pair. Moreover, the short equilibrium times of Λ, Ξ, Ω are compatible to an high density environment in which hadronic scattering play a relevant role, validating the grand-canonical model, seen as a natural consequence of QGP formation in the first stages of collisions.

1.3.3 The anistotropic flow coefficient

The p_T dependence of ν_2 for $\pi^{\pm}$, $K^{\pm}$, K^0_s, $p+\bar{p}$, $\Lambda+\bar{\Lambda}$ and ϕ [15] are reported in figure 1.7. It should be noted that:

- ν_2 is mass ordered due to a strong radial flow in the regime $p_T < 2-3\ GeV/c$;
- a grouping of baryon is observed at intermediate momenta in the range $3 \leq p_T \leq 8-10\ GeV/c$ consistently with hadronization via recombination.

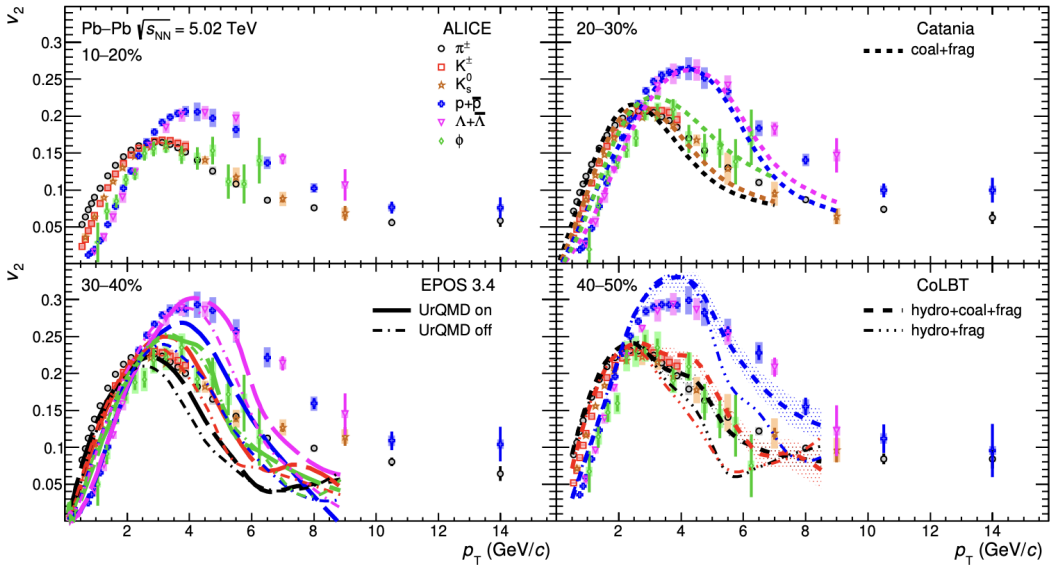

Figure 1.7: In the picture the p_T differential for ν_2 for several particle species in Pb-Pb collisions at $\sqrt{s_{NN}} = 5.02\ TeV$ for different centrality classes compared to simulations.

It is interesting to analyse the behaviour of ϕ mesons: at low momenta, they follow the behaviour of the proton, having a similar mass; at intermediate p_T the ν_2 value becomes similar to the mesons coefficient, since in this momentum range the elliptic flow depends mostly on the quark content. At high momenta ν_2 values are similar for different hadron species, indicating the dominance of fragmentation processes. The baryon grouping and ν_2 depending on p_T at intermediate momenta is explained by the recombination mechanism [16], [17]: in this picture, mesons M and baryons B reflects properties of their partonic constituents with an average momentum $\frac{p_T}{2}$ and $\frac{p_T}{3}$; the anisotropic coefficient is then given by the quarks one as $\nu_{2,M}(p_T) = 2\nu_{2,q}(\frac{p_T}{2})$ and $\nu_{2,B}(p_T) = 3\nu_{2,q}(\frac{p_T}{3})$, following that ν_2 reaches its maximum at higher momenta

nisation in high-multiplicity pp collisions

for baryons respect to mesons. After precise measurement at LHC, the scaling of the coefficient with the number of constituents quarks is extended to charm mesons and charmonia states.

1.3.4 Heavy-flavour hadrons

Charm and beauty quarks are not produced in chemical equilibrium within the plasma, since their masses are significantly larger than the temperature scale of the medium at LHC. However, SHM model is able to predict the yields of charm hadrons using as input the cross section of the initial hard-scattering processes [18]: the latter are the only source of production of charm and beauty quarks, which, once created, cross the medium exchanging energy and momentum with it. Such a cross section determines the number of charm quarks in the fireball and is based on charm conservation during the evolution: in this picture, charm quarks are to some extent thermalised in the QGP. Data collected in Pb-Pb collisions for the p_T differential yields of several charm hadrons show differences in the Λ_c/D^0 ratios with respect to pp collisions, although the same change is not observed in the integrated p_T ratio (fore more details, [19], [20], [21]-[24]). Such observation sufficiently agrees with expectations for hadrons produced via quark recombination, and the measured particle-yield ratios are parameterised by model including both recombination and fragmentation.

1.3.4.1 Charmonium regeneration

At the LHC energies, it is possible to further investigate the processes of charmonium states regeneration due to recombination of deconfined quark charms.

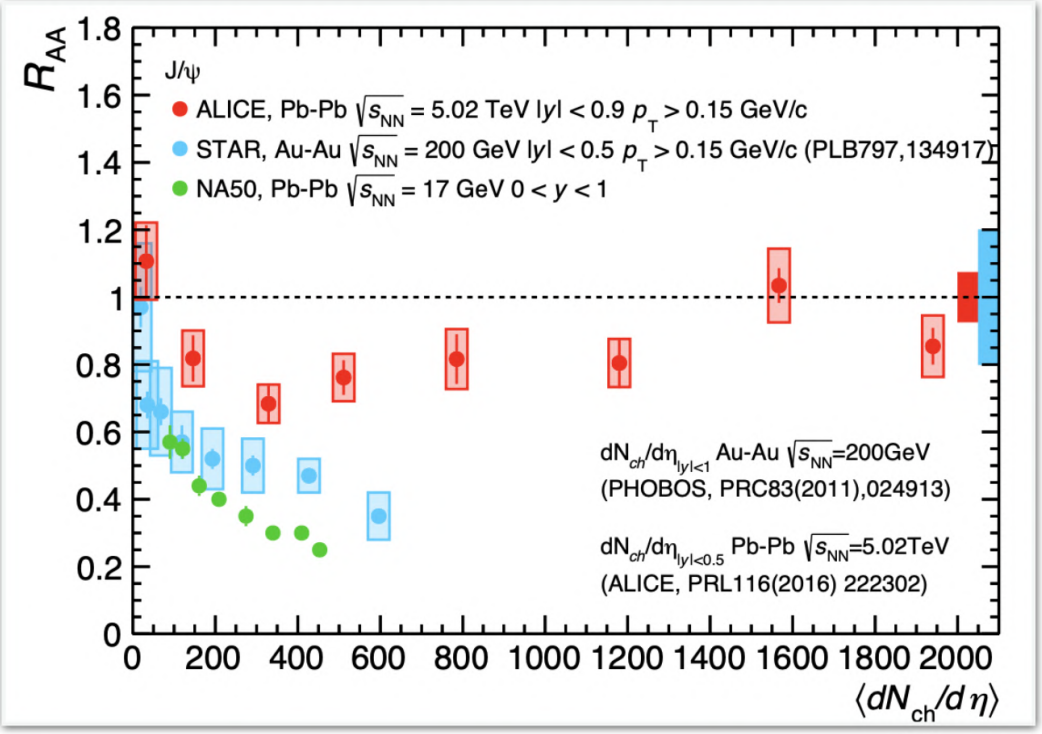

Figure 1.8: In the figure, the nuclear modification factor as a function of the charged hadron multiplicity is shown. For ALICE, the choice on $p_T > 0.15\ GeV/c$ minimizes the contribution of photoproduced J/Ψ.

Comparing ALICE results to the ones obtained at RICH and SPS with smaller energies (see [25] for more details), the J/Ψ suppression tends to reduce moving to higher energies, disappearing totally at LHC for central collisions; both effects indicates the presence of regeneration processes (figure 1.8).

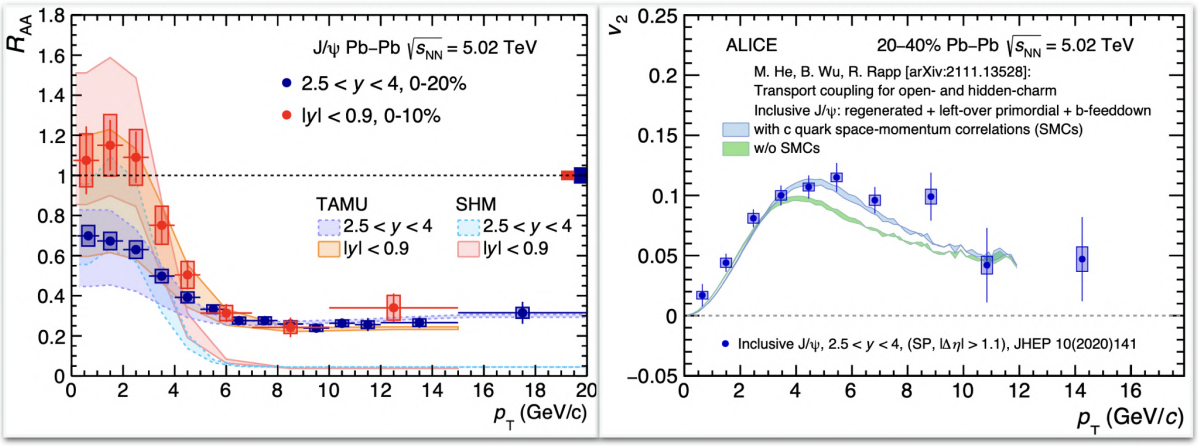

Figure 1.9: In the figure, the nuclear modification factor (left) and ν_2 (right) as a function of p_T are reported, together with the results of simulations.

A deeper analysis is provided by the p_T dependence of R_{AA} and ν_2 for the J/Ψ (figure 1.9): at low p_T the majority of charm quarks is produced and R_{AA} strongly increases; the effect is even more evident at midrapidity, since the regeneration mechanism is dominant at low momentum. On the other hand, at higher momenta R_{AA} is similar to the one observed for the other hadrons and the rapidity dependence is absent, probably due to parton energy loss. Finally, the larger ν_2 values obtained at $p_T \approx 5\ GeV/c$ in the centrality interval 20-40% suggest a larger J/Ψ production due to regeneration effects; the charm quarks, recombining, take their anisotropy in the collective expansion of the system.

1.3.5 The Jet Quenching Mechanism

When a parton has a momentum greater than few GeV/c, it evolves independently from other products of the same interactions, and the jet shower created propagates with the expanding and cooling medium. The "jet quenching mechanism" refers to the modification the shower undergoes, since its colour-charged constituents interact with the coloured component of the medium.

In figure 1.10 (left) the nuclear modification factor is shown as a function of p_T; for central Pb-Pb collisions, a peak is visible at intermediate momenta, probably due to the radial flow, while at high p_T a suppression of a factor 5 is observed. The R_{AA} behaviour shows a minimum for $p_T \approx 6\ GeV/c$, with a following increase which suggest that energy loss is constant [26], not depending on the parent parton energy. The same behaviour is observed for peripheral collisions, where the increase after the minimum reaches unity. Moreover, in figure 1.10(right) is shown R_{AA} for light-flavour mesons, protons ([34]) and isolated photons ([35]). It is immediately evident that the electroweak particles, which do not carry a colour charge, do not interact with the QGP medium [36]. Furthermore, the peak in the yields in the range $2 < p_T < 6\ GeV/c$ is most evident for protons, with a maximum value ordered according to mass, as we expect from the radial flux. For momenta greater than few GeV/c the formation of hadrons in jets is not

affected by the presence of the plasma, so the fact that all hadrons show the same energy loss for $p_T \geq 8\ GeV/c$ indicates that suppression acts at the partonic level.

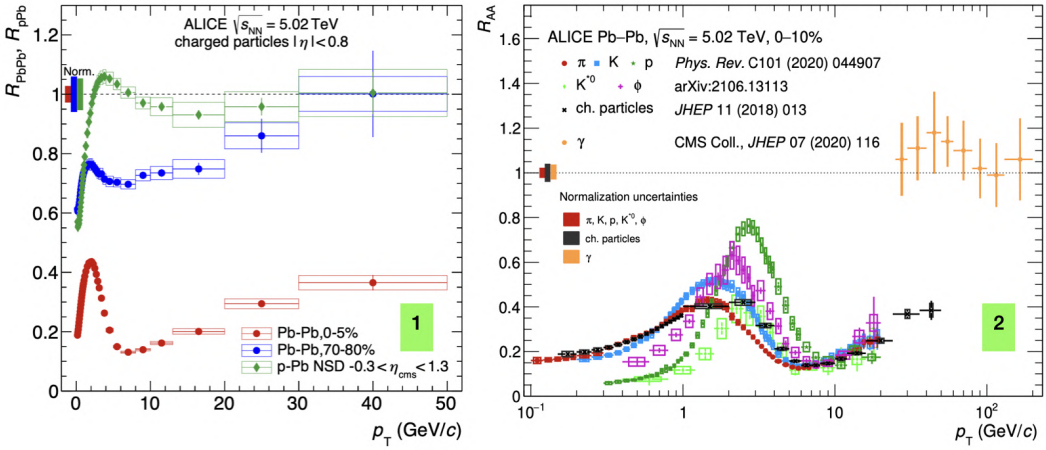

Figure 1.10: The nuclear modification factor R_{AA} in central and peripheral PbPb collisions and NSD pPb collisions (panel 1) and for different species of particles in central Pb-Pb collisions, where also isolated photons are included for the comparison.

1.4 ALICE 3

ALICE 3 [37] is an innovative experiment (see figure 1.11) that aims for excellent particle identification with a very low-mass tracking system and unique pointing resolution; it is meant as a major upgrade of the present ALICE experiment for LHC RUN 5 and 6 and will be installed at the LHC Interaction Point 2 (IP2) during the Long Shutdown 4.

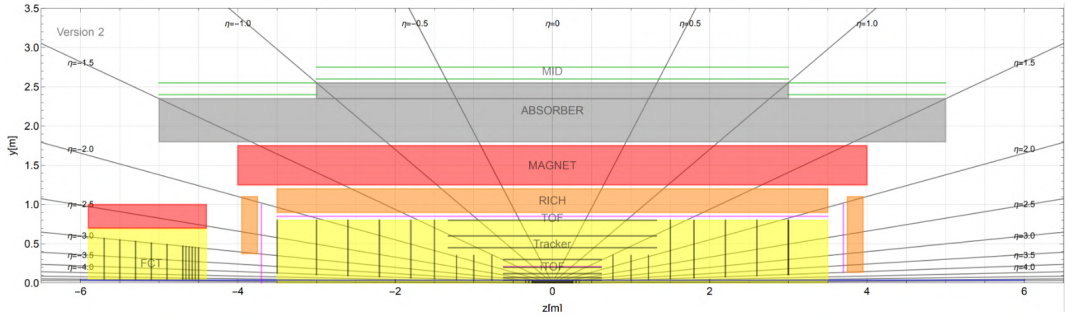

Figure 1.11: The figure shows the longitudinal cross section of the ALICE 3 detector; the tracker and the PID systems are housed in the filed of a superconducting magnet system. Moreover, the electromagnetic calorimeter ECAL, the muon system and the Forward Conversion Tracker (FCT) are visible,

The rapidity range covered is significantly increased with respect to the present ALICE experiment, providing additional tools for producing thermal dielectrons and heavy-flavour probes. In addition, cleanly investigating dielectrons over a wide range of p_T and masses provides a better understanding of temperature evolution in the initial phase of the collision, as well as unique access to evidence of chiral symmetry restoration. One of the new features of ALICE 3 is the retractable internal tracker that provides a unique pointing capability and enables the detection of heavy-flavour hadrons with high efficiency and purity even at very low momenta; among the high-precision measurements made possible for mesons and baryons containing charm and beauty, it is worth

noting the $D\bar{D}$ azimuthal correlation measurements that provide unique direct access to the interactions of heavy quarks with the QGP. In addition, the first layer of the vertex tracker is close enough to enable the highly efficient detection of weakly decaying strange baryons ('strangeness tracking') that are used in the detection of multi-charm baryons in heavy-ion collisions.

ALICE 3 is also capable of identifying muons with low transverse momentum over a unique range of p_T and is able to explore the formation and dissociation of exotic hadrons (as the $\chi_{c1}(3872)$) in heavy-ion collisions at thermal momentum scales. Moreover, other relevant features are:

- a great capability to identify nuclei and to look for super-nuclei;
- the particle identification based on the Time-of-Flight (TOF) and on the Ring Imaging Cherenkov (RICH) over a broad range of rapidity allows to investigate fluctuations in the net baryon number providing the dynamical effects of baryon numbers conservation together with information about QCD matter around the transition point;
- possibility to study also the physics beyond the Standard Model, as the presence of Axion-Like-Particles in ultra-peripheral collisions; the photon conversion layer proposed is a tool for very soft photons investigations, to explore new aspects of field theory in this regime.

1.4.1 Detector

1.4.1.1 Magnets and infrastructures

The ALICE detector is nowadays installed in the cavern of the L3 experiment at the time of LEP; the L3 magnet is a structural part of the cavern and is still used by ALICE, providing a solenoidal magnetic field of 0.5 T. Furthermore, a dipole magnet was added providing a field integral of $4\ mT$.

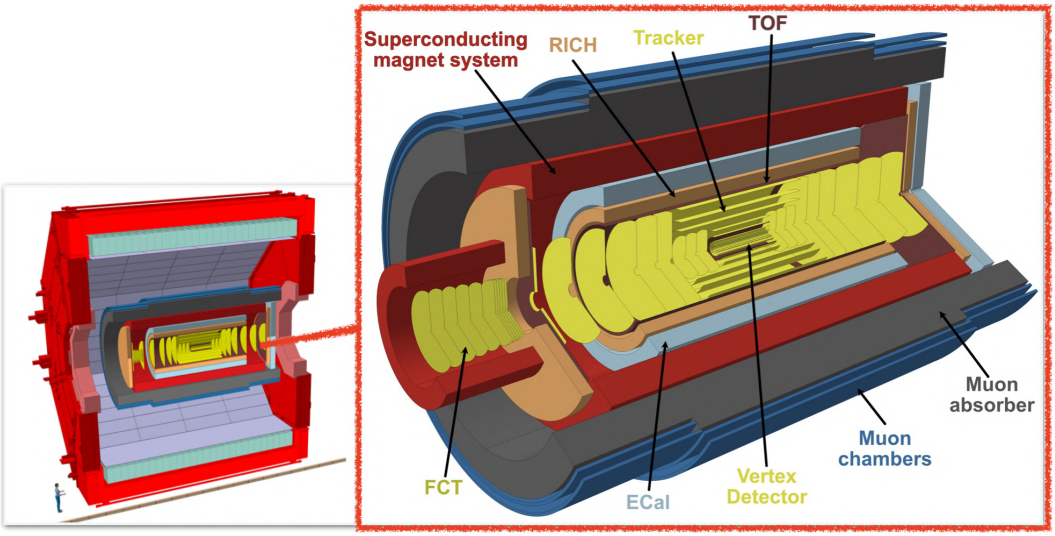

Figure 1.12: In the picture is reported the ALICE3 detector inside the L3 magnet yoke. The detector layout is represented with a solenoidal and a dipole integrated in the main magnet system.

To install the ALICE 3 detector (the layout is shown in figure 1.11), the previous configuration will be totally removed and only the L3 magnet yoke will be left in the

cavern; the latter will be used as a shield for the magnetic field towards the cavern, while a superconducting magnet will be placed in the volume of L3 magnet (figure 1.12).

1.4.1.2 Vertex detector and outer tracker

The detector design consists of 11 barrel layers and 2x12 forward discs, divided into a Vertex Tracker and an Outer Detector; the former includes the first 3 layers and 2x3 discs, retractably placed inside a secondary vacuum.

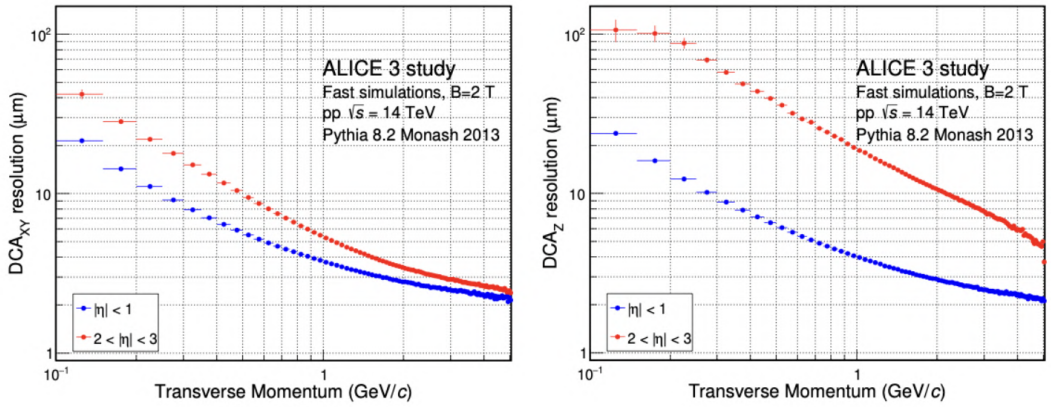

Figure 1.13: The impact parameter resolution is shown for a magnetic field B=2 T; the transverse (longitudinal) direction is shown in the left (right) panel.

The foreseen longitudinal and radial extension are, respectively, $\pm 400\ cm$ and $0.5 - 80\ cm$, in a pseudo-rapidity range of $|\eta| < 4$. The expected active surface will reach a value of $60\ m^2$, but including also peripheral coverage and hermeticity goal, a total amount of $66\ m^2$ of silicon will be used.

The expected performance for the resolution on the impact parameter is shown in figure 1.13 in the transverse (left) and longitudinal (right) directions for charged particles in pp collisions in a magnetic field of 2 T. There is a clear improvement, by about a factor of five, compared to the ITS3+TPC system for charged particles with $p_T \approx 500\ MeV$. A further comparison between ITS2, ITS3 and ALICE 3 is shown in figure 1.14 for a magnetic field of 1.5 T: for ALICE 3 the resolution improves by a factor of 10 compared to the performance of ITS3. For tracks with momenta up to 200 MeV/c, the resolution can reach values of less than 10 μm due to the very low material budget, and the value still remains lower than 100 μm for moments up to 0.1 GeV/c.

1.4.1.3 Specifications

The detector must be build according to some specifications:

- The radial distance of the first detection layer must be as close as possible to the interaction point, limited in turn by the aperture for the beam ($\approx 5\ mm$);
- Low material budget, since the vertex detector and the outer tracker aim to a thickness of 0.1 % and 1 % of a radiation length, respectively;
- The vertex detector and the outer tracker layers should provide an intrinsic position resolution of $2.5\ \mu m$ and $10\ \mu m$ respectively, corresponding to a pixel pitches of $10\ \mu m$ and $50\ \mu m$;

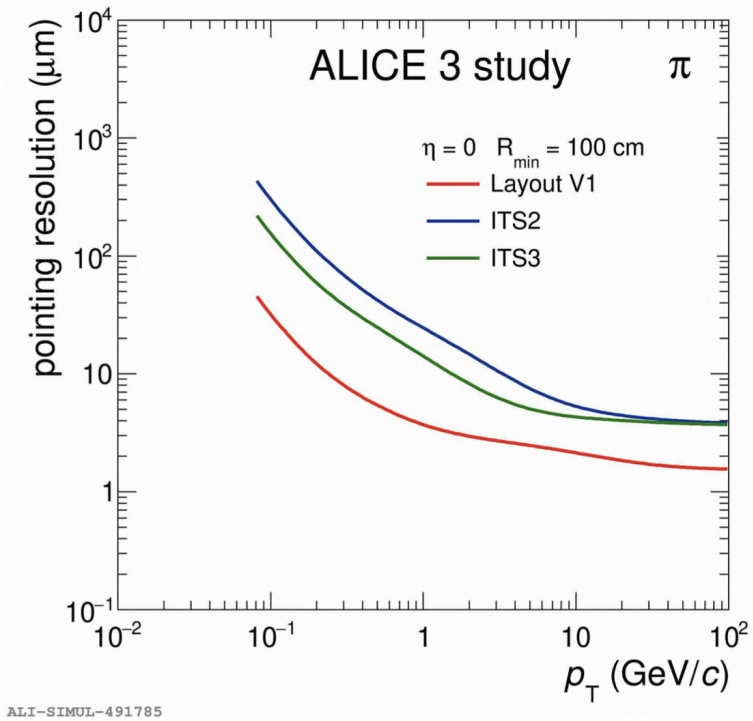

Figure 1.14: The pointing resolution for charged pion as a function of transverse momentum p_T for the IT of the ALICE 3 is compared to the ITS2 and ITS3 expected values in a magnetic filed of 0.5 T; a minimum track length of 1 m is requested.

- The time resolution expected from the sensors is $\approx 100\ ns$ in order to guarantee a time binning of $500\ ns$ in the vertex and outer tracker;
- The total data rate expected is $\approx\ 1\ Tbit\ s^{-1}$ considering an encoding with 2 bytes/hit and a fake hit rate of $\approx 10 - 8$ per pixel and event;
- The readout rate expected for sensors in the most exposed region of the vertex detector is $35\ MHz\ cm^{-2}$; in the outer tracker this value decreases down to $1 - 5\ kHz\ cm^{-2}$ in the most external layers;
- A power consumption below $70\ mW\ cm^{-2}$ and $20\ mW\ cm^{-2}$ for the vertex detector and for the outer tracker, respectively, is needed in order to keep the material thickness within the criteria;
- The maximum radiation load per operational year is $1.5 \cdot 10^{15}\ 1\ MeV\ n_{eq}/cm^2$ at a radial distance of 5 mm from the interaction point.

An ultra-thin layer as close as possible to the interaction point is a fundamental requirement to improve the pointing resolution:

$$\sigma_{DCA} \propto \frac{r_0}{p} \cdot \sqrt{\frac{\chi}{\chi_0} cosh\eta} \tag{1.4.1}$$

The retractable design is pushed by the need of an higher aperture at the injection energy, so it constitutes the only way to get 5 mm far from the beam.

1.4.1.4 The Vertex Detector

The proposed design consists in 4 petals (see figure 1.15) which can simultaneously rotate and close, like in an iris optic diaphragm, leaving a minimum distance of 10 mm of diameter for the beam passage; each of them hosts a quarter of detector with the first detection layer at a minimum distances of 5 mm from the beam axis in the closed configuration.

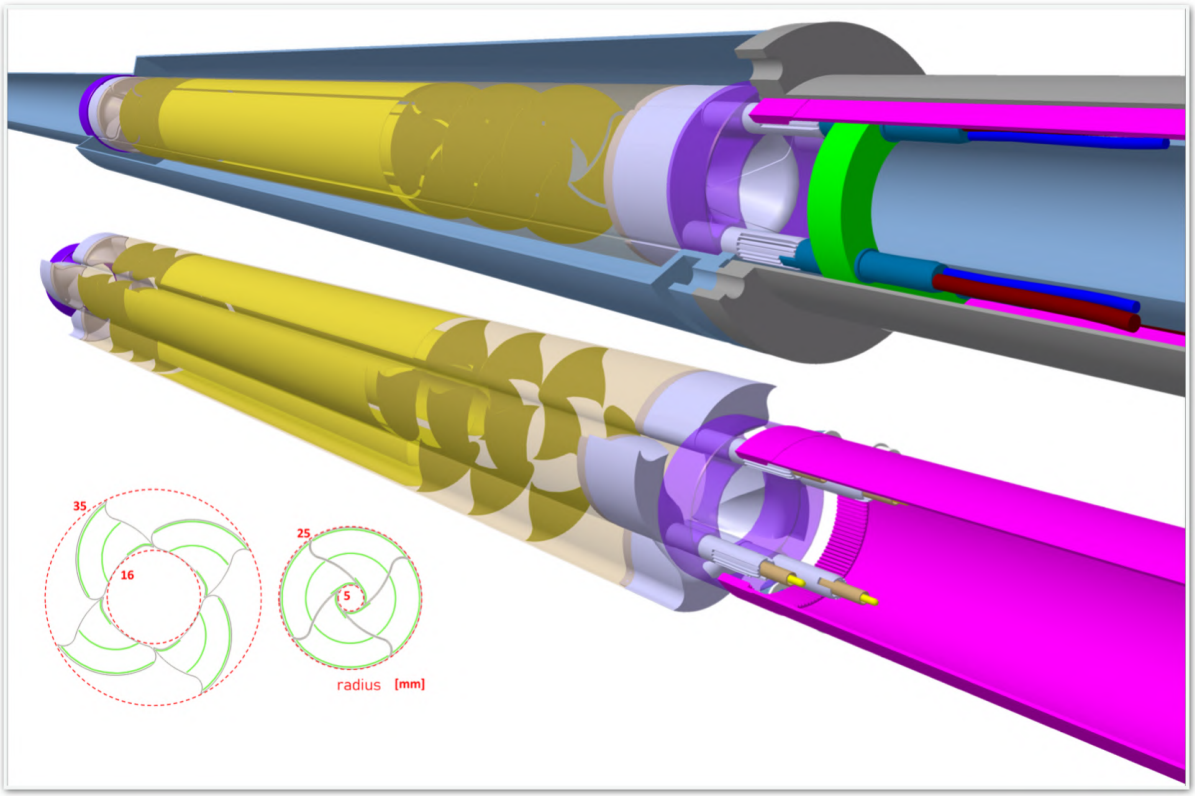

Figure 1.15: In the picture are reported the iris tracker configuration with its component.

The petals are thought to achieve an almost closed round bore with a diameter of 32 mm and 10 mm when they are, respectively, open or close. The petal walls separate the detector from the primary LHC vacuum and their thickness must be minimized; the inner wall of the petals are RF foils which controls the electromagnetic field induced by the beam. The key parameters for operation stability are aperture, impedence and vacuum stability at the interaction point: in particular, the minimal beam pipe radius set the limit for the distance from the first layer. Typically the minimum radius is 18 mm, with a thickness of 0.18 mm, but ALICE 3 is texting the possibilities to achieve a minimum radius of 16 mm with a thickness of 0.5 mm.

Placing the innermost tracker layer directly inside the beam pipe vacuum is a second option to get closer to the interaction point; however, there are several critical aspects to deal with in the implementation of the iris tracker. To begin with, it must be retract from its physical position at every injection and at the end of every fill, in order to match the larger aperture needed at the injection energy. The iris tracker is contained in a secondary vacuum, separated from the first vacuum by a thin wall, in order to reduce gas contamination coming from detector components. This wall contributes individually for the most to the material budget and it is before the first point of measurement, so its thickness must be minimized; moreover, the design must include a response scheme to pressure increasing. Reducing the central opening diameter

at the interaction point however affects vacuum pressure and stability, due to particles beam hitting the surface. To deal with this effect, a NEG coating is used inside the beam pipe: it is a thin layer of titanium-zirconium-vanadium alloy and it is effective in removing all gases except of methane and noble gases, then took away by LHC pumps. Another challenge is the possibility to easily access and replace the iris system and its vacuum equipment; the foreseen complicated design relies on an airlock section limited by two gates valves to insert and extract the iris tracker through the beampipe. It requires particular attention to the interface between the secondary vacuum of the iris tracker and the first vacuum of the beampipe, as well to the connectivity of services as cooling.

1.4.1.5 The Outer tracker

The main structure (figure 1.16) is made by modules and support elements: each modules is composed by interconnected sensors bounded to a high thermal conductive substrate. There is a functional support of longitudinal staves and flat discs respectively in the central barrel section and in the forward region: each module relies on it, to ensure mechanical support, alignment, cooling and electrical connectivity.

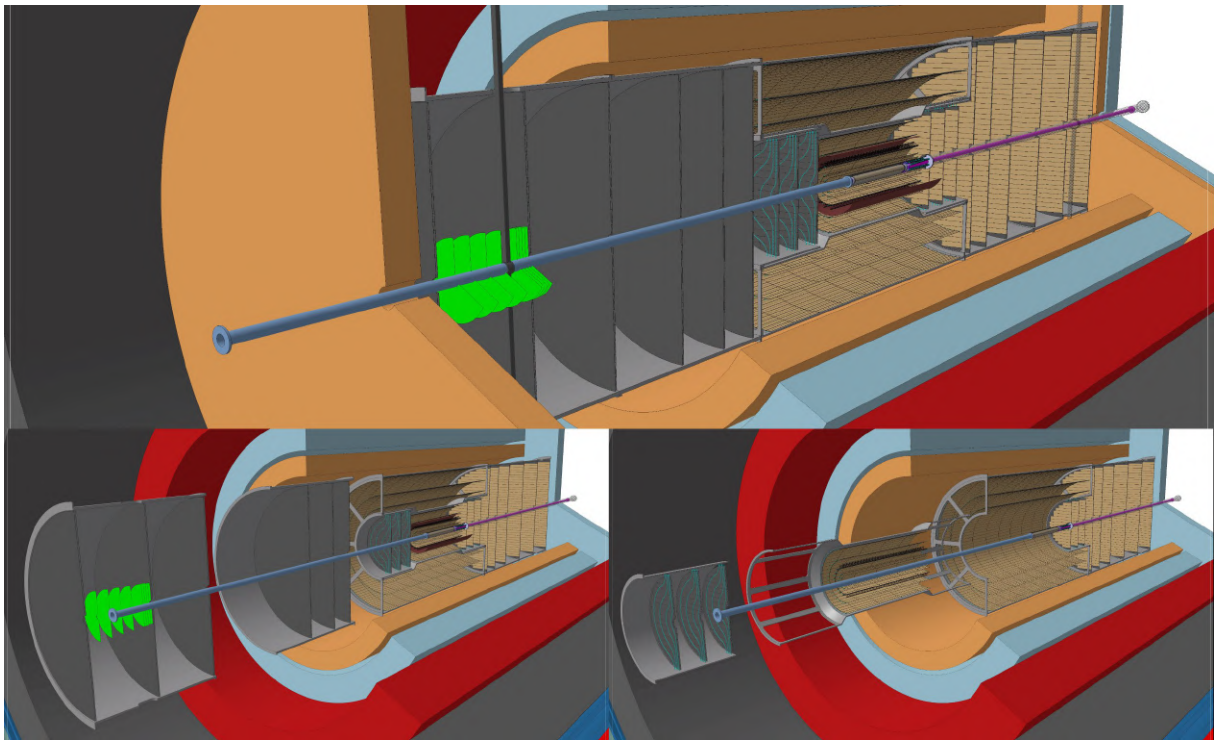

Figure 1.16: In the picture is shown the design for the outer tracker; modules assembled in staves structures should be noticed, together with services and power lines, but also the overlap of the staves is visible.

Staves and discs keep the position thanks to mechanical support structures with barrel-shape for an overall length of 8 m; the tracker is segmented into several barrels to ensure a sequential extraction from both sides of the detector. The discs of a given endcap are placed in the inner side of the so called Cylindrical Support Shell which makes possible to extract independently the different barrel sections and carries services in the cylindrical layers. The advantages of this component is to minimise the material between layers, since it offers support for the inner and outer barrel. In each

layer, the staves are fixed at both ends to the corresponding end-wheels, light composite end-rings that guarantee the positioning of the stave in the layer and provide the reference plane for the fixing of each extremity of the stave. To minimize the material budget, the sensors will be powered serially, then the modules are grouped in serial powering chains with a constant current source. Within each module, the individual front-end chips are supplied in parallel.

The main building blocks constituting the tracker are the modules and their supports of two different kinds: longitudinal staves for the modules in the central barrel and flat discs for the forward region. The staves are characterized by a carbon fibre spaceframe-like structure providing stiffness and positioning; the spaceframe keeps the coldplate positioned, consisting in layers of high-thermal conductivity carbon embodying polyimide cooling pipes. A similar structure is implemented for the discs, with the adding of a carbon sandwich panel that provides support and positioning. The module and the corresponding support are coupled at the level of the coldplate, relying on a precise system to check their relative position and on a dismountable interface for the mechanical connection. The thermal impedence is mitigated with a thermal interface material between the module substrate and the coldplate: in this way a single module of the tracker can be easily replaced or temporarily removed for repair.

1.4.1.6 The time of flight layer

The TOF system is composed by an inner and an outer layer in the central barrel and forward discs on both sides of the experiment with the main goal to provide particle identification over the full rapidity range $|\eta|< 4$. The more challenging requests are a time resolution of $20\ ps$, a low material budget of $1-3\%\ X_0$ and a power density of $50\ mW/cm^2$; silicon sensors seem to precious tools, with the request of creating large area systems, and several technology opportunities are under investigation. The TOF system is composed by several buiding blocks: the sensor, the front-end, the Time-to-Digital Converter (TDC), the clock management system and the readout system. To limit material budget and cost, one single layer of sensors is aimed, and the foreseen cell size for sensors that provide the correct matching for the track is $1\ mm^2$ for the inner TOF and $25\ mm^2$ for the outer TOF.

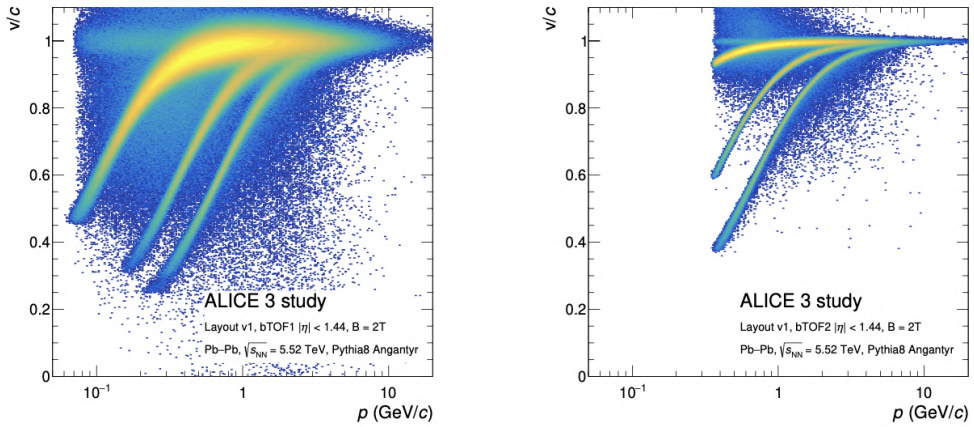

Figure 1.17: Particle velocity distribution as a function of momentum for Pb-Pb collisions at B=2 T for bTO1 (left) and bTOF2 (right). The effect of the improved momentum resolution together with the momentum thresholds for different particle species are evident in the figure.

Two layers of Time-Of-Flight detectors, named bTOF1 and bTOF2, are installed

at 19 cm and 85 cm from the beam pipe, respectively; they measure the arrival time of the particles with a resolution of 20 ps. Forward TOF walls with the same time resolution are located at 405 cm on either side of the interaction point. In particular, the combination of bTOF1 and bTOF2 allows the true time of flight to be measured and the start time to be accurately determined even with a small number of tracks. The results of the simulation of the response of the barrel TOF systems for Pb-Pb events with B=2 T are shown in figure 1.17; due to the higher occupancy, the false hit association is larger for the bTOF1 layer and thus the background for the track mismatch increases.

For what concerns sensors, there are three possible technologies proposed: fully depleted CMOS sensors, Low-Gain Avalanche Diodes (LGAD) and Single Photon Avalanche Diodes (SPAD). Starting from fully depleted CMOS sensors, the main goal is to reduce fabrication costs, getting at the same time easier and cheaper to assemble them with a 2D monolithic design which can provide both time resolution and complete coverage with just one layer. The more critical aspects is the necessity to improve significantly the current time resolution up to 20 ps, probably with the implementation of an internal gain layer. On the contrary, state-of-the-art LGADs reach a time resolution of 30 ps which is closer to the ALICE 3 requirements, and recently very thin LGAD has been pushed down to the value of 20 ps; however, they are produced in wafers and require a dedicated electronics, which increases significantly the fabrication costs and hardness the assembling procedure, making them only a secondary solution. Another option are SPADs manufactured in CMOS technology, which would also allows the readout of TOF and RICH to be merged; however, their use will only be considered if one decides to pursue this route, because the use of a single layer in this case is made more difficult by the presence of dark current and the evaluation of the fill factor[5]. It is worth noting that the choice of technology to be used does not place any constraints on the temperature along the TOF detector, and variations of a few degrees Celsius should not affect the temporal performance of the detector itself.

MAPS The most recent innovations in MAPS technology have focused on small cell size, noise reduction and low power consumption for tracking applications, while for timing their full potential is not yet known.

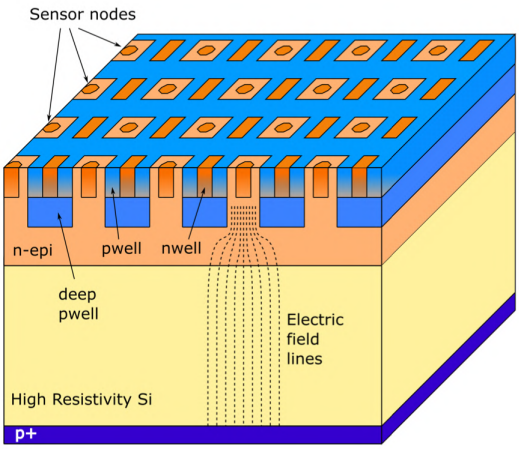

Figure 1.18: In the figure is reported a schematic view of the ARCADIA project sensor.

Good time performance requires a fast charge collection, and thus fully depleted

[5]Respectively, they are fake hits of sensor in absence of photon and the fraction of sensitive area over the total one

sensors, but also an optimised geometry and field configuration. The introduction of the gain layer has made it possible to increase the signal-to-noise ratio, and thus reduce the impact that noise has on time resolution. Different projects offer partially or fully depleted devices suitable for the aforementioned purpose: the FASTPIX project has analysed small pixels devices with the goal to model the field lines at the pixel border maximizing in this way the charge collection; the SEED and ARCADIA projects (figure 1.18) have implemented a n-type substrate with a surface n-type epitaxial layer and a buried p-well in a fully depleted device, to fasten charge collection and integrate electronics on the device. At the moment however, CMOS sensors do not achieve the aimed time resolution of 20 ps and it is doubtful whether this value can be obtained with devices without the internal gain layer, in order to reduce the electronic noise; CMOS integrated monolithic sensors with internal gain optimized for visible near infrared light has made their appearance, and the introduction of avalanche gain in the sensor substrate for timing applications is currently under discussion.

The pixel size is a trade off between a small sensor capacitance and the need to have enough area to host the electronics. The foreseen design is hierarchical, with every diode equipped with a front-end amplifier and discriminator. Larger macro-pixel are obtained overlapping the signal generated by the small pixels in a single data line.

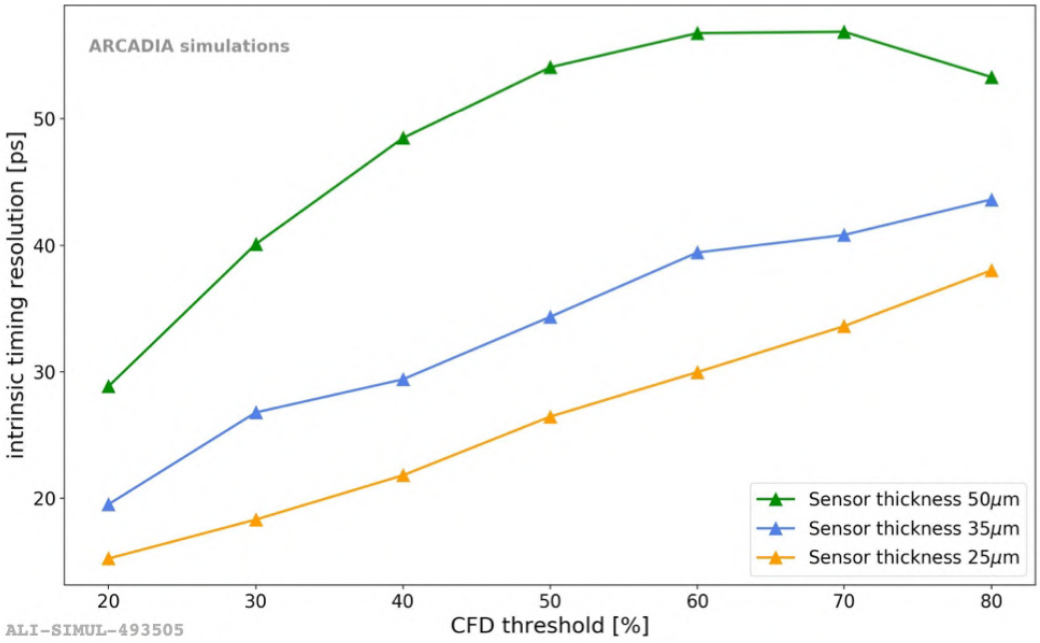

Figure 1.19: In the picture simulations of the time resolutions for 50 μm x 50 μm pixels with ARCADIA technology are reported; the pad size used in the simulation is 40 μm x 40 μm

A good time resolution requires uniform and fast charge collection, together with a very high Signal-to-Noise Ratio (SNR); the time performance of a fully depleted MAPS depends on the sensor thickness and on the collection electrode area: to thicker sensor corresponds larger signal, but the time resolutions worsens due to larger charge collection time. On the contrary, the electric field becomes more uniform increasing the sensor size, but also the capacitance increases, and the electronic noise grows accordingly. Several simulation are currently running in order to optimize the devices geometry in order to meet the strict timing requirement for the TOF layer: Monte Carlo simulations performed on 50 μm x 50 μm pixels with ARCADIA technology, with an active layer of 25 μm show that it is possible to achieve the aimed value of timing resolution of 20 ps, despite the presence of Landau fluctuations and non-saturated carrier

velocity (figure 1.19). However, a large power consumption is expected to obtain very low electronic noise, which nevertheless can be reduced introducing a moderate gain, of the order of 5-20. Strategies to include such a gain layer are thus under investigation, using dedicated implants or engineered substrates.

LGAD sensors Low Gain Avalanche Diodes are silicon detectors widely studied in the recent years, since they provide excellent timing performances and radiation hardness, being thus suitable for HEP experiment. The addition of a highly-doped p-layer near the p-n junction, the multiplication layer, creates and high field which results in an internal gain. The operative working range is below the breakdown voltage, reducing in this way cross-talk, dead time, dark count rate and with an easier segmentation; the optimum gain for a 50 μm thick LGAD is around 20-30. The time resolution seems to improve when the sensor thickness reduces, since the signal becomes shorter and Landau and gain fluctuations have less impact on the time resolution; however, whether the thickness reduces, the capacitance increases, a balance is therefore required between sensor capacity, internal gain and front-end power consumption. The time resolution improves when the threshold of a constant fraction discriminator (CFD) increases (figure 1.20), left) since the electronic noise contributions are less effective; simulations seem to confirm that LGAD with thinner active thickness have better timing performance (figure 1.20, right).

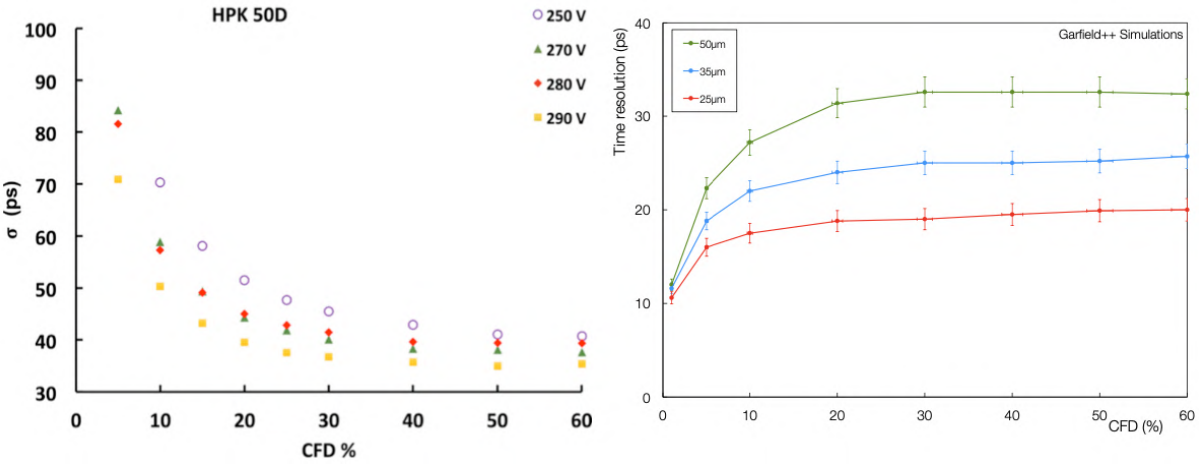

Figure 1.20: The test beam measurements of the time resolution of 50 μm LGADs from HPK (Hamamatsu Photonics K.K., Japan) for different voltages (left); simulation of the time resolution as a function of CFD for different thickness (right).

Another critical aspect that must be touched is the containment of the high electric field in order to avoid cross-talk or, eventually, breakdown. Deeply n-doped implants surround the gain layer to control lateral field components; however, geometric efficiency is reduced because lower-gain areas are present at the edges of the pad. However, the hypothesis of introducing shallow trenches into the silicon substrate with the termination implants inside the trench itself has recently been considered as an isolation strategy. However, another option still under study seems to be AC-coupled silicon resistive rectifiers (RSD or AC-LGAD). They are characterised by the presence of a thin resistive layer isolated from the readout pads on which the voltage is applied: at high frequency, this layer becomes transparent and the signal is induced directly on the pads themselves. Finally, the last critical aspect is radiation damage, which decreases charge collection efficiency, increases leakage current and changes the doping profiles

of the sensors by decreasing the gain in the amplification layer. Low temperatures reduce the impact of these effects ($\approx \ -30°C$) but this impacts costs and the material budget, which must be as low as possible. However, for the radiation levels expected at ALICE 3 these effects should be negligible, and consequently the sensors can be used at room temperature.

1.4.1.7 The RICH detector

Cherenkov radiation is a valuable tool for identifying particles in the region of transverse momenta that is not within the range of TOF; the range of p_T is determined by the refractive index, and using $n = 1.3$ ensures continuity in identification performance beyond TOF in the middle barrel; this is why aerogel is used as a radiator.

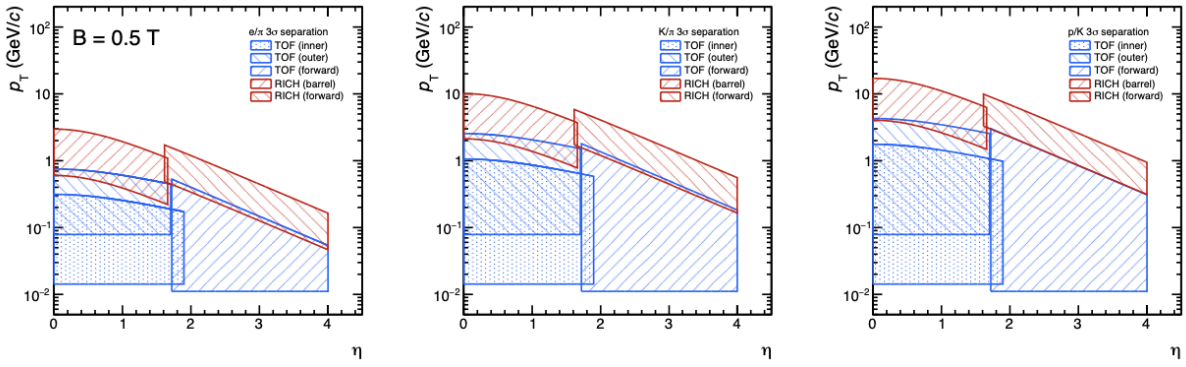

Figure 1.21: The calculated $\eta - p_T$ regions where particles can be separated by at least 3σ by the ALICE 3 particle identification subsystem in a 0.5 T magnetic field. From left to right, electron/pion, pion/kaon and kaon/proton separation plot are shown, respectively.

In figure 1.21 it is shown how RICH detector contribute to hadron identification, in particular providing e/π, π/K, K/p separation. In order to achieve adequate p_T coverage in the forward region, a smaller refractive index must be used due to Lorentz boost.

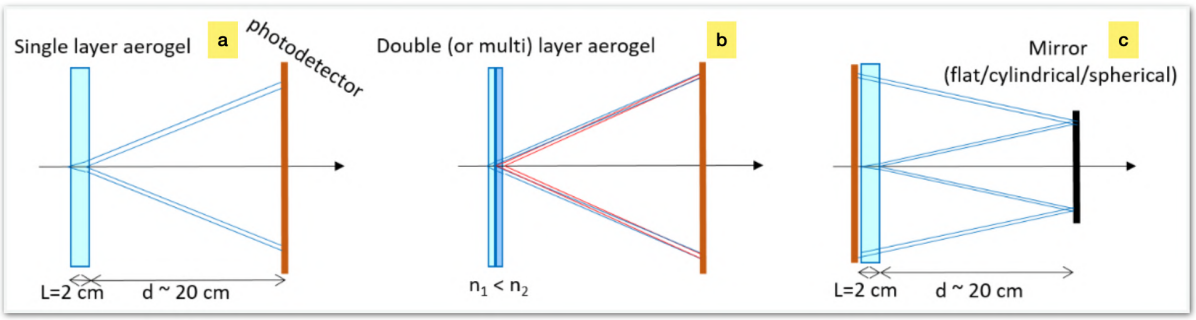

Figure 1.22: Schematic view of the aerogel RICH baseline layout (a), multi-layer aerogel layout (b) and mirror layout (c).

The aim of the detector is to extend the e/π separation up to $\approx 2\ GeV/c$ and the identification of charged hadrons up to $\approx 10\ GeV/c$: to do this, a 2 cm aerogel layer and a photodetector layer 20 cm from the radiator are to be implemented.

The large surface area, the Cherenkov angle required to achieve proper separation and the presence of a strong magnetic field guide the design of the sub-detector; the

separation capability depends on the angular resolution of the single photon $\sigma^{\gamma}_{\theta_c}$ and the number of photons detected N_{γ} as:

$$\sigma^{tot}_{\theta_c} = \frac{\sigma^{\gamma}_{\theta_c}}{\sqrt{N_{gamma}}} \bigoplus \sigma^{track}_{\theta_c} \tag{1.4.2}$$

$\sigma^{\gamma}_{\theta_c}$ is in turn influenced by several factors [6] and can be parameterised as:

$$\sigma^{\gamma}_{\theta_c} = \sigma^{chr}_{\theta_c} \bigoplus \sigma^{geo}_{\theta_c} \bigoplus \sigma^{pos}_{\theta_c} \bigoplus \sigma^{noise}_{\theta_c} \tag{1.4.3}$$

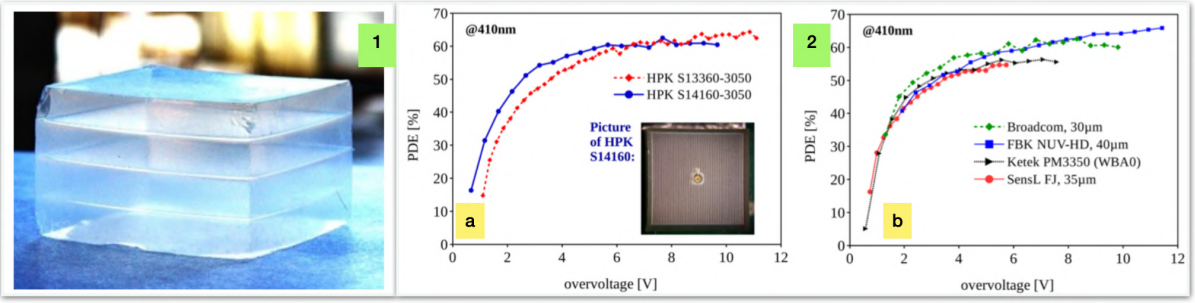

Figure 1.23: The figure shows a 4-layer monolithic aerogel (panel 1). Panel 2 shows the PDE as a function of over-voltage measured at 410 nm, for sensors from Hamamatsu (a) and other vendors (b).

Each contribution is estimated analytically and verified through simulations; it has been observed that increasing the gap d between the radiator and the photodetector improves geometric and pixel resolutions, while adding a mirror improves focus and geometric aberration. The basic configuration (see figure 1.22 panel a) consists of a 15 cm x 15 cm x 2 cm) hydrophobic aerogel tile radiator from Aerogel Factory Co. Ltd (Chiba, Japan); however, the angular resolution could be improved by inserting a multilayer radiator (figure 1.22 panel b) with 2 or 4 tiles of increasing refractive index (see figure 1.23 panel 1). In the latter case, the greater overall thickness of the radiator increases the number of Cherenkov photons, preventing the uncertainty at the point of emission from degrading the angular resolution of the individual photon. A further configuration (figure 1.22 panel c) involves the addition of a mirror on the outside of the aerogel layer, to reflect the Cherenkov radiation onto a detector located upstream of the radiator; while this solution leads to an improvement in angular resolution, decreasing geometric aberration, and a decrease in the photosensitive area to be covered, it also increases the difficulties in terms of mechanics and alignment, and is therefore still at the design stage. Photon sensors used for the detection of Cherenkov radiation must be sensitive to visible light, as aerogel is transparent in the visible range, but becomes opaque for wavelengths in the UV range. Silicon-based photon sensors seem to be a good option: based on the SPAD concept, we find the SiPM, the 2D silicon digital photomultiplier (2DdSiPM) and the 3D silicon digital photomultiplier. These devices, designed for detecting photons, are capable of excellent time performance; SiPMs in particular are characterised by a peak efficiency (PDE) of 60% in the visible (picture 1.23, panel 2) insensitivity to magnetic fields, compactness and can be integrated with active areas of up to 90%. SiPMs with integrated electronics made in a CMOS process may be able to mask hot cells and offer larger fill factors. The development of SiPMs is supported by several motivations:

[6] Respectively, from chromatic aberration, geometric aberration, spatial resolution and uncorrelated hits (noise)

- the rapid evolution of SPADs based on CMOS technology, which significantly reduces production costs;
- possibility of realising integrated circuits for time-gating logic and reducing DCR by masking hot cells;
- monolithic approach and integration of the electronics in the sensor itself decreases the material budget and simplifies integration, lowering production costs;
- possibility of building a customised sensor by optimising performance parameters (PDE, DCR and related noise, radiation tolerance).

Finally, using devices containing several SiPMs would facilitate the assembly of photodetector panels, also reducing dead area and improving connectivity.

Chapter 2

The solid state detectors

Solid-state detectors, based on semiconductor materials such as germanium and silicon, are widely used not only in high-energy physics (HEP) but also in medical and engineering fields, as they are very efficient in detecting photons and charged particles. What has made them the first choice in the field of HEP experiments is the wide availability of silicon, as well as the fact that they can also be used at room temperature. In this chapter, after a brief introduction on the physics of semiconductor materials and their interaction with various particles, the focus will fall on the Silicon Photomultipliers (SiPM), a device which is mainly used for photon detection. Through the description of its main characteristics and figures of merit, we will come to analyze the most innovative applications, that see the use of SiPMs themselves for the detection of charged particles without coupling them to scintillators or Cherenkov radiators.

2.1 The semiconductor materials

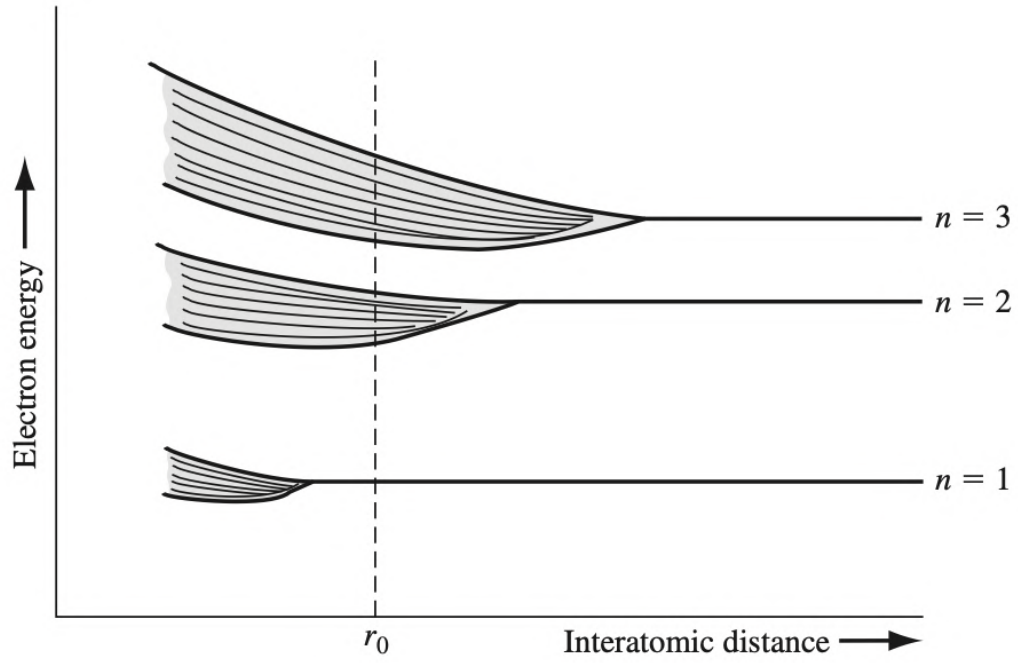

Figure 2.1: Typical band structure of a solid state material.

An energy band (figure 2.1)is defined as a set of energy levels so close together that

they are considered to be continuous: the valence band embodies lower energy levels and it is usually completely or partially filled at T=0K; the conduction band is made up of higher energy levels and is usually empty. They are separated by a gap of forbidden levels: in metals, the gap is absent, so the valence and conduction band overlap while in insulator materials, the gap is several eV wide so, even applying a strong electric field, electrons cannot jump from one band to the other. Semiconductors materials have a smaller energy gap respect to metals, of 1-3 eV, and at T=0 K the conduction band is empty, as in insulators; however, at T=300 K electrons can easily jump to the conduction band via thermal excitation, since the energy gap is only 1.12 eV. The different band structure of metals and semiconductor material is shown in figures 2.3 and 2.2.

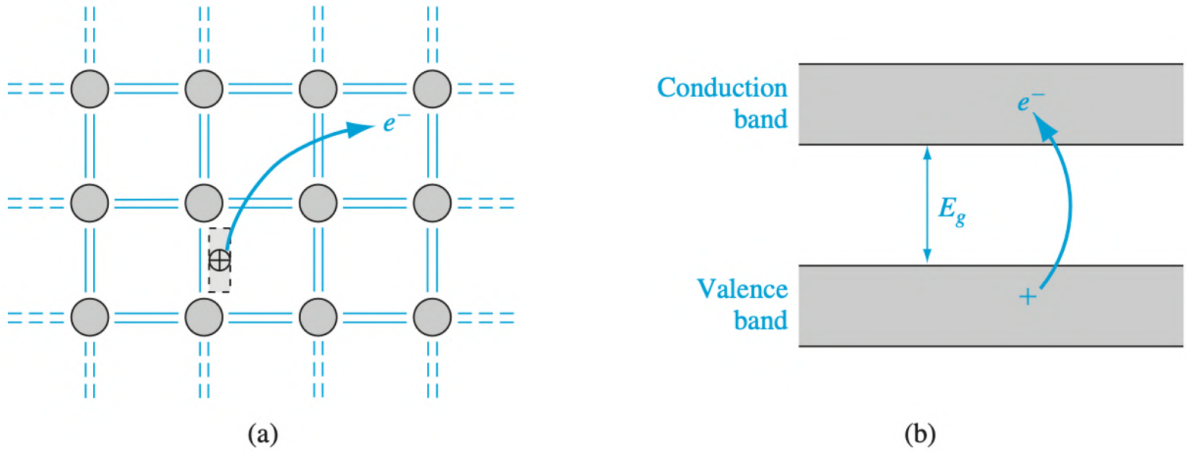

Figure 2.2: The figure shows the process of breaking of the covalent bonding (a), together with the band structure for a semiconductor (b); the jumping of an electron from the valence band to the conduction one is shown in the latter.

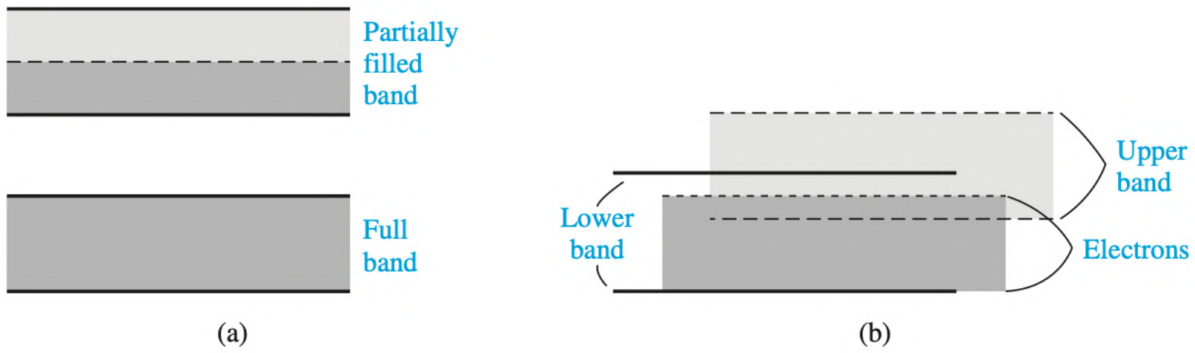

Figure 2.3: In the picture, the typical band structure for metals, where also the conduction bans is partially filled (a) or the two bands are overlapping (b).

However, they belong to the IV group, so they have four valence electrons available for the formation of four valence bonds: increasing the temperature, an electron is excited and jumps in the conduction band, leaving a hole (considered as positive charged) in the valence band. Therefore, applying an electric field, the semiconductor is crossed by a current which has two contributions: the electrons and the holes current. In pure (intrinsic) semiconductor electrons and holes are continuously created by thermal excitation, but they also recombine, creating an equilibrium situations in which

their concentrations n and p, respectively, are equal and called intrinsic concentrations of charged carriers n_i:

$$n_i = n = p = 1.45 \cdot 10^{10}\ cm^{-3} \tag{2.1.1}$$

for holes and electrons in thermal equilibrium at room temperature. The concentrations for holes and electrons are reported in equation 2.1.3:

$$n = N_C e^{-\frac{E_C - E_F}{kT}} \text{ where } N_C = 2(\frac{2\pi m_n^* kT}{h})^{3/2} \tag{2.1.2}$$

$$p = N_V e^{-\frac{E_F - E_V}{kT}} \text{ where } N_V = 2(\frac{2\pi m_p^* kT}{h})^{3/2} \tag{2.1.3}$$

where N_C and N_V are the effective densities of states in the conduction and valence band, respectively, E_F is the Fermi energy, E_C and E_V are the top and the bottom energy values of the conduction and valence band, m_p^* and m_n^* are the electrons and holes effective mass. Equation 2.1.1 becomes:

$$n_i^2 = n \cdot p = N - CN_V e^{-\frac{E_C - E_V}{kT}} = N - CN_V e^{-\frac{E_{gap}}{kT}} \tag{2.1.4}$$

The total hole and electron currents have to take into account drift and diffusion processes:

$$J_n = J_{n,drift} + J_{n,diff} = q(n\mu_n E + D_n \nabla n) \tag{2.1.5}$$

$$J_p = J_{p,drift} + J_{p,diff} = q(p\mu_p E - D_p \nabla p) \tag{2.1.6}$$

where μ_n and μ_p are electron and hole mobilties, where $\mu_n >> \mu_p$ (typically μ_n=1350 cm^2/Vs and μ_p=480 cm^2/Vs); they define the capabilities of charged carriers to move under the action of an electric field:

$$v_D = \mu E \tag{2.1.7}$$

The relation between the velocity and the E field is linear until the so called saturation conditions, at very high electric field, where the drift velocity becomes constant since the energy loss by collisions with the lattice atoms compensates the energy acquired; the saturated velocity is about $10^7\ cm/s$ for electric field of the order of $\approx$ 500 kV/cm. Moreover, the mobility depends also on temperature as T^{-m} where $m = 2.5$ for electrons and $M = 2.7$ for holes in Silicon. D_n and D_p are the diffusion coefficients for electrons and holes and typical values are 35 cm^{2}s^{-1} and 12.4 cm^{2}s^{-1}, respectively.

2.1.1 Extrinsic semiconductors

Usually pure semiconductors are doped with impurity atoms of the third (trivalent) or fifth (pentavalent) group which substitute Si or Ge atoms in the lattice, as the intrinsic concentration of charges is very small. The trivalent atoms lack of one electron to complete the four covalent bond with the neighbours, so they tend to capture an electron and are called acceptors; conversely, pentavalent atoms have one weakly bounded electrons not participating in the covalent bond so they tend to release these electrons, and are colled donors. These impurities introduce shallow energy levels in the gap very close to the valence and the conduction bands: at room temperature, electrons from the donor levels can easily jump into the conduction band, as well as the ones in the valence band can easily reach the acceptor levels, leaving a hole in the valence band. The conclusion is that at operational temperatures all acceptors and donors are

ionized, contributing with electrons and holes to the semiconductor conductivity: even if the dopants concentration is small ($10^{13} - 10^{16}$ atoms/cm^{-3}), it overcomes the intrinsic concentration of a factor $10^3 - 10^6$, contributing strongly in improving the material conductivity. Doping with donors creates an excess of electrons, called majority charge carriers, respect to holes (minority charge carriers), with an opposite effect when the doping atom is an acceptor (figures 2.4 and 2.5).

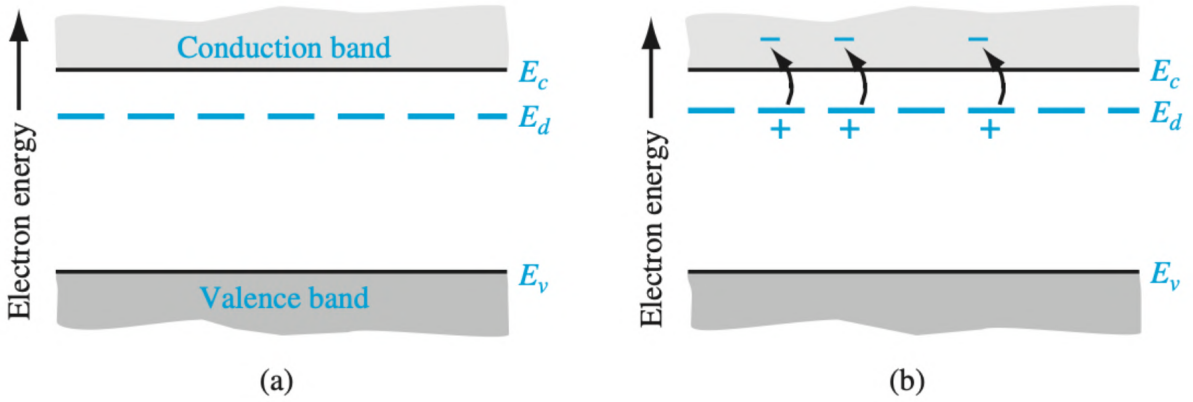

Figure 2.4: In the picture, the formation of donor energy levels below the conduction band (a) and electrons jumping toward the latter without creating holes in the valence band.

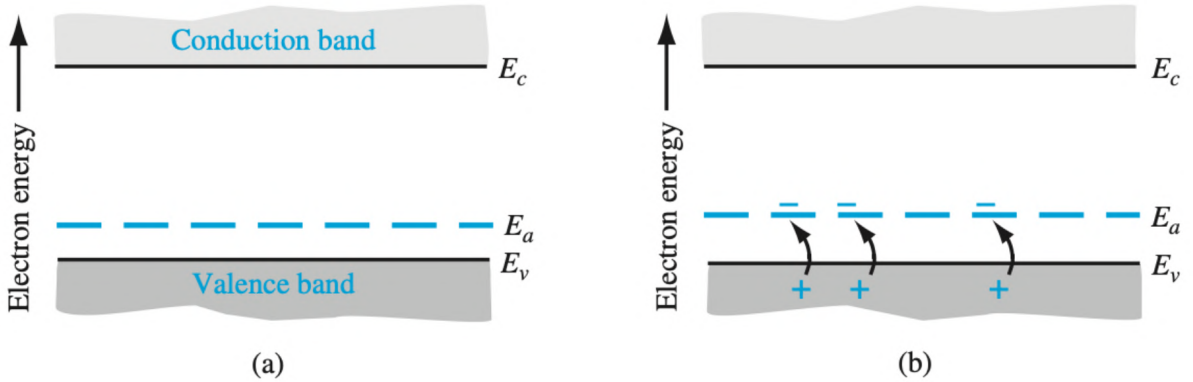

Figure 2.5: The picture shows the presence of acceptor energy level slightly above the valence band (a) and electrons jumping toward the former create holes in the valence band without populating the conduction one (b).

The equation 2.1.1 state that, for an intrinsic semiconductor, the concentration of electrons in the conduction band is equal to the concentration of holes in the valence band, and they are referred as intrinsic electrons/hole concentrations. However, adding dopant atoms, equation 2.1.1 is not true anymore, and we can express electrons and holes concentration in terms of intrinsic Fermi energy level as follows (equation 2.1.9)

$$n = n_i e^{\frac{E_F - E_F i}{kT}} \tag{2.1.8}$$

$$p = n_i e^{-\frac{E_F - E_F i}{kT}} \tag{2.1.9}$$

As the concentration changes from the intrinsic one, the Fermi energy also differs from the intrinsic Fermi level: in an n-type semiconductor, $E_F > E_F i$, so $n > p$, and

the opposite for a p-type semiconductor, which means that the Fermi level is above (below) the intrinsic Fermi energy for a n-semiconductor (p-semiconductor). In figure 2.6 the Fermi energy level is shown as a function of acceptor and donor concentration at $T \approx 300\ K$: as the doping concentration increases, the level of Fermi shifts close to the valence band for p-type material and close to the conduction band for n-type material. Since the intrinsic concentration is strongly dependent on temperature, the position of the Fermi level is also affected (figure 2.6): if the temperature increases, the intrinsic concentration n_i increases so the Fermi level tends to the intrinsic one. Therefore, the behavior of an extrinsic semiconductor tends to the intrinsic one at high temperatures. At very low temperatures, on the other hand, we encounter the freeze-out condition where the Fermi level goes above donor levels and below accessory levels, so that at absolute zero all levels below E_F are full and above it are empty.

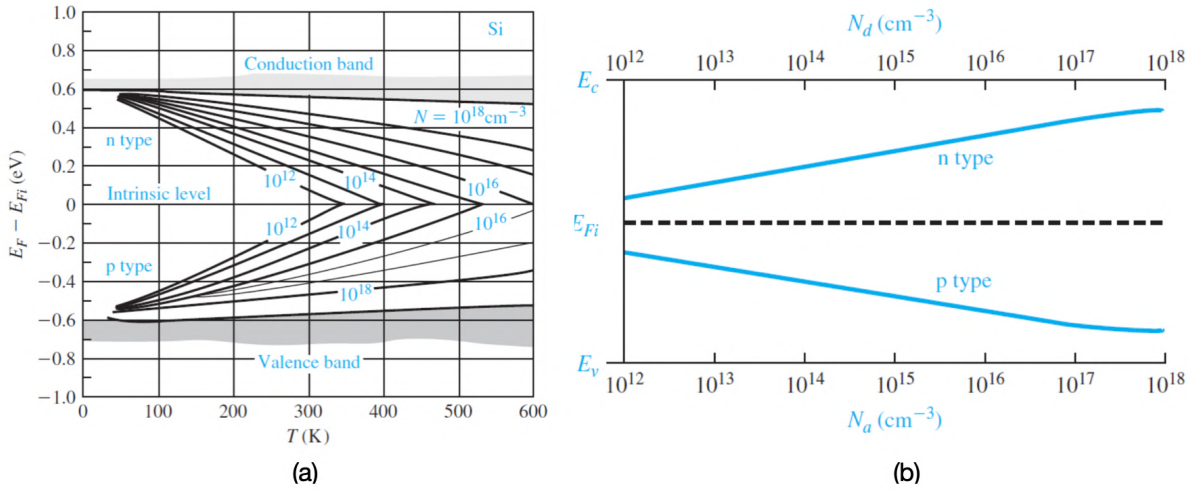

Figure 2.6: In the picture the Fermi level position is shown as a function of temperature (a) and doping concentration (b).

2.1.2 The pn jucntion:

When a p-doped region is contacted with an n-doped region, majorities charged carriers diffuse into the region with the lower concentration with the interface region populated by ionized donors and acceptors; an electric filed builds up and stops the diffusion and a depletion region arises at the junction, together with a potential difference V_{bi} (called contact potential or built-in) from the n-side, where positive ions are fixed in the lattice, to the p-side (fixed negative ions). The built-in potential is expressed by:

$$V_{bi} = \frac{kT}{e} ln(\frac{N_a \cdot N_d}{ni^2}) = V_T ln(\frac{N_a \cdot N_d}{n_i^2}) \tag{2.1.10}$$

where V_T is the thermal voltage, k is the Boltzmann constant, N_a and N_d are the donor and acceptor concentration, respectively and n_i is the intrinsic concentration. In figure 2.7 the positive and negative charged region are shown: all electrons and holes are swept away from the depletion region by the electric field; however, a density gradient is still present in the majority carrier concentrations [1] at each edge of the space charge

[1] Majority carriers are electrons in n-doped semiconductor and holes for p-doped ones

region and it produces a diffusion force on majority charge carriers. At thermal equilibrium, the electric and diffusion forces are exactly balanced and the Fermi energy level is constant throughout the junction, so the conduction and valence band have to bend inside the depletion region. The junction is called to be in forward bias when the voltage is applied with the anode on the p side and the cathode on the n side: the potential barrier is lowered and a net current of electrons and holes flows through the junction, so that the depletion region becomes smaller. Reversing the polarity results in reverse bias junction, in which the charges are moved away from the depletion region and only a very small current, called the saturation current, flows over the junction. However, there is a voltage for which the reverse current starts to increase rapidly: this region is called the breakdown.

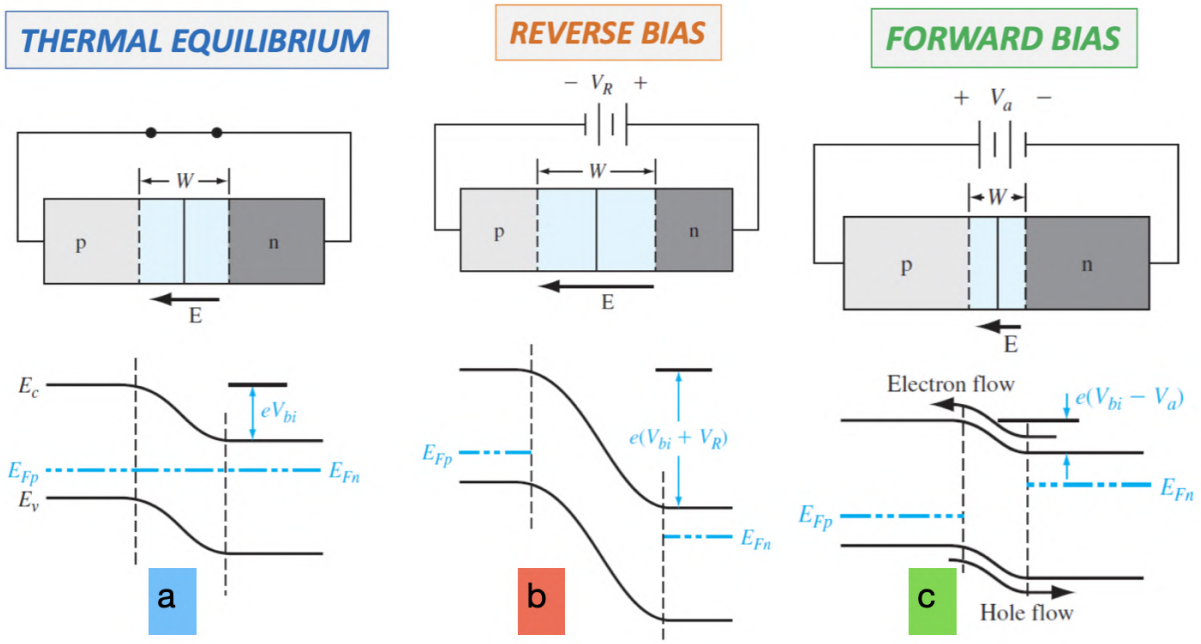

Figure 2.7: In the picture the pn junction is shown in case of no bias applied (a), in reverse bias (b) and in forward bias (c); it is important to note that the width of the depletion region and the height of the potential barrier changes based on the different configuration.

There are two mechanisms which give rise to the breakdown mechanism in a reversed-biased pn junction:

1. Zener breakdown occurs in highly doped pn junction throughout a tunneling effect: the conduction and the valence bands are sufficiently close that electrons can directly pass from the valence band in the p-side to the conduction band in the n-side.

2. Avalanche breakdown is due to electrons and holes that, moving in the depletion region, acquire enough energy from the electric field to create secondary electrons/holes pair by colliding with atomic electrons in the depletion region.

The ideal characteristic of a pn junction is given by (figure 2.8):

$$J = J_s(e^{\frac{eV_a}{kT}} - 1) \tag{2.1.11}$$

which accurately describes the voltage-current characteristic for the junction over a spectrum range of currents and voltages. It is valid for both positive and negative applied voltages V_a: when $V_a < 0$, for small values of the reverse bias, then the current

density is independent of the applied voltage; as the applied reverse voltage increases, on the other hand, the breakdown region described in 2.1.2 is approached. The saturation reverse current density J_s is defined by the equation 2.1.12:

$$J_s = \frac{eD_p p_{n0}}{L_p} + \frac{eD_n n_{p0}}{L_n} \tag{2.1.12}$$

where $L_{i,i=n,p}$ and D_i are respectively the diffusion length and coefficient and p_{n0} and n_{p0} are the initial hole/electrons concentrations in the n/p side.

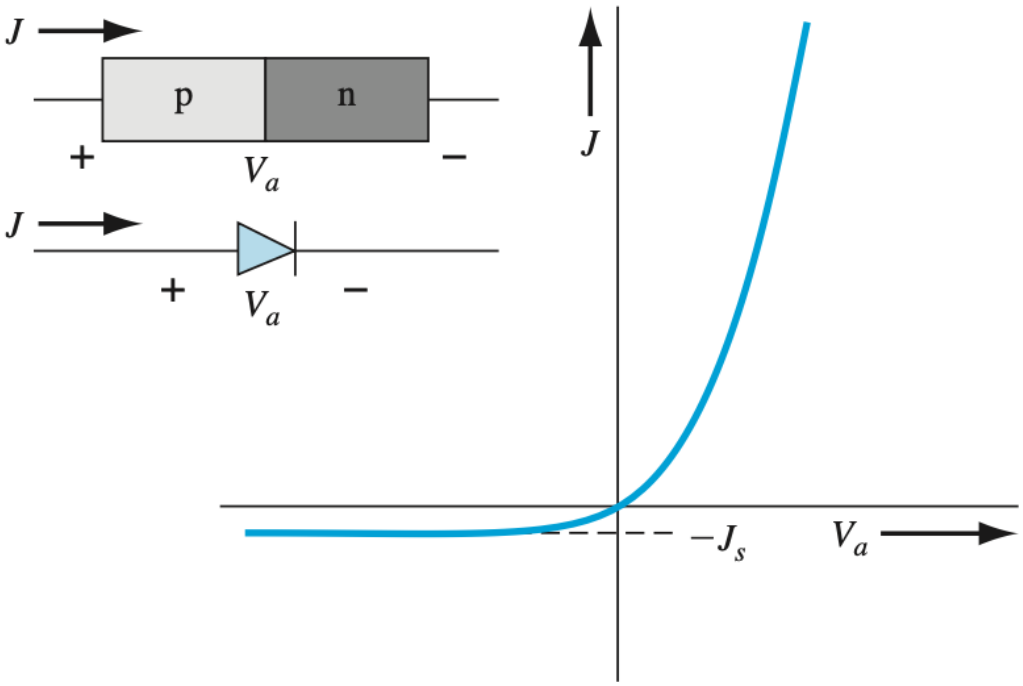

Figure 2.8: An ideal pn junction IV charateristic.

2.1.3 Semiconductor junction detectors

Semiconductor junction detectors are likened to solid ionization chambers that operate in reverse bias, measuring the small amount of charge created by a charged incident particle, which loses energy by ionization, or by a photon, which will be converted in turn to a charged particle. Since in normal junctions the depletion region is very small, "abrupt junction" with an asymmetric doping concentration, such as p^+n, is usually used; in this case the p part is highly doped and the depletion region extends almost entirely into the n region. The width W of the depletion region is expressed by equation 2.1.13, together with the inverse capacitance squared,which is a linear function of the reverse bias applied V_R.

$$W \approx \sqrt{\frac{2\epsilon_s(V_{bi} + V_R)}{eN_d}} \frac{1}{C^2} = \frac{2(V_{bi} + V_R)}{e\epsilon_s N_d} \tag{2.1.13}$$

where N_d is the donor concentration, C is the capacitance, ϵ_s is the medium dielectric constant. In figure 2.9 a plot of equation 2.1.13 is shown; it is possible to compute

the built-in potential looking at the point in the plot where $\frac{1}{C^2} = 0$. The slope of the curve is inversely proportional to the doping concentration of the low-doped region, which can be thus experimentally determined under the assumption of uniform doping in both the semiconductor region, the abrupt doping approximation and a planar junction.

When a photon beam crosses a material the initial intensity I_0 is attenuated according to the exponential law $I = I_0 e^{-\alpha x}$, where α is the absorption coefficient typical of the material and is the inverse of the mean free path λ, called absorption length. Silicon can absorb efficiently photons in a wide range of wavelengths (190-1100 nm) within a few tens of micrometers, making it well suited as a photodetector material. The photon is almost immediately absorbed (<10^{-2} μm) for very short λ, while it crosses the whole detector at very high λ (>10^2 μ m).

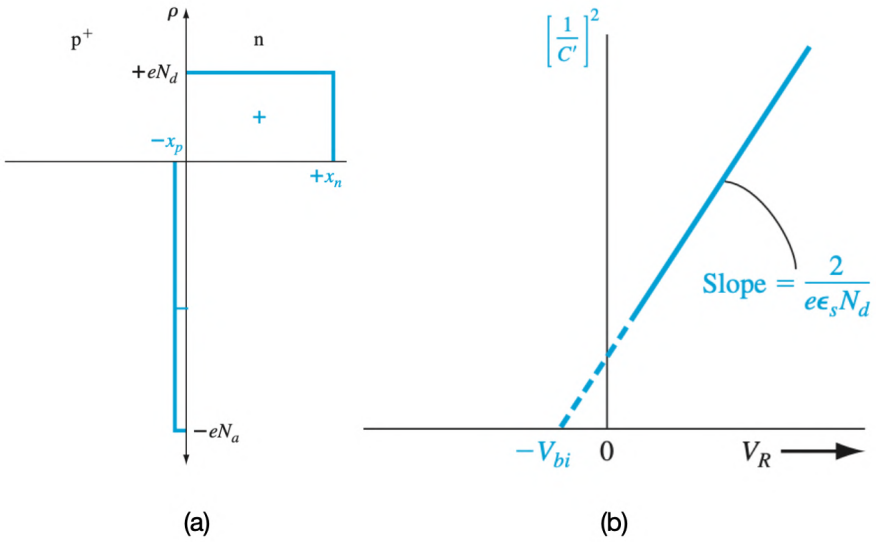

Figure 2.9: In the picture, the charge density is shown for electrons and holes (a); the inverse of the squared capacitance is also displayed (b).

2.1.3.1 The PIN photodiode

It is a special detector configuration in which an intrinsic semiconductor region is sandwiched between the p^+-side and the n^+-side; actually this region can also be slightly doped p (π region) or n (ν region). By doing so, the depletion region is largely enlarged, and the contact between the intrinsic, or quasi-intrinsic, region and the doped region becomes an ohmic contact; since the charge is almost zero, the electric field and thus the drift velocity are uniform in the depletion region. The advantages of using these photodiodes over photomultiplier tubes are compactness and price, greater insensitivity to magnetic fields, higher quantum efficiency, and lower applied voltage; however, because they lack intrinsic gain, they are insensitive under conditions of low light intensity, have a small sensitive area, poor time resolution, and the signal is small and must be amplified, introducing electronic noise.

2.1.3.2 Avalanche Photodiode (APD)

For electric field higher than the drift velocity saturation limit, the impact ionization starts to take place; photoproduced electrons and holes have sufficient energy to initiate secondary ionizations, producing an avalanche process very similar to the Towsend

avalanche in gases. The ability of electrons and gaps to start an avalanche is parameterized by the impact ionization coefficient $\alpha_{n,p}$ (cm$^{-}1$), which depends on the electric field through an empirical formula:

$$\alpha_{n,p} = \alpha_{n,p,\infty} e^{\frac{-\beta_{n,p}}{|E|}} \tag{2.1.14}$$

where $\alpha_{n,p,\infty}$ and $\beta_{n,p}$ are different constants for electrons and holes. The gain is defined as $G = e^{-\alpha d}$ where d is the thickness of the high electric-field region $(1 - 2\ \mu m)$ and for typical field value of $E = 3 \cdot 10^5\ V/cm$ the gain is $G \approx 50/300$ (linear region). With G>1, the APD photodetector can be sensitive to even a small number of photons: to achieve this, the PIN structure is enhanced with a gain layer. Figure 2.10 shows a p-gain layer added near the n+ layer, and the final structure from top to bottom is $n^+ - p - \pi - p^+$. As a result, the electric field is constant over the entire intrinsic region but grows sharply at the n+-p junction, where multiplication occurs. The APD produces an intrinsically amplified signal so the signal-to-noise ratio (SNR) is determined by the statistical fluctuations in avalanche formation. Clearly, this amplification affects also the thermal leakage current, resulting in what is called "excess noise." So in general, the SNR of the APD is no better than that of the PIN except at low light intensities, where the PIN signal must be amplified by the electronics, a source of noise. However, APDs also have disadvantages such as long dead times and low sensitivity to individual photons.

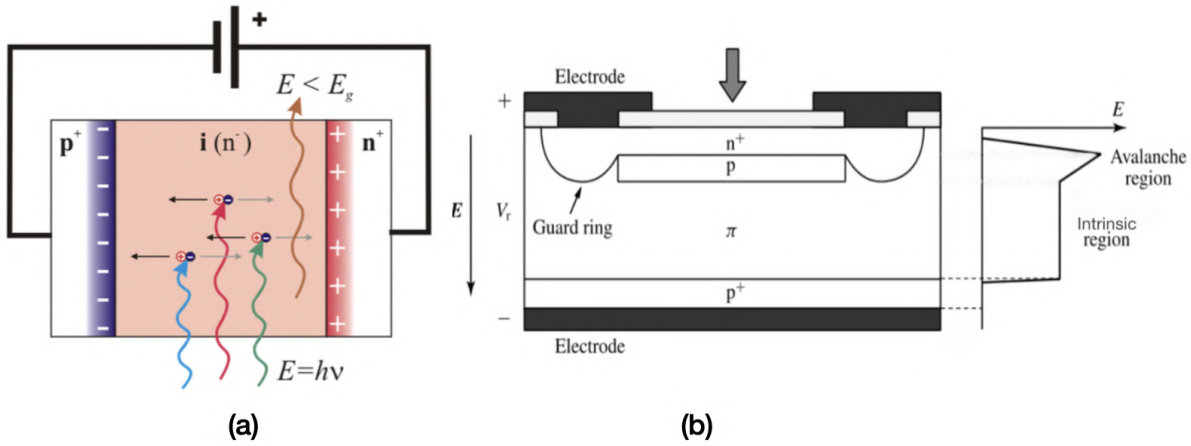

Figure 2.10: In the picture the panel 1 shows the typical structure of a PIN sensor, while panel 2 display the structure of an APD. The difference between the two is the presence of the gain layer in the latter.

2.1.3.3 G-APD or SPAD (Single Photon Avalanche Diode)

These devices operate in Geiger mode, where the reverse bias voltage is 10-20% greater than the breakdown value. In these conditions is possible to detect single photons. After the breakdown the avalanche is quenched by a passive resistor or an active transistor circuit, which, due to the high current value, produces a potential drop below the breakdown voltage. Advantages of using SPADs include a large output signal (large gain), high sensitivity to low light intensities, even to single photons, excellent temporal resolution, and greater insensitivity to magnetic fields than APDs.

A more precise description of these photosensors, which are the component unit of Silicon Photomultipliers, is as follows: there are three regions of cell operation (figure 2.11), depending on the voltage applied:

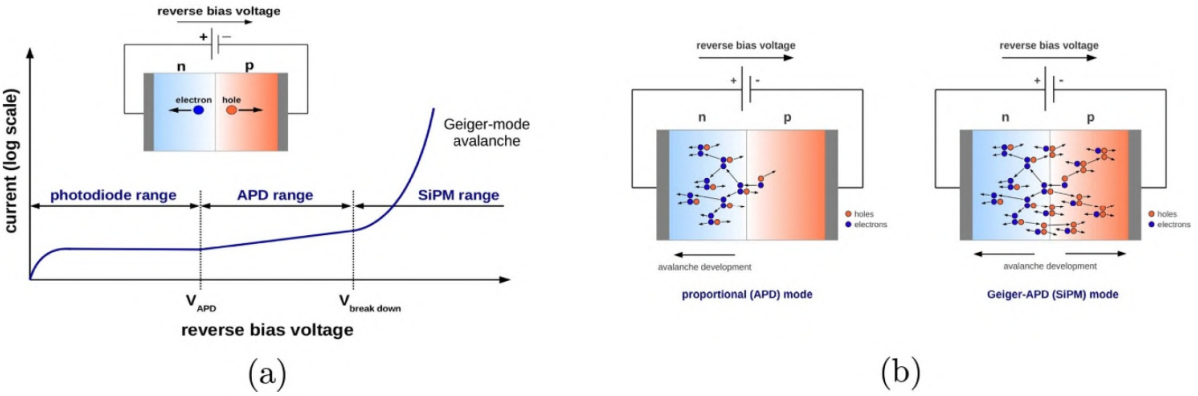

Figure 2.11: In the picture the three different region of working for a SiPM are shown (a); the difference between APD region and Geiger mode is shown in the panel (b): in the latter even holes partecipate to the avalanche, while in the former secondary ionization affect only electrons [38].

1. when V_{bias} is low no multiplication takes place and each photon can create only one electron/hole pair, which are separated by the presence of the electric field;

2. however, as V_{bias} increases, the electric field also increases and the electron has enough energy to create secondary ionization, which give rise to an avalanche. In this case the sensor works in the APD region where only electrons participate in the avalanche: the current is proportional to the number of incident photons and the avalanche flows in only one direction. The avalanche is self-quenching, so in this regime no external circuit is needed;

3. if the voltage exceeds the breakdown voltage, the pits also participate in the avalanche. The electric field of the order of $10^{-5}\ Vcm^{-1}$ is such that a charge carrier (both electrons and holes) triggers a self-sustained avalanche, so that the current grows very rapidly. An external quenching circuit is needed to damp the avalanche, bringing the voltage below the breakdown value, and for the sensor to be sensitive to photons again, the original bias must be restored.

2.1.4 Silicon PhotoMultiplier (SiPM)

The last configuration, where both electrons and holes participate to the avalanche, is the case of the SiPM: it is an array of SPADs with order of 10^3 pixels in a total area of some mm^2; they operate in Geiger mode with a gain up to 10^6. Each SPADs, or pixel gives a binary response, depending if it was hit or not (and so depending also on their detection efficiency), making SiPM single photon detector[39] [40]. The structure of SiPM is reported in figure 2.12, where 3 pixels are visible, each composed by (from the bottom): the p^+ substrate, the lightly doped π region, where the most part of photon conversion takes place, and the junction, made by a p^+ gain layer and a n^{++} layer. Each pixel has its own quenching resistor. Typical thickness are $0.1 - 1.5\ \mu m$ for the n^{++} layer and $1 - 3\ \mu m$ for the p^+ gain layer and few μms for the intrinsic π region.

2.1.4.1 Breakdown voltage and multiplication gain

The peculiarity of these silicon sensors lies in their ability to work beyond the breakdown voltage, where the current exhibits divergent behaviour. Here the multiplication

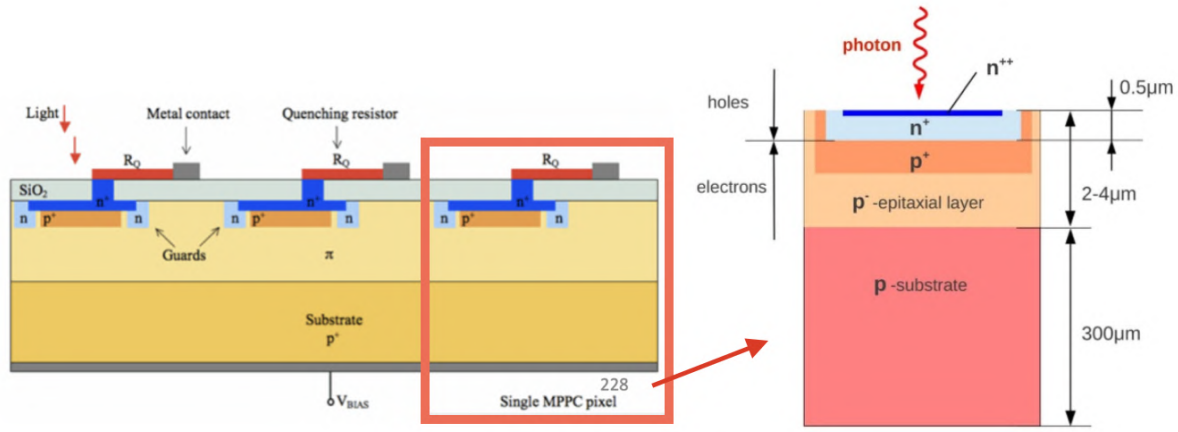

Figure 2.12: In the picture the SiPM typical structure is reported, together with a zoom on the structure of a single SPAD.

factor M, defined as the number of secondary charge carriers produced by each primary carrier, diverges. The advantage of working in this regime lies not only in the high gain but also in an almost gain-independent noise factor. The condition for an avalanche to be created is that sufficient positive and negative charge carriers are created by ionization: if α_n and α_p are the ionization rates for electrons and gaps and W is the width of the depletion region, the mathematical condition for entering such a multiplication regime [41] is as follows:

$$\int_0^W \alpha_n e^{-\int_0^x (\alpha_n - \alpha_p) dx'} dx = 1 \tag{2.1.15}$$

From general studies on the breakdown conditions the following conclusions can be given:

1. V_{BD} increases with W, the thickness of the depletion region;
2. increasing W, V_{BD} becomes more dependent on temperature;
3. in the depletion region, the reproducibility of V_BD is higher.

As a consequences, working with thick depletion region is not convenient in terms of breakdown uniformity and temperature stability, while is more advantageous using thin depletion region sensitive from blue to UV light. Moreover, in SPADs with integrated quenching resistors the gain is generally well defined and it is given by:

$$G = V_{OV} \cdot \frac{(C_q + C_d)}{q} \tag{2.1.16}$$

It is typically of the order of 10^5 to 10^7 and gives to SiPM excellent single photon counting capabilities.

2.1.4.2 Electrical equivalent circuit of the SPAD

The connection (figure 2.13) is modelled as a parallel of the internal resistance of the diode space-charge region $R_d \approx 1\ k\Omega$ and the inner depletion region capacitance, $C_d \approx 0.1\ pF$, which is in turn the sum of the SPAD area capacitance and other perimeter or parasitic capacitances. An integrated quenching circuit is added, consisting in a

quenching resistor $R_q \approx 10^2\ k\Omega$ and a parasitic capacitance C_q: the latter is responsible for a fast signal extraction, which is very beneficial for timing applications. When an avalanche is triggered, the circuit is closed, and the capacitor C_d starts to be discharged, provoking an exponential voltage drop at the internal node between C_q and C_d, initially at the bias voltage. When the circuit is close, even the capacitance C_q is charging via R_d so that the discharge time constant is $\tau_r = R_d(C_q + C_d) \approx 100\ ps$, neglecting the influence of R_q, usually highly resistive; this provide the signal rise time and it is usually fast. the maximum voltage drop is obtained at the breakdown voltage V_{BD}, while typical bias applied are typically $\approx 30 - 70$ V. The discharged of C_d and the recharge of C_q is stopped when the current I_d through R_d reaches the threshold value below which the formation of a self-sustaining avalanche is suppressed. This current value I_d is a little bit higher than the minimum asymptotic value [42] reported in equation 2.1.17:

$$I_d f = V_o v/(R_q + R_d) \approx V_o v/R_q \tag{2.1.17}$$

Once the avalanche is quenched, the recovery time of the charge is given by $\tau_{recharge} = R_q \cdot (C_q + C_d)$ .The latter constitues the SPAD recovery time usually of the order of some ns. The avalanche is quenched near the asymptotic value, so the total charge that has to be provided from the outside is $V_{ov} \cdot (C_q + C_d)$, where the overvoltage is defined in equation 2.1.18

$$V_{ov} = V_{BIAS} - V_{BD} \tag{2.1.18}$$

and represents the the SPAD gain multiplied by the electron charge. The output of SiPM is the sum of the single pixels outputs, which are joined together via the quenching resistor to a single output node; the output signal is, in the end, proportional to the number of activated cells.

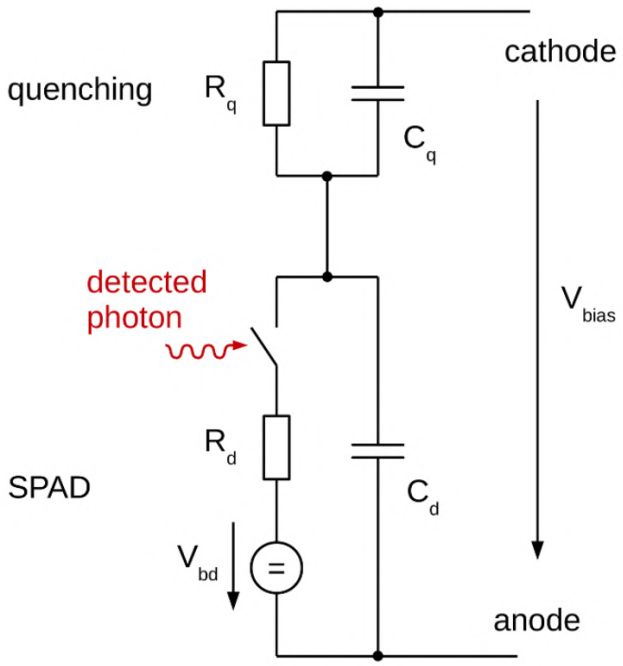

Figure 2.13: In the picture the typical circuit of a SPAD is shown [38].

2.1.4.3 SiPM saturation and non-linearity

To be more precise, only under low light intensity conditions each sensor pixel can be assumed hit by a single photon; this condition is called linearity and the total number of activated cells is proportional to the number of incident photons. However, as the amount of incident light increases, the SiPM enters the saturation region where each pixel can be hit by more than one photon. The general equations for the number of triggered SPADs [43] is function of the number of photons N_{photon} and of the total number of SPADs in the SiPM (N_{tot}) under the assumption of uniform illumination:

$$N_{fired\ cells} = N_{tot}(1 - e^{\frac{-N_{photon} \cdot PDE \cdot ENF}{N_{tot}}}) \tag{2.1.19}$$

where the Photon Detection Efficiency (PDE) and the Excess Noise Factory (ENF) are explained in the following. In case of large signals, a limited number of SPADs causes saturation, but in the last year much smaller SPAD size are available (down to 10 μm) improving the linear range.

2.1.4.4 Photon Detection Efficiency

An important figure of merit of SiPMs is Photon Detection Efficiency (PDE): it quantifies the ability of a single-photon detector to detect photons. PDE is defined as the ratio between the number of detected photons and the number of incoming ones and its expression is given by equation 2.1.20.

$$PDE = Q_E \cdot P_G \cdot F_A \tag{2.1.20}$$

where we define the quantum efficiency Q_E (which typically assumes values between 70 and 80%) as the number of electron-hole pairs created by an incident photon, the fill factor F_A (20-80%) as the fraction of sensitive area over the total entrance-window area of the sensor; the Geiger probability P_G (90%), which is the breakdown probability. Q_E depends on the wavelength λ and for the detection in the UV range it is optimized by using special protecting coating. For what concerns the fill factor, the inactive area is created in order to separate SPADs electrically and optically from each other, and it is usually lower for smaller cells size; however, in modern small size pixels it has improved by using transparent metal film quenching resistors (MFQR) versus the more standard option of a non transparent Polysilicon quenching resistor. Finally, P_g is a function of the overvoltage and the the wavelength of the incoming photons. Electrons have higher ionization rate respect to holes, and they are easier to be collected when generated by an incoming photons. Typical values for the PDE are between 40-60% but it depends on the wavelength: a red photon, with $\lambda \approx 700\ nm$ has an absorption depth of some μm so it is absorbed in the intrinsic region, while a blue photon ($\lambda \approx 450\ nm$) penetrates only $\approx 0.5\ \mu m$ so it is absorbed near the junction.

2.1.4.5 Excess Noise Factor

Despite a small sensitive area, the advantages of using these sensors are several: high gain that allows them to be single-photon sensitive, high PDE, excellent temporal resolution (definitely below 100 ps), low applied voltages, great insensitivity to magnetic fields, compactness, low price. However, they are susceptible to several sources of noise such as:

1. **dark current (DC)** due to thermal e-h pair generation in the active volume; the DC rate depends on temperature (it it doubles every 10°C [38]), on active area and on overvoltage;

2. **optical cross talk between pixels:** during the avalanche, charge carriers are accelerated in the high electric field region and emit photons in the near infrared. These photons induce fake signals in the neighbouring cells;

3. **afterpulsing:** if impurities are present in the silicon, charge carriers could be trapped and after a time delay, they are released and are free to start an avalanche, inducing a signal, called afterpulses, in some pixel. If the time delay is short, as few ns, the pixel is not already fully re-charged and the impact of afterpulses is negligible; however, for time delay of $\approx 10^2$ ns it produces fake signals, therefore the silicon must be as pure as possible;

4. **temperature dependence of the breakdown voltage:** V_{BD} increases linearly with the temperature, changing the overvoltage value, which affects many of the SiPM performances. For large temperature variations it is necessary to apply a compensation, as an automatic system that changes the bias applied in response to the changing temperature.

The fluctuations on the number of primary triggered SPADs for incoming photons (called photoelectrons, N_{phe}) for an ideal photodetector are given by $\sqrt{N_{phe}}$. However, considering some non-ideality factors as the inter SPAD cross-talk and the integrated afterplusing which increase the signal, one would find a value for N_{phe} greater than the real one and this is often referred as the excess charge factor $ECF = \frac{\langle Q \rangle}{\langle Q_N \rangle}$ where $\langle Q \rangle$ is the average total charge measured and $\langle Q_n \rangle$ is the average charge of the primary photoelelectrons. This excess of charge appears as an artificial gain which is also called excess noise factor [44]:

$$ENF = \frac{(\sigma_Q / \langle Q \rangle)^2}{(\sigma_{Q_N} / \langle Q_N \rangle)^2} \tag{2.1.21}$$

where σ_Q is the standard deviations of the measured spectrum. It is important to note that afterpulsing and cross-talk depend on the strength of the electric field, and thus the ENF increases with overvoltage; however, new studies on isolation of individual SPADs to reduce cross-talk have shown that it is possible to have an ENF close to unity even with an overvoltage of 5 V.

2.1.4.6 Single Photon Time resolution

The SPTR has several contributions, as reported in equation 2.1.22

$$\sigma^2_{SPTR} = \sigma^2_{electronic\,noise} + \sigma^2_{TDC} + \sigma^2_{current} + \sigma^2_{TS} \tag{2.1.22}$$

where

$$\sigma_{TDC} = \frac{TDC_{bin}}{\sqrt{12}}$$

is the term related to the analog-to-digital conversion, $sigma_{current}$ is related to the Landau fluctuations of the deposited charge and $sigma_{TS}$ is the time slewing term, due to the fact that the signal overcome the threshold at a time which depends on its amplitude. It is possible to refer to the latter two terms as intrinsic time resolution.

The part of the single photon time resolution SPTR only caused by the electronic readout [45] is

$$\sigma_{electronic\ noise} = \frac{\sigma_{\nu_{noise}}}{dV/dt_{threshold}} \tag{2.1.23}$$

where $\sigma_{\nu_{noise}}$ is the standard deviations of the electronic noise floor and $d\nu/dt_{threshold}$ is the the slew rate of the signal at a given threshold. $\sigma_{electronic\ noise}$ is one of the few parameter which can still be widely improved, since front-end readout, bandwidth and electronics noise play a key role in reaching the intrinsic SPTR limits imposed by the SiPM itself. It can be shown that with a low noise amplifier, a signal with a faster rise time (larger bandwidth) lead to better timing response. Recently, some improvements have been achieved using high-frequency electronics, although despite the optimized electronics the intrinsic SPTR of the SiPM at FWHM appears to be 70 ps, having already subtracted the contribution of electrical noise calculated as in 2.1.23. In addition, the way the SPADs are constructed and linked together greatly impacts this parameter, making it difficult both to make an exact estimate and to design some focused improvement.

2.1.5 SiPMs in HEP

The first large experiment using one of the first fully commercial SiPMs from Hamamatsu was the neutrino detector T2K ($1.3x1.3\ mm^2$, $50\ \mu m$ pitch). At the LHC the first experiment using them was CMS, where they replaced the Hybrid Photo Diodes in the Hadronic Calorimeter HCal. The initial decision to use Hybrid Photon Detectors HPD [2] was forced by the need for magnetic field tolerance, but the implementation of more than 18,000 large-area SiPMs improved the signal-to-noise ratio and stability. In order to satisfy the large linear range needed in the HCal, CMS collaborated with several companies to develop $15\ \mu m$ pitch sensors with more than 4000 SPADs per mm^2. In general, the major complications of working at late energy are the highly radioactive environment and the dependence of sensor gain and PDE on temperature, which causes a shift in the breakdown voltage. Radiation damage creates an increase in leakage current due to defect formation in silicon, increasing the DCR and consequently the ENC as follows [46]:

$$DCR = \frac{I_d}{Gq} \tag{2.1.24}$$

$$ENC = \sqrt{DCR \cdot T_I} \tag{2.1.25}$$

where I_d is the SiPM current, G is the gain at a given overvoltage, q the elementary charged and T_I the integration time. To give some number, the expected dark count rate of most SiPMs was below 100 kHz mm^2 but with radiation it increases quickly to 1 MHz mm^2 for every 10^9 neutrons/cm^{-2} and an overvoltage of 3 V [38].

The radiation damage induced by high DCR is a delicate issue especially for timing; the time resolution of a detector has many contributions and can be parametrized as:

$$\sigma_t = \sigma_t^{clock} \oplus \sigma_t^{dig} \oplus \sigma_t^{ele} \oplus \sigma_t^{phot} \oplus \sigma_t^{DCR} \tag{2.1.26}$$

with σ_t^{clock} the clock distribution jitter, σ_t^{dig} the digitization induced jitter, σ_t^{ele} the electronic contribution, σ_t^{phot} photostatistic contribution of the scintillation emission and σ_t^{DCR} the dark count rate induced noise equivalent timming jitter. The temporal performance of

[2] They are PMT with a photosensitive cathode and an array of APD made of cells

these sensors is driven by the photo-statistics terms (PDE and SPTR) and the DCR-related noise term, particularly at high values. The photo-statistics term at zero DCR is related to fluctuations in photon arrival times at the sensor and is equal to $\sigma_t^{phot} = \frac{1}{\sqrt{N_{phe}}}$ where N_{phe} is the number of photoelectrons. The contribution of the dark current rate is expressed by the equation:

$$\sigma_t^{DCR} \propto \frac{\sqrt{DCR}}{N_{phe}} \tag{2.1.27}$$

It can be seen that the time resolution is affected by the DCR as much as the electronic noise and the $\sqrt{DCR}$ is the noise amplitude; increasing the signal to noise ratio, or equivalently the detected light intensity, the time resolution can be further improved.

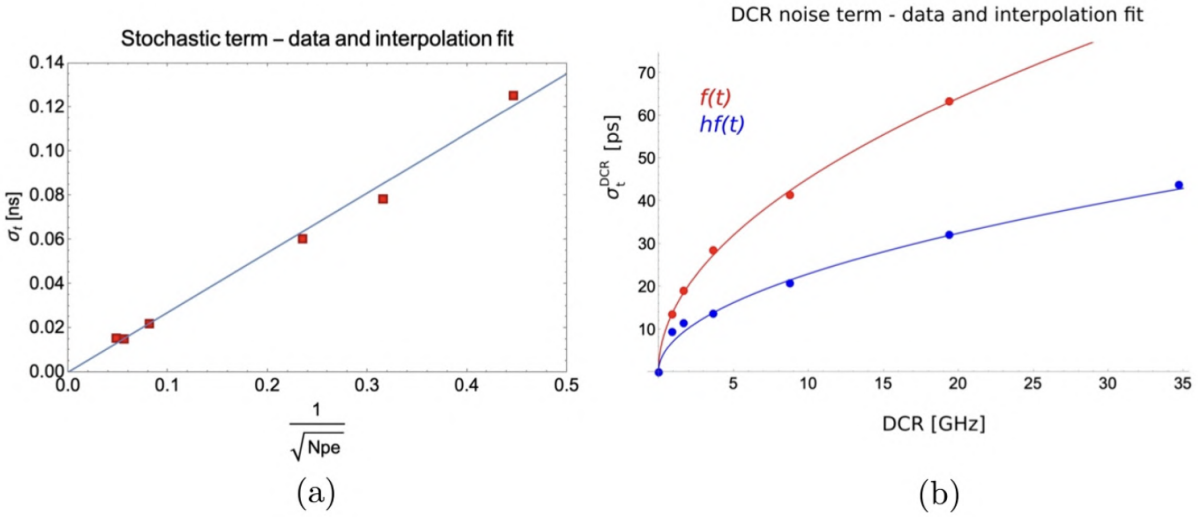

Figure 2.14: Time resolution of the SiPM for different signal amplitude in case of DCR=0 is shown (a); in (b) additional time jitter due to DCR up to 35 GHz is shown: it is measured by randomly injecting light on the sensor for a signal of 390 photoelelctrons [38].

The time resolution dependence on DCR and N_{phe} is shown in figure 2.14, where a LED with pulse time spread of 350 ps is used: the DCR noise term will be the dominant factor in the resolutions due to large radiation fluency. In the figure 2.14 (b), on the other hand, shows the comparison between a constant fractional algorithm (called Constant Fraction Discrimination method, CFD) and a simple leading edge approach (fixed threshold method), respectively $hf(t)$ and $f(t)$ in figure. The former consists in evaluating the time resolution when the signal overcome a certain percentage in amplitude, and not a fixed threshold as in the latter; however, the former seems to provide benefits over the latter in high radiation environments. To obtain $hf(t)$, the signal $f(t)$ is processed so that the waveform is inverted and delayed and then summed with the original pulse resulting in $hf(t) = f(t) - f(t + dt)$: doing so results in a baseline that has smaller oscillations due to DCR.

2.1.5.1 NUV-HD SiPM Technology

Near Ultra Violet High Density (NUV-HD) SiPM technology [48] was introduced in 2016 with the aim of providing better electrical insulation: the cells are separated by deep trenches filled with silicon dioxide. Due to the different refractive index of silicon, this implies also an optical isolation. The typical structure of a NUV-HD SiPM is reported in figure 2.15.

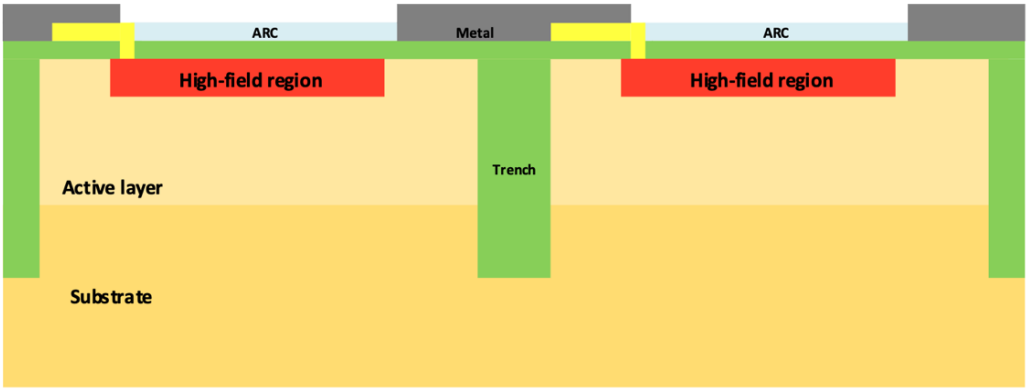

Figure 2.15: In the picture typical structure of a NUV-HD SiPM [47]; trenches, in green, are present to isolate optically and electrically the sensor.

The active area is defined by a high-energy ion implantation, called a deep implant or DI, which grows the electric field between the surface to achieve the multiplication conditions. The space between DI and silicon is called virtual guard ring (VGR) and prevents from premature breakdown: here the cell is not sensitive to light. The distance between DI and trenches, together with the trench width are critical dimensions (CDs) and are minimized to increase the Fill Factor $FF = \frac{ActiveArea}{CellArea}$, where the active area is approximately the DI area, since the dead border are smaller than $2\ \mu m$. In figure 2.16a the fill factor is reported as a function of the cell pitch [49], where the recent NUV-HD technology is compared to the older one without trenches.

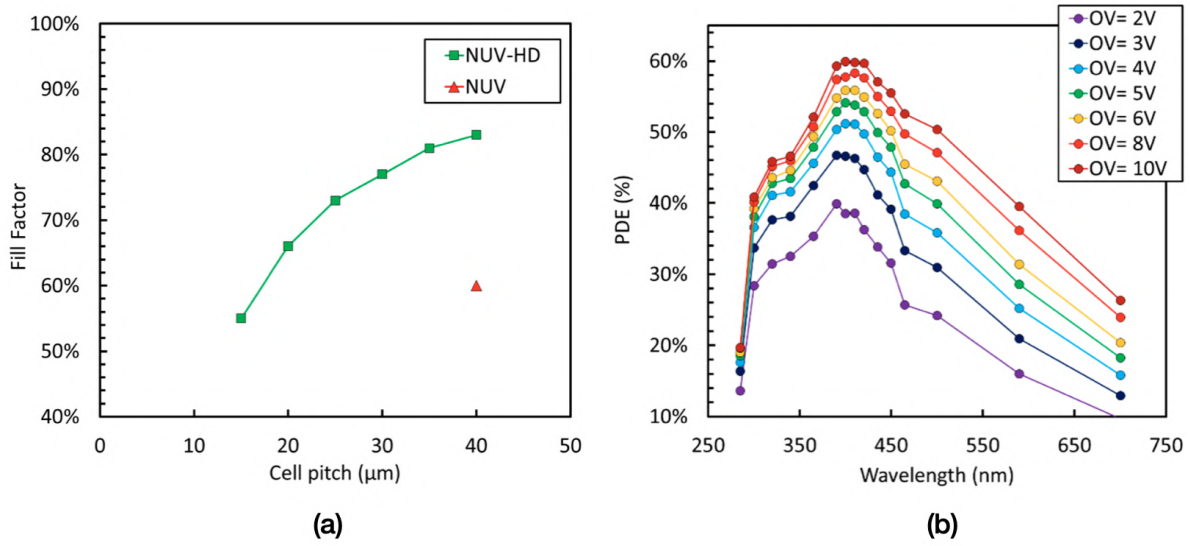

Figure 2.16: The figure shows the Fill Factor as a function of the cell pitch (a), with an evident benefit from the new technology (green line); the PDE as a function of the wavelength is shown (b): the peak is about 60% at 420 nm [47].

An improvement is visible in the former case over the latter, partly because the old technology had larger dead edges; we see that all cells built with the same technology lie on the same line, from the fit of which we derive the critical dimensions. Moreover, PDE measured at 410 nm (figure 2.16)b shows a peak of 60% at 410 nm [50]-[51]; the sensor was covered with protective silicon resin, transparent down to 300 nm. The

important thing is that this curve corresponds to the peak emission of LSO/LYSO crystals ($\approx 410\ nm$) offering a technology with advanced temporal performance particularly for TOF-PET application [52]: the coincident resolving time CRT corresponding is less than 100 ps FWHM. In addition to this, the PDE is close to 50% even at 300 nm, making this technology also suitable for Cherenkov light dejection.

2.1.5.2 NUV-HD-MT SiPM

Standard NUV-HD technology [48] features silicon dioxide SiO_2-filled trenches to optically and electrically isolate the SPAD, although this also has a benefit in reducing Cross Talk (CT).

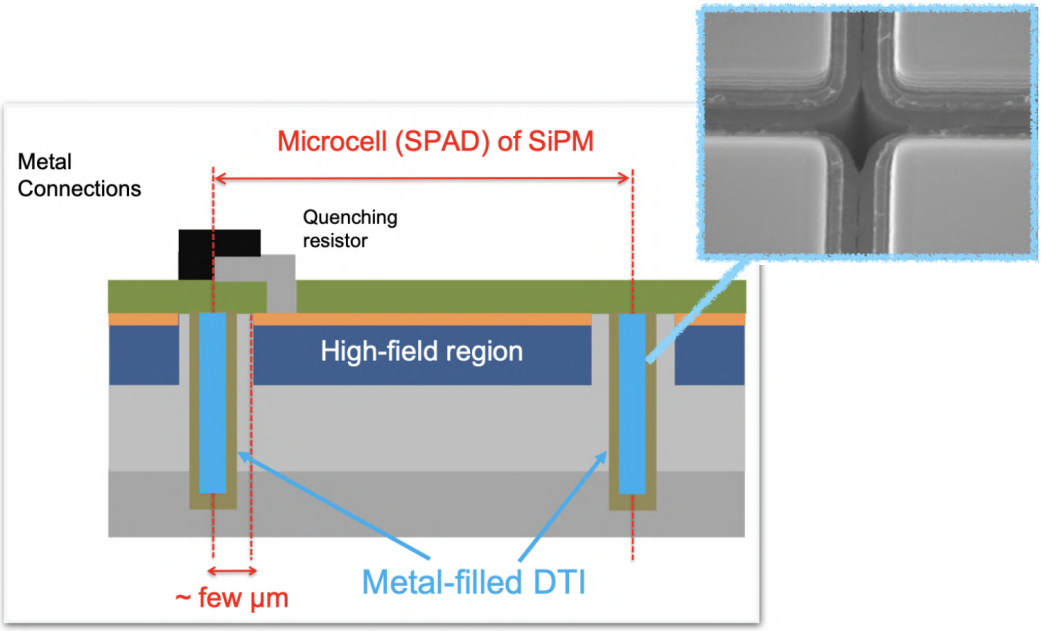

Figure 2.17: The typical structure of a SiPM with metal trench is shown in the figure; the zoom shows the typical structure between two SPADs.

In fact, although silicon dioxide is transparent to CT photons, nevertheless the reflections introduced in the oxide layer result in an effective reduction in the level of Cross Talk. The introduction of metal trenches (figure 2.17) could further improve the sensor noise levels; the reduction of the optimal Cross Talk probability allows the maximum voltage applicable to the sensor to be increased (see figure B.1 in appendix B.1).

The ability to apply higher voltages compensates for the slight decrease in active area that results from the introduction of trenches. Although the peak of the Photon Detection Efficiency (PDE) is between 390 and 420 nm, the PDE in the red range also reaches saturation due to the large applicable overbias that maximizes the multiplication of holes in the avalanche (figure 2.18 in appendix B.1). Increasing the applicable bias also allows for larger gains and lower values of Single Photon Time Resolution (SPTR).

2.1.5.3 Charged particles detection

When a charged particle crosses the SiPM, an excess in measured cross-talk is observed with respect to standard CT-DC, the intrinsic cross-talk measured on Dark

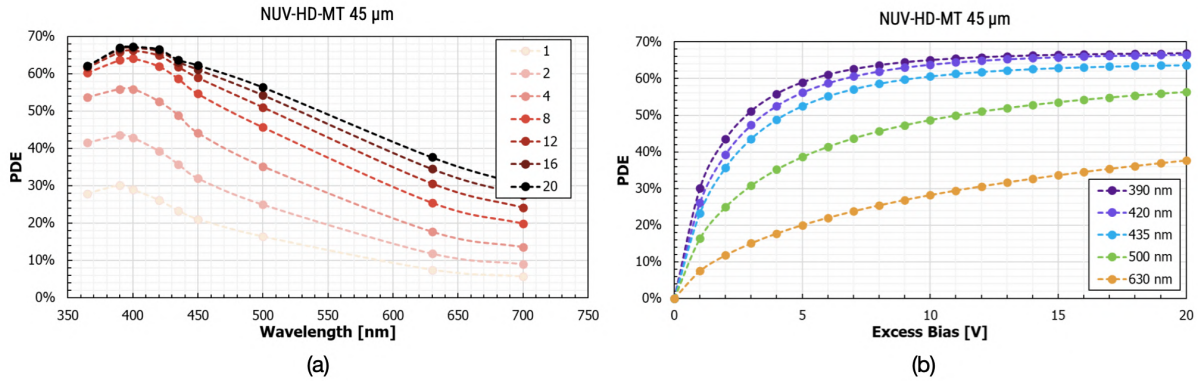

Figure 2.18: Photon Detection Efficiency as a function of wavelength and applied voltage is shown in the figure.

Count events. If this phenomenon were due to Cherenkov radiation emitted when the particle passes through the resin layer (placed above the sensor for its mechanical protection) , it should be more pronounced when the particle approaches the sensor from the front (i.e. the photosenstivie side), and be suppressed when the particle arrives from behind. This is no longer true if the excess is attributed to phenomena occurring in the bulk of the sensor, which have no dependence on the direction of the incident particle.

In figure 2.19 are reported the measurement of F_n, defined in equation 2.1.28, for different voltages and different sensors:

$$F_n = \frac{events\ with\ n\ SPADs\ fired}{events\ with\ n \geq 1\ SPADs\ fired} \tag{2.1.28}$$

From the results [53], it does not appear that the effect is related to phenomenon in the bulk; in fact, for sensors without resin (WR in the plot B.2), there is no dependence on the direction of the incident particle. In contrast, in the presence of the resin layer, a multi-SPADs signal is present when the particle enters the sensor from the front, with most events activating more than 4 SPADs, whereas if the particle arrives from behind the distribution of F_n is shifted to higher values of n. This could indicate reflection on the resin layer when the particle enters the sensor on the back. In any case, this effect seems correlated to the emission of Cherenkov light when a charged particle crosses the resin, and since the Cherenkov cone has a radius of the order of 0.5-1 mm the sensor is able to detect also light from a particle passing passing not necessarily directly on the sipm, but in the nearby resin.

2.1.5.4 Time Resolution

In figure 2.20 time resolution improves as the number of hit SPADS increases, showing a trend compatible to a $\frac{1}{\sqrt{N_{SPAD}}}$ scaling [54]. Time resolution lower than 20 ps are obtained if N_{SPAD}>6 for sensors with the resin protection layer, and the number of events involving a small number of SPADs is low. The application of such sensors in detecting charged particle results in a huge noise rejection respect to the standard photons detection; keeping a threshold above 3 SPADs shows an efficiency higher than 99% getting rid of those noise event coming from DCR and CT. On the contrary, for the sensor without resin coverage WR, the time resolution at 2 or 3 SPADs is strongly deteriorated by DCR and CT.

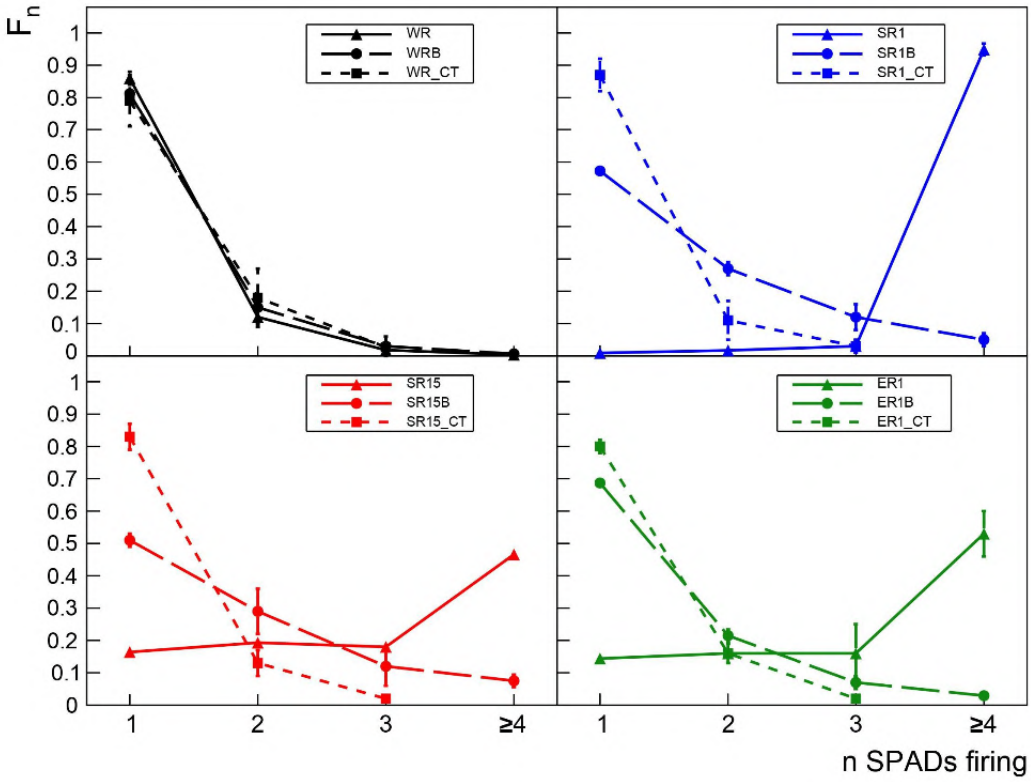

Figure 2.19: In the picture F_n is plotted as a function of the number of fired SPADs; the distribution indicates presence of multiple-SPADs event for sensors with the protection layer, which also have a dependence on the particle direction. The same behaviour is not observed in WR sensors, suggesting the presence of Cherenkov light [53].

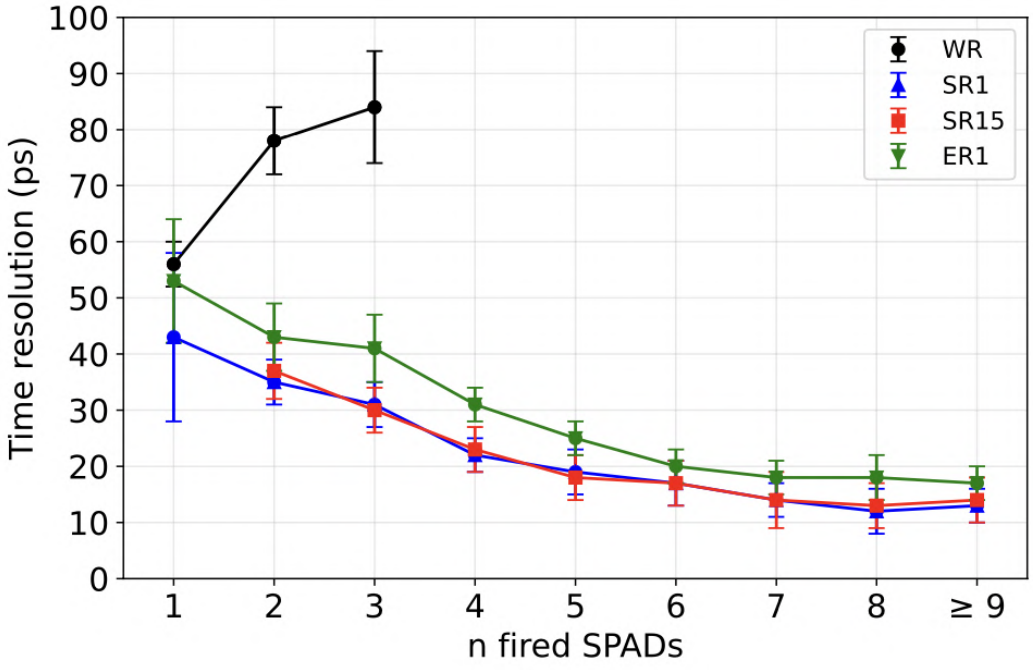

Figure 2.20: The time resolution as a function of the number of SPADs fired is shown [54].

Chapter 3

SIPM measurements

The following section concerns the characterization of some prototypes of Silicon PhotoMultipliers (SiPMs) produced by the Bruno Kessler Foundation (FBK); in particular, sensors belonging to two different technologies, the standard NUV-HD SiPMs and the NUV-HD-MT SiPMs, were studied. The analysis is structured as follows: the preliminary phase includes evaluation of the Dark Count Rate (DCR) for all sensors, both those irradiated with a charged particle beam and those not, and measurements of current and capacitance as voltage changes (IV and CV curves); also in this case, a comparison between irradiated and non-irradiated sensors is presented. The second step involves the timing characterization of the sensors when hit by photons emitted from a laser source: samples with different thickness of the protection layer, placed above the SiPM itself, were chosen for this measurement for comparison. Finally, the timing resolution is also evaluated by means of a charged particle beam.

Sensor type	*Sensor name*	*Resin*	*FF*	*Cell pitch (μm)*	*Area (mm^2)*
NUV-HD	SR1A	Silicon 1 mm	82.8%	40	9
	SR15B SR15D	Silicon 1.5 mm			
	E1C E1A	Epoxy 1 mm			
	WR-L WR-E	No resin			
	SR3G SR3F	Silicon 3 mm			
NUV-HD-MT	A1, B1 C1, D1	Silicon 1 mm	81.1%	40	9
	A15,B15 C15,D15	Silicon 1.5 mm			
	WR-55 WR-63 WR.64	No resin			

Table 3.1: Summary of the features of the sensors analyzed.

The characteristics of the sensors analysed are shown in table 3.1; NUV-HD-MT sensors are shown in figure 3.1 (a) and standard technology sensors in figure 3.1 (b).

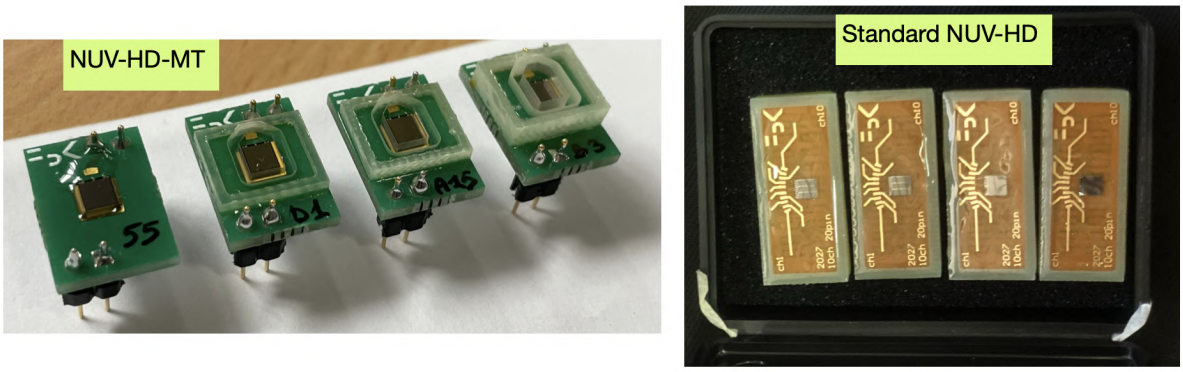

(a) (b)

Figure 3.1: Picture of the analyzed samples both of NUV-HD-MT technology (a) and of standard NUV-HD (b)

3.1 Preliminary measurements

3.1.1 Dark Count Rate

The dark count, as described in 2.1.4.5, is the presence of signal in a completely dark condition and it is evaluated by acquiring with the oscilloscope the sensor signal when it is isolated from any photon source. The rate of the signal is then analyzed by counting how many times it exceeds the value attributed to a SPAD hit. This threshold value depends on the technology under study and may be assumed with reference to one SiPM: typical values are of the order of few tens of mV at 2 V of overvoltage OV, which is defined according to equation 2.1.18. However, the amplitude associated to one SPAD may vary from sensor to sensor even within the same technology so the threshold chosen to compute the DCR is chosen according to experimental observation.

Figure 3.2 shows the typical signal of an irradiated sensor (a) and that of a non-irradiated sensor (b); the increase in DCR is evident, as one goes from a frequency at 3 OV less than 1 MHz/mm^2 to one higher than 10 MHz/mm^2 after an irradiation of at least 10^9 $1MeV$ n_{eq}/cm^2.

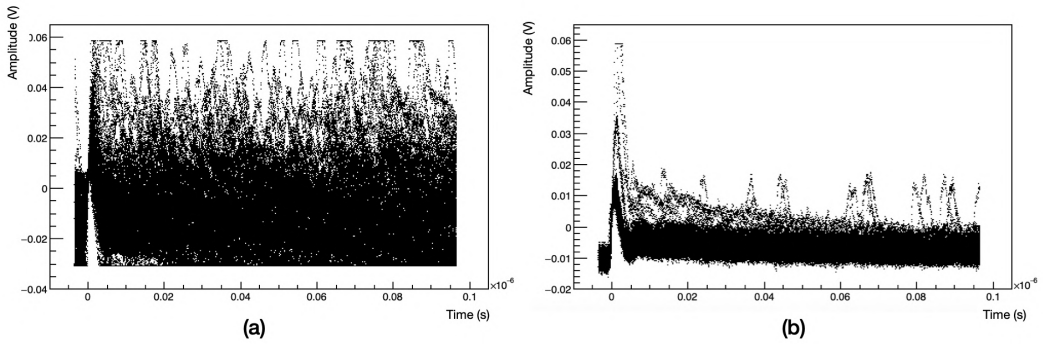

Figure 3.2: A comparison of the dark count rate for an irradiated sensor (a) and a new one (b) for two NUV-HD sensors with 1.5 mm resin is shown in the figure.

Figure 3.3 shows a typical signal of a NUV-HD-MT SiPM, irradiated (a) and not-irradiated (b); at 3 OV the new sensor has a higher DCR respect to standard NUV-HD sensors but still very low, of the order of $1MHz/mm^2$. The irradiated sensor, on the

other hand, has a frequency slightly lower than 10MHz/mm^2, but the difference is not significative compared to standard technology; in this case, the threshold corresponding to a SPAD at 3 OV has been set at 75 mV because these sensors have greater amplitudes than the previous ones.

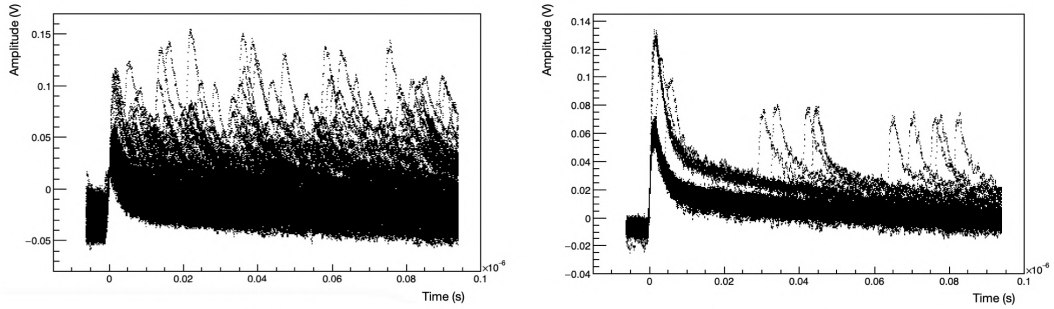

Figure 3.3: A comparison of the dark count rate for an irradiated sensor (a) and a new one (b) for two NUV-HD-MT sensors with 1 mm resin is shown in the figure.

Figure 3.4 shows offline scans of the DCR, which consists in varying the threshold for the evaluation of the dark count events; the trend is as expected, i.e. a very high frequency at low thresholds where electronic noise predominates, and then lowering to zero as the threshold amplitude increases.

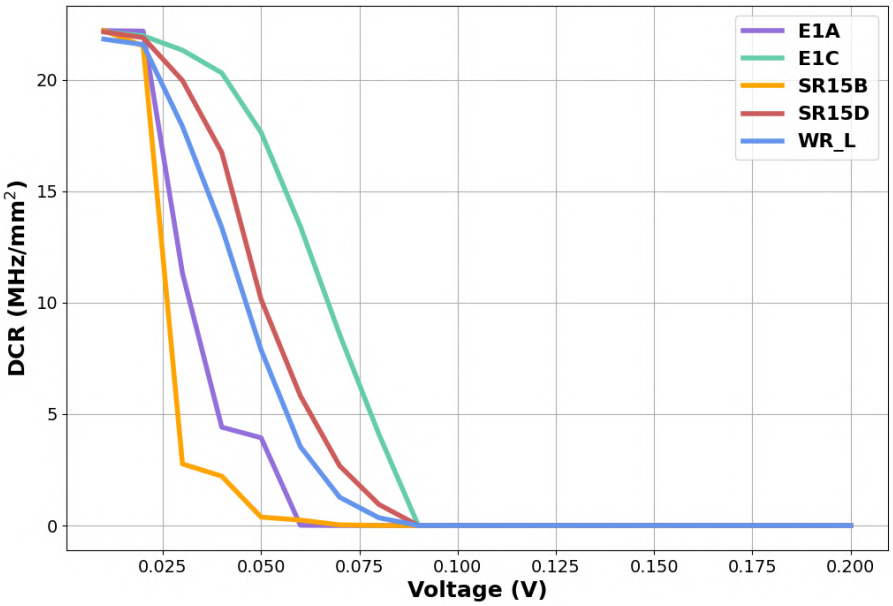

Figure 3.4: Figure shows the frequency of DCR as the threshold changes in amplitude for sensors with different coverage, both irradiated and not.

A comparison of sensors with different protection layer (or without it) can be seen in figure 3.4 for both irradiated and non-irradiated sensors for both of the NUV-HD technologies working at 3 OV. The sensors with 1 mm epoxy cover seem to be the ones that suffer the most from DCR, both when irradiated (E1C), but also new (E1A); the sensor without resin WR-L, on the other hand, has an intermediate trend between

silicon and epoxy resin, although a full evaluation is not possible because the sensor has been irradiated (there is no new counterpart).

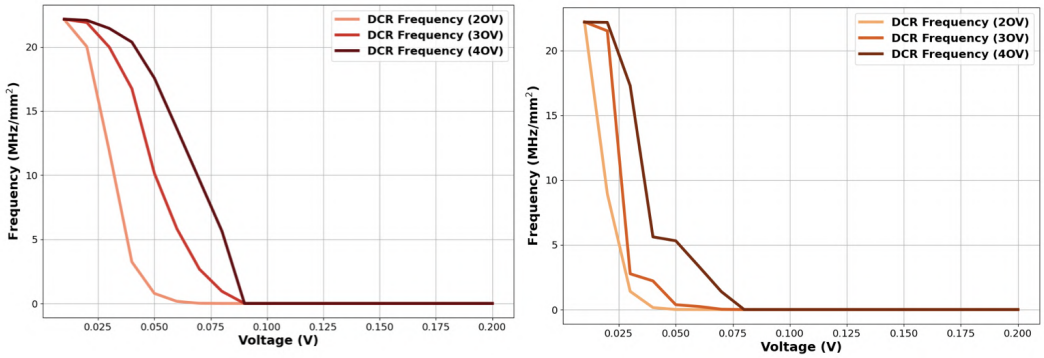

Figure 3.5: Figure shows the DCR as the threshold changes in amplitude for an irradiated sensor (a) and a not irradiated one (b) with the same resin coverage at different overvoltages.

Figure 3.5, on the other hand, show how DCR increases with overvoltage, both for irradiated (a) and not irradiated (b) sensors, which is consistent with what is expected since DCR should increase linearly with overvoltage. Finally, as expected, irradiation makes the DCR higher, also causing greater baseline fluctuation in sensors that have been hit by a charged particle beam: the analysis of these offline sensors requires greater cuts to isolate the signal region.

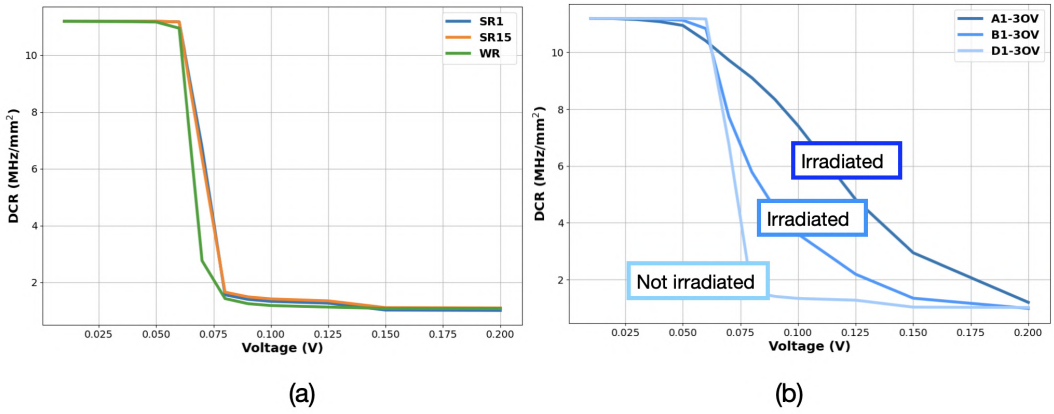

Figure 3.6: Comparison of DCR frequency at varying amplitude threshold for three unirradiated sensors of the NUV-HD-MT type with different coverage (a); difference between sensors of the same type, NUV-HD-MT with 1-mm silicon resin, where A1 and B1 are irradiated while D1 is not (b).

The same type of plot is shown in figure 3.6 for NUV-HD-MT type sensors; (a) shows the difference between three non-irradiated sensors with different resin coverage: the difference in behaviour appears negligible. This is particularly true for sensors with resin, where, despite the difference in cover thickness, the DCR trend appears identical. The difference between sensors of the same type (1 mm silicon resin) is reported (b), where A1 and B1 are irradiated, D1 is not; as expected, the first two have a higher DCR than the last. However, perhaps also due to different amounts of radiation, the two irradiated sensors show a DCR that changes differently with threshold. It is also worth noting that since the NUV-HD-MT SiPMs have larger amplitudes, the DCR does not go to zero at 200 mV as it did in the previous case, although it continues to decrease

as the amplitude threshold increases. Finally, a summary of all the analysed sensors and the observed DCR is given in table 3.2 ; NUV-HD-MT sensors show on average a lower DCR than the previous prototypes, which is compatible with the introduction of metal trenches to isolate the SPADs more.

Sensor:	SR15B	SR15D	A1	D1	WR-L	WR-64	E1C	E1A
$DCR(MHz/mm^2)$	0.37	10.15	9.10	1.57	17.65	1.43	17.67	3.94

Table 3.2: The DCR observed at 3 OV, with an amplitude threshold of 50 mV for NUV-HD and 75 mV for NUV-HD-MT.

3.1.2 IV curves

The IV (current-voltage) curve is one of the most important characterisation steps for a silicon detector operating under reverse bias; the aim is to determine the optimum operating voltage for the device. The main concern for SiPM is to observe the transition to Geiger mode, where a self-sustained avalanche process starts: this happens after a typical voltage value called the breakdown voltage V_{BD}.

3.1.2.1 IV setup

The instrumentation used includes a TDK Lamba Z100-2 power supply[55] and a Keithley 6487 picoammeter[56]. The circuit is as follows: the cathode of the sensor is biased with a positive voltage, while the anode is connected to the picoammeter to measure the current.

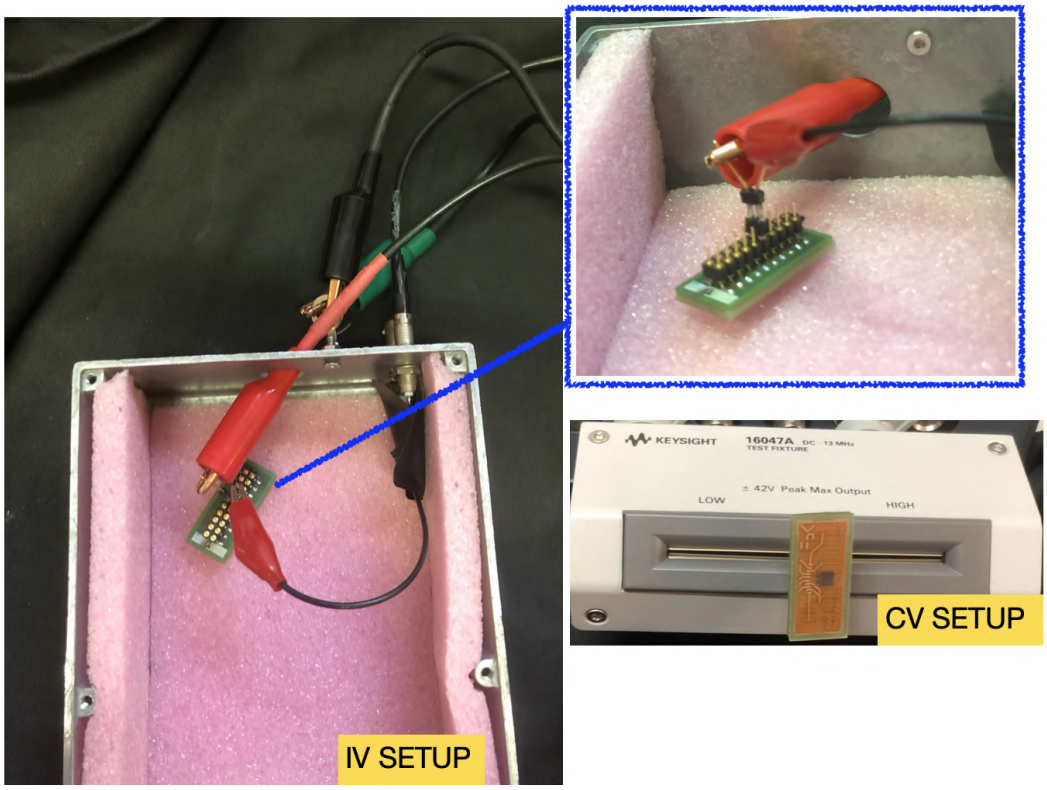

Figure 3.7: The experimental setup for the IV and CV characterization is shown in the picture.

The picoammeter uses a triaxial cable as shown in the figure 3.7; the current enters the red cable while the black cable is connected to ground. The green cable is an additional protection for the measurement, ensuring that the current flowing does not alter the results. The value of V_{BD} can be obtained from IV data using the Logarithmic Derivative (LD) and the Inverse Logarithmic Derivative (ILD) methods. The overvoltage OV refers to the extracted values of BD reported in table 3.3, while the breakdown values of all analysed sensors are given in the tables C.1 and C.2 in the appendix C.1.

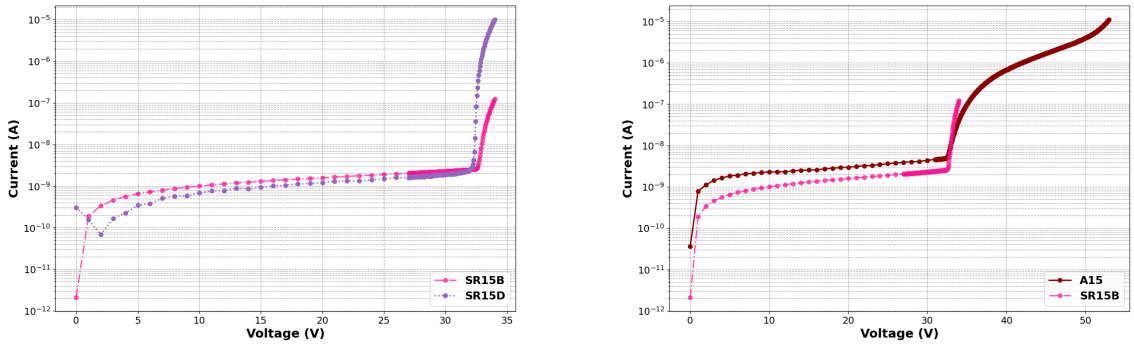

(a) (b)

Figure 3.8: Comparison between an irradiated and a not irradiated sensor (a) for the NUV-HD technology; comparison between two not irradiated sensors of the NUV-HD-MT technology and the standard NUV-HD one (b).

3.1.2.2 IV results

The obtained IV curves can be seen in figure 3.8. It is evident that sensors subjected to irradiation by charged particles reach much higher current values than new sensors; this can be seen in figure 3.8, (a), where a comparison between pairs of new and irradiated sensors with the same coverage is reported; the difference in current reaches two order of magnitude, with the latter which has a current of the order of 10 μA. Comparing two non-irradiated sensors belonging to different technologies (standard NUV-HD versus NUV-HD-MT shown in 3.8 (b), however, we see that the latter can withstand a much higher overbias, and consequently, also show an increase in current values. Again, the difference is about two orders of magnitude, with the NUV-HD-MT sensors reaching 10 μA, but much more gradually than and over a greater voltage range than the standard NUV-HD irradiated.

3.1.2.3 Method for Extracting the Breakdown Value

The value of V_{BD} is obtained from a fit of the data collected experimentally using primarily two methods [57]: the logarithmic derivative and its inverse function. The first method consists of calculating the derivative of the logarithm of the IV curves defined as following 3.1.1:

$$LD = \frac{dln(|I|)}{dV} \tag{3.1.1}$$

In the second case, we simply take the inverse function:

$$ILD = \frac{dln(|I|)}{dV}^{-1} \tag{3.1.2}$$

Below the breakdown value, LD depends linearly on the voltage with a positive slope; however, as we approach V_{BD}, it takes on a quadratic behaviour: a parabola is obtained with its vertex corresponding to the breakdown voltage. The same applies to ILD, where the slope is opposite: ILD has a minimum at the breakdown voltage, so its inverse, LD, will have a maximum. To extract V_{BD}, a parabolic fit is applied to both curves, and the minimum is sought over an interval centred around the breakdown voltage. The schematic representation of the two methods is shown in Figure 3.9.

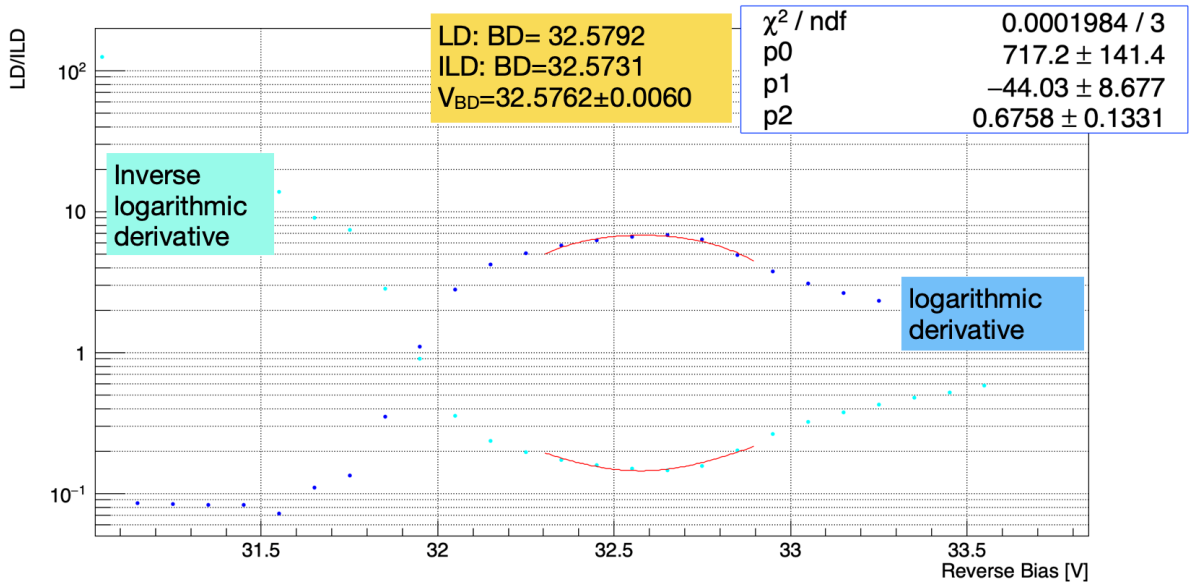

Figure 3.9: Schematic representation of the two methods to obtain the BD value for a SiPM.

In table 3.3, the extracted breakdown values are shown for a sample of the sensors analyzed (all the values are reported in tables C.1 and C.2 in the appendix). It can be seen that the V_{BD} is about the same for both the standard NUV-HD SiPMs and the NUV-HD-MT SiPMs, and it does not change when the sensor is covered with different thicknesses of resin (or if the resin is absent). What is important to point out is that the NUV-HD-MT SiPMs have a longer working range due to the presence of the metal trench that guarantees a greater isolation between pixels, as explained in the appropriate paragraph 2.1.5.2, but this feature does not change the value of the breakdown voltage.

Sensor type	*Sensor name*	*BD values (V)*
NUV-HD	SR1A	(32.4 ±0.1)
	SR15B	(33.0 ±0.1)
	SR3F	(32.9 ±0.1)
	WR-L	(32.6 ±0.1)
	E1A	(32.7 ±0.1)
NUV-HD-MT	A1	(33.1 ±0.1)
	A15	(33.1 ±0.1)
	A3	(32.9 ±0.1)
	WR55	(33.0 ±1)

Table 3.3: The breakdown values are shown for SiPMs of the type NUV-HD standard and NUV-HD-MT.

3.1.3 CV curves

The CV characterisation (capacitance-voltage) is another important preliminary tool from which the pixel capacitance, the effective doping concentration, the electric field and the depletion voltage can be extracted. The measurement are performed with a Keysight impedance analyzer [58] with a frequency of 200 kHz.

The CV curve should present two flexes: the first is before the breakdown voltage and occurs when the curve begins to decrease more slowly; the second occurs when complete sensor depletion is reached.

3.1.3.1 Sensors parameters from CV analysis

The analysis of the CV characteristic allows us to extract important parameters that characterize the sensor, such as the depth of the gain layer $W[\mu m]$, the doping profile of the sensor $D[cm^{-3}]$, and the behavior of the electric field. To do this, knowing ϵ_{Si}, the dielectric constant of silicon, and e, the elementary charge, we calculate the depth of the gain layer (equation 3.1.3):

$$W = \frac{\epsilon_{Si} \cdot A}{C_p} \tag{3.1.3}$$

where A is the area of the active region, which varies depending on the fabrication process.

The doping profile is given by equation 3.1.4:

$$D = \frac{dV}{d(\frac{1}{C^2})} \cdot \frac{1}{\epsilon_{Si} \cdot e \cdot A^2} \tag{3.1.4}$$

Once the sensor's capacitance is determined, it is also possible to estimate the gain, which is a fundamental parameter for semiconductor sensors. It represents an estimate of the charge deposited by the avalanche process following the arrival of a photon and is the same in every hit cell. It can be calculated by knowing the sensor's capacitance using equation 3.1.5, where V_{OV} is the overvoltage and C_{pixel} is the capacitance of each individual cell.

$$G = \frac{V_{OV} \cdot C_{pixel}}{e} \tag{3.1.5}$$

In the case of the NUV-HD standard sensors, each pixel has an area of 40 μm x 40 μm, while each sensor has an area of 9 mm^2. Therefore, the number of SPADs is approximately $N_{spad} = \frac{A_{SiPM}}{A_{SPAD}} \approx 5625$; the capacitance of the sensor after breakdown is about 750 pF, and $C_{pixel} = C_{sensor}/N_{spad}$. Substituting into equation 3.1.5, we find a gain of 3×10^6 at 4 OV and 2.4×10^6 at 3 OV, which is consistent with the expected values for an SiPM.

3.1.3.2 CV Results

The CV curves obtained are shown in figure 3.10; no difference is visible between irradiated and non-irradiated sensors. In all curves, the first inflection is clearly visible, unlike the second which cannot be seen, most probably, because the complete emptying of the sensor probably takes place at higher voltages; only in a few cases the beginning of the asymptotic region is visible, such as for the SR3F sensor in figure 3.10. In fact, these sensors work up to a maximum of 6V beyond the breakdown, and

increasing the voltage even further could cause damage to the device. However, the onset of breakdown is only visible in non-irradiated sensors, which usually have a more regular behaviour.

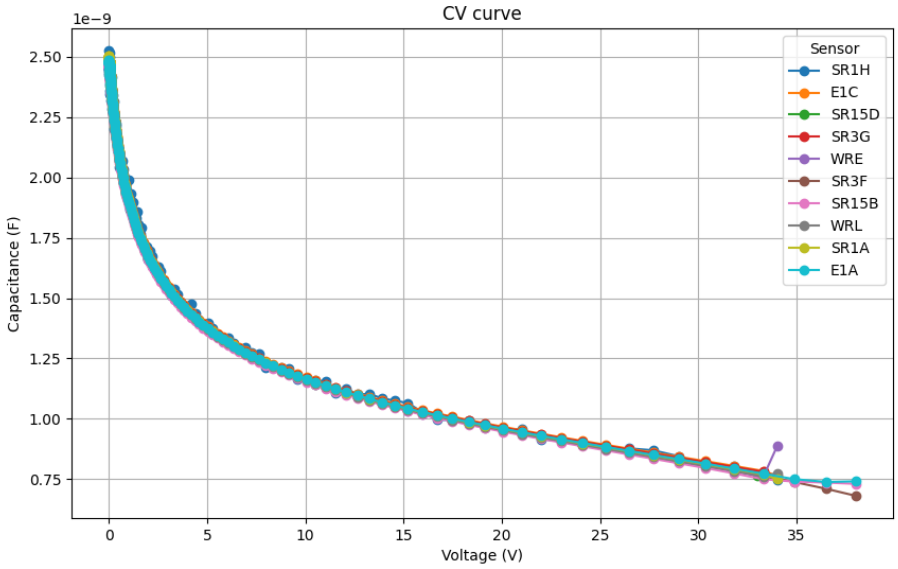

Figure 3.10: Capacitance as a function of voltage for different sensors are shown in the figure; the distributions are all comparable, both for irradiated and non irradiated sensors and for sensors with different thicknesses and different types of resin.

Figures 3.11 and 3.12 show the doping profile and electric field, respectively, extracted for a new sensor (a) and one irradiated (b) with the same resin cover (1 mm epoxy); it is evident how irradiation changes the distribution of doping, making it less uniform. In particular, a decrease in doping concentration is observed at the beginning of the gain layer, as one of the effects of irradiation is to inhibit the presence of boron in the p-doped semiconductors; this effect, however, does not affect the entire gain layer: a doping peak is nevertheless visible at the end of the gain layer, around 1μm, for both sensors.

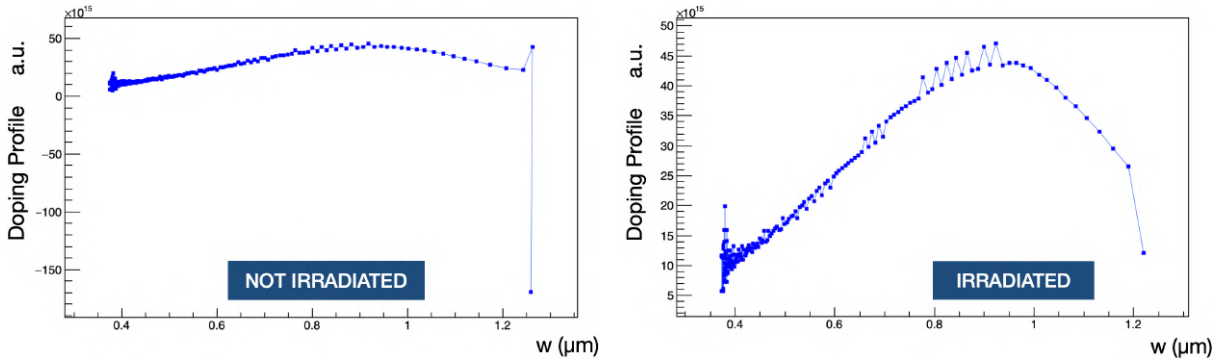

(a) (b)

Figure 3.11: Plot of doping profile as a function of position for not irradiated (a) and irradiated (b) sensors

The electric field, on the other hand, does not seem to be affected by the radiation, and shows a comparable distribution for the two sensors; in both cases it is evident how the electric field is peaked on the gain layer, which has a thickness of 1μm, and how it decreases outside it.

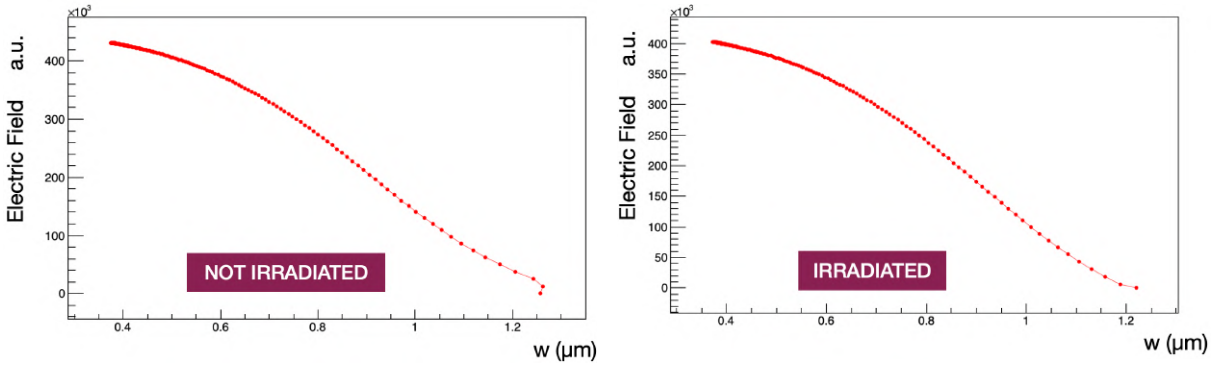

(a) (b)

Figure 3.12: Plot of the electric field as a function of position for not irradiated (a) and irradiated (b) sensors.

3.2 Time Resolution with a laser source

SiPMs are classically used as photodetectors, so their main characterisation are measurements using photon beams; the setup used for this type of measurement is illustrated in figure 3.13. The light is supplied by a picosecond pulsed laser of wavelength 1054 nm (PiLas PiL036XSM) [59] controlled by an IG2000DX controller.

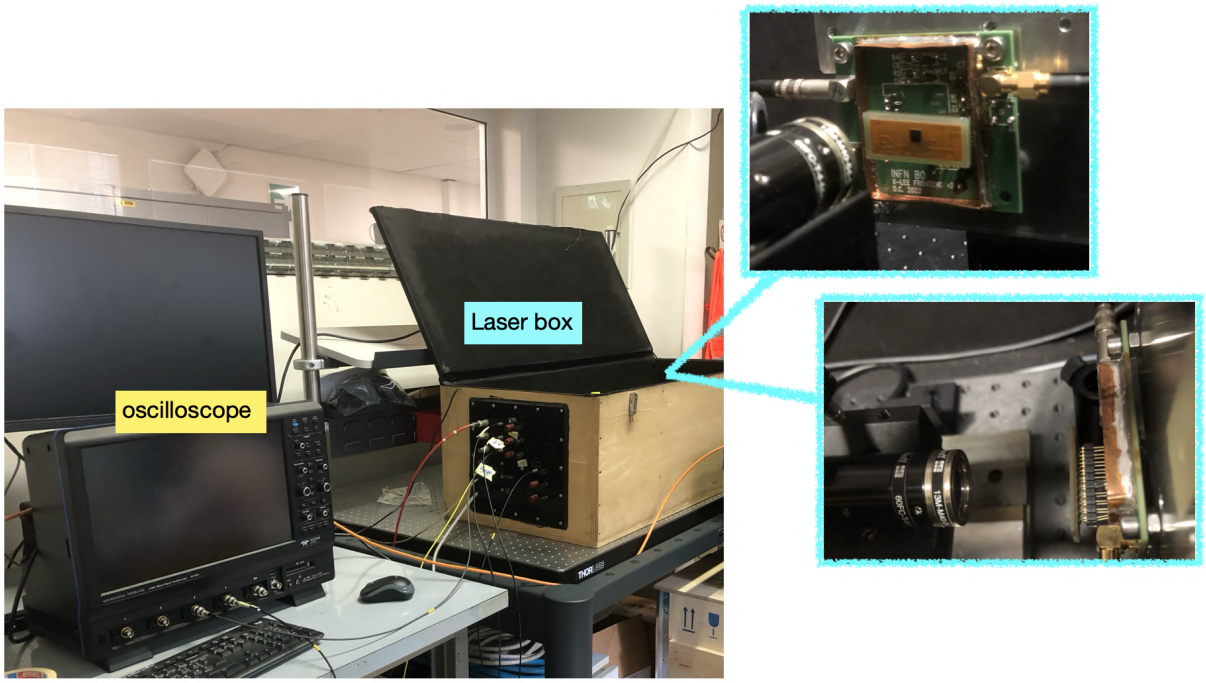

Figure 3.13: In the picture, the laser setup is shown.

The laser head is connected to a 1-metre single-mode optical fibre (Thorlabs P3-980A-FC-1) to direct the infrared photons into the black box where the sensor is located, but before reaching the sensor the light is collimated and focused by a combination of collimator and lens (Schafter & Kirchhoff 60FC-T-4-M40-54, Micro Focus Optics 13M-M40-54-S). These two optical objects are placed on a manually moving frame that permits to control the distance between the point of emission of the light and the sensor surface with a precision of 20 μm. The correct distance between the lens and the sensor is important for correctly focusing the micrometric laser spot. The

board to which the SiPM is connected is mounted on a two-axis Standa 8MT167-25LS micrometric positioning stage (MPS) [60], controlled by a LabView programme [61]; it allows the sensor to be moved along the x and y coordinates with micrometric precision to reach the correct laser position where the laser spot falls within the active area of the sensor. The signal provided by the passage of the laser is amplified by the Lee39+ amplifier [62] then read out on a Teledyne LeCroy Wave-Master SDA 816Zi-A [63] digital oscilloscope in the form of waveforms: each waveform constitutes a sequence, and the acquisition comprises several sequences that are then analysed offline. During the analysis, a series of cuts are imposed on the amplitude distributions to remove unwanted events, such as noisy ones. Typically, both a minimum and maximum acceptable amplitude limit are imposed: in the case of SiPMs, the first peak of the amplitude distribution, which is lower than the value associated with a SPAD (usually 10-20 mV), is usually cut, but no limits are placed on the maximum amplitude. Additionally, cuts are also imposed on the background distribution, which represents the amplitude in the 10 ns preceding the signal region. In this case as well, maximum acceptable values are set to mainly remove Dark Count events, i.e., signals with an amplitude greater than one SPAD but not due to any actual event. The amplification factor is about 40 dB, resulting from the series of two 17 dB amplifiers.

3.2.1 Preliminary measurements: amplitude distribution

Before extracting the time resolutions, a preliminary analysis on the amplitudes of the signals from six sensors was done to understand whether the responses to laser-emitted photons are comparable to each other.

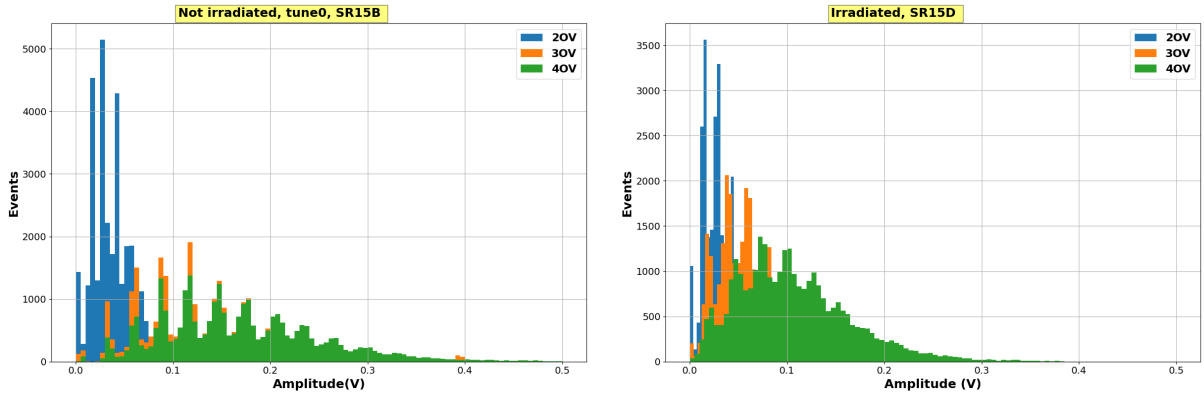

(a) (b)

Figure 3.14: The difference in amplitude distribution between a not irradiated (a) and irradiated (b) sensor; the amount of radiation integrated corresponds to 10^{10} $1MeV$ n_{eq}/cm^2. The main difference lies in the fact that in the latter the peaks corresponding to the hit SPADs are not as clearly visible as in the former.

The different tests include:

1. **Comparison between irradiated and new sensors:** the amplitude distribution of a never-irradiated sensor is shown in the figure 3.14a, in which we note that the peaks relating to the SPADs affected are clearly visible, as is an increase in the number of events at multiple SPADs as the voltage increases (the distribution therefore widens). In the amplitude distribution of the irradiated sensors, the peaks corresponding to the number of illuminated SPADs are not clearly visible as they are in that of the new sensors (figure 3.14b). This is probably due to the

fact that the irradiated sensors show an increase in DCR and a highly variable baseline that makes it difficult to observe repeatable values of the amplitudes. It must be emphasised that in both plots the baseline has already been subtracted, so it is the presence of noise that makes the peaks of the SPADs less visible. Moreover, even with the same applied voltage, it appears that the distribution of the irradiated sensor reaches lower amplitude values, demonstrating a different response to incident photons;

2. **Comparison of different resin thicknesses:** in figure 3.15a are shown the amplitude distributions for sensors covered with silicon resin of 1 mm, 1.5 mm and without resin. Since the source emits photons, we do not expect a difference in the response between the three cases, as is confirmed by the distribution. In fact, the photons do not interact with the resin layer except to be reflected or absorbed. In contrast, when the sensor is coated by a different type of resin (figure 3.15b the distribution appears different; the sensor coated by epoxy has an amplitude distribution shifted toward higher values than the silicon resin, but it is difficult to state whether it is because of a different effect of the resin, as it is difficult to recreate the same experimental situation each time. Nevertheless, not only is the amplitude of the signal associated with a SPAD different (around 50 mV for silicone resin versus 70 mV for epoxy resin), but the distribution of E1A also reaches up to 300 mV, versus 100 mV for SR15B.

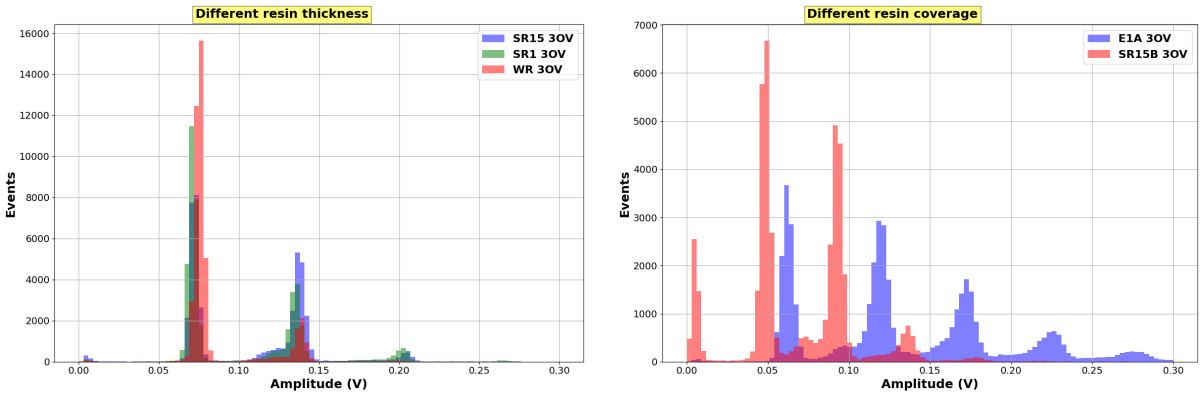

(a) (b)

Figure 3.15: Amplitude distribution for 3 different sensors covered with 1 mm, 1.5 mm silicon resin and without any resin layer (a); the distribution is similar in all three cases. (b) The same distribution is shown for one sensor covered with silicon resin (SR15B, red) and one covered with 1 mm epoxy (E1A, blue); in this case the distributions seem to change.

3. **Comparison to different laser tunes**: in Figure 3.16a the distribution of amplitudes is shown for different laser intensities, where "tune 0" corresponds to the maximum intensity, instead "tune 810" to the minimum intensity. As the laser intensity increases (the tune regulates the amplitude of the laser spot, as the amount of photons emitted), the emitted photons and thus the number of affected SPADs also increases. However, the difference in the distribution is most noticeable between the maximum and minimum intensities but no gradual decrease is observed as the intermediate and tune 0 distributions overlap. On the other hand, we note that amplitudes at tune 810 do not exceed 100 mV, while they reach as high as 300 mV at other laser intensities;

4. **Use of a filter and diffuser:** the objective of this test is to limit the number of photons hitting the sensor since we want to estimate the single photon time

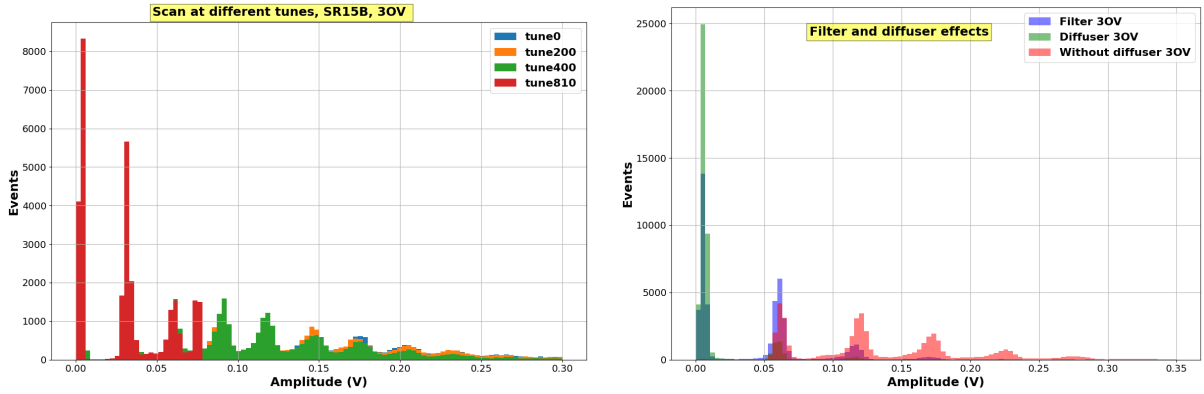

(a) (b)

Figure 3.16: Amplitude distribution as the laser intensity changes (a); amplitude distribution changes when a filter or diffuser is used to limit the number of photons hitting the sensor (b).

resolution (SPTR). The filter constitutes an absorbing material that absorbs part of the photons, while the diffuser deflects the photons by an angle of about 45°; the result in both cases is that a smaller number of SPADs are expected (figure 3.16b). The diffuser in particular greatly limits the number of photons arriving because most of them fall outside the sensitive area of the sensor, as is evident from the spike in zero in the histogram of amplitudes in figure 3.16b. The number of pixels affected varies from zero in the case of the diffuser, to five (although with few events) with nothing in front of the sensor. It means that using the diffuser the sensor is completely inefficient to detect photons.

3.2.2 Tuning the laser for SPTR

Single photon time resolution is measured by trying to hit as few SPADs as possible with the laser. However, this condition is very difficult to achieve due to the possible reflection and scattering processes that come into play when the photon hits the sensor. The focal distance of the laser is 3.44 cm and has been calculated using an LGAD as a reference. The laser is considered to be well aligned when it hits no more than three or four SPADs, as can be seen in the figure 3.17; first of all, an attempt is made to hit the centre of the sensor by scanning in position, both along the x-axis and y-axis, and looking for the extremes, i.e. the points where the signal disappears. Next, we move the source closer to or further away from the sensor to look for the point where fewer SPADs are hit.

3.2.3 Time Resolution: some results

The time distributions are given by the difference of the time at which the SiPM exceeds a fixed threshold in amplitude, usually slightly more than half of the signal of a single SPAD, and the time at which the laser signal exceeds 50 per cent of its amplitude. The time resolutions were extracted as standard deviations of the q-gaussian fit (see Equation 3.2.1) on the time histograms; the laser contribution to the timing resolution is considered negligible, so the extracted value is the timing resolution of the sensor.

$$f(x) = \begin{cases} p0\left[1-(1-p2)\left(\frac{1}{3-p2}\right)\frac{(x-meanPeak)^2}{p1^2}\right]^{\frac{1}{1-p2}}, & \text{if } x \leq meanPeak, \\ p0\left[1-(1-p3)\left(\frac{1}{3-p3}\right)\frac{(x-meanPeak)^2}{p1^2}\right]^{\frac{1}{1-p3}}, & \text{if } x > meanPeak. \end{cases} \tag{3.2.1}$$

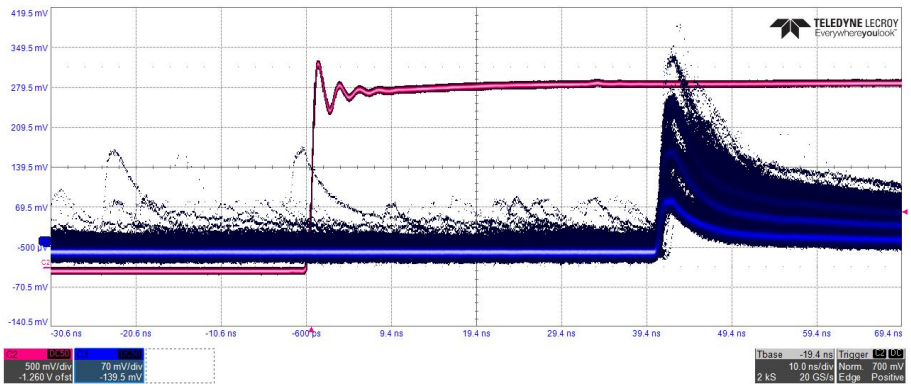

Figure 3.17: The figure shows an example of a signal seen on the oscilloscope by the SR15B sensor; in this case at most 4 SPADs are hit, so the laser is well focused. The laser trigger always arrives 40 ns before the photon beam and the events occurring before the signal region are due to dark counts, as showing less than 2 SPADs fired.

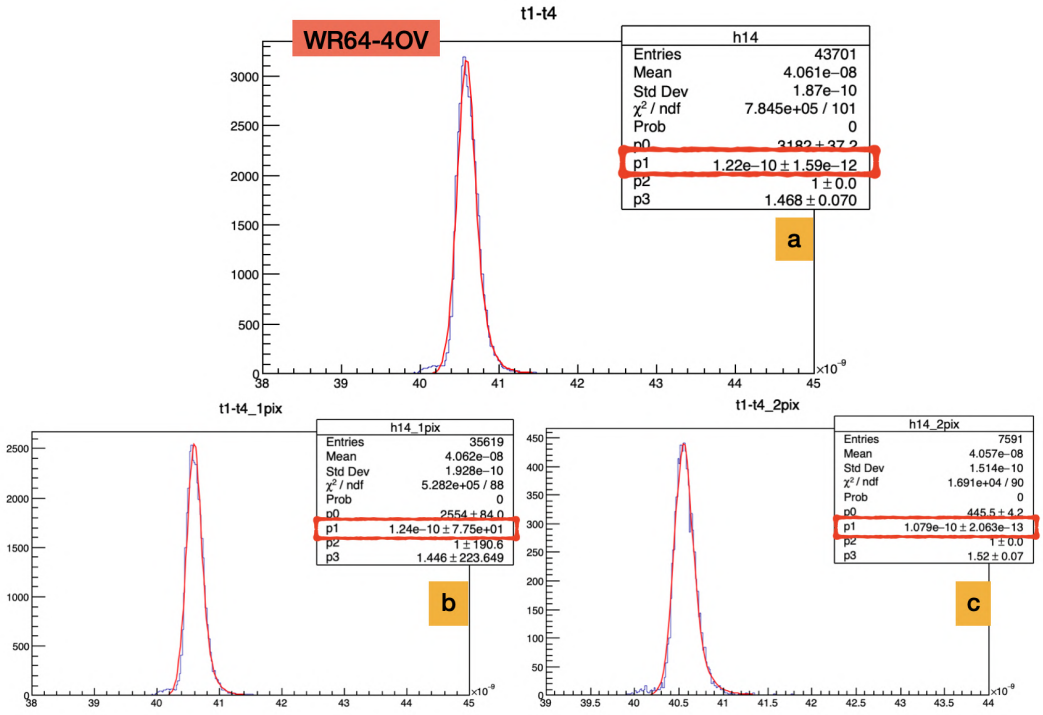

Figure 3.18: The timing distribution for the NUV-HD-MT WR64 sensor is shown in the figure; in this case the laser hit only two SPADs, with 83% of the events in the first pixel.

The time at which the signal overcomes the fixed threshold is calculated with a linear interpolation as shown in equation 3.2.2, where j is a variable indicating the binning of the waveform's points saved on the oscilloscope and $fixTH[i-1]$ is the threshold for each channel of the oscilloscope. The resulting time is calculating in the raising edge of the signal and corresponds to the time when the signals falls below the threshold, as $amp_j < fixTH[i-1] + bkg$.

$$fixtimeTH = time_j + \frac{(time_{j+1} - time_j)}{(amp_{j+1} - amp_j)} \cdot ((fixTH[i-1] + bkg) - amp_j) \qquad (3.2.2)$$

The uncertainty on the resolution was calculated by considering different sensors analysed at different overvoltage, and considering the maximum and minimum value

obtained in each situation; in particular, for each configuration, the percentage error obtained was calculated as given in equation 3.2.3, and the average value obtained is 5%.

$$\frac{\Delta_\sigma}{\sigma} = \frac{\sigma_{max} - \sigma_{min}}{2} \cdot \frac{1}{\sigma_{max}} \tag{3.2.3}$$

An example of a fit on the histogram of the time distributions is shown in figure 3.18 for the resin-free WR64 sensor, with which the best time resolution value was obtained. In this case, the laser only hits two SPADs and furthermore, most events only hit one SPAD. The fit seems to fit the data very well and the distribution is narrow, as shown by the value of the parameter $p1$ in the figure, which represents the temporal resolution. The fit becomes more problematic for sensors with resin, where not only do the distributions become wider, but there are also more SPADs hit (with lower statistics as the number of SPADs increases.

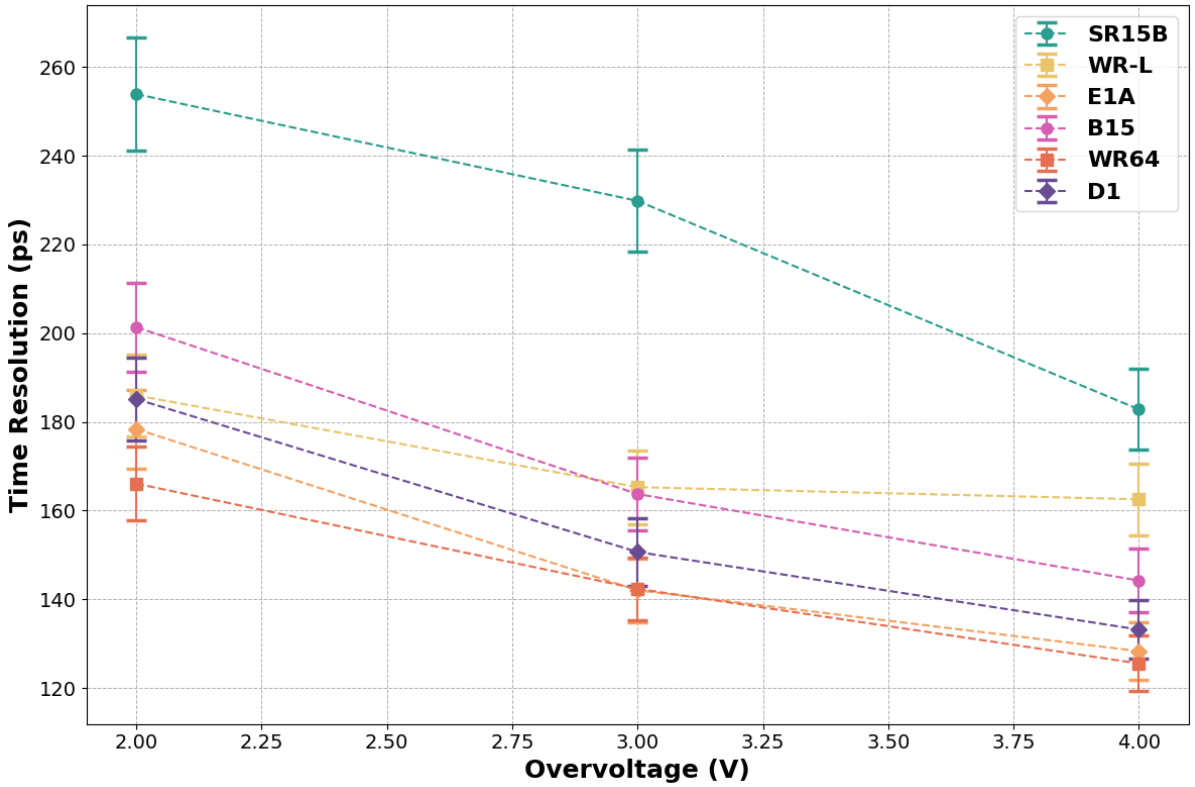

Figure 3.19: Time resolution for all sensors analyzed in the configuration without filter.

Furthermore, the distributions resulting from the use of a diffuser or filter are also wider and more complicated to fit, and a study of resolution as a function of the number of SPADs is complicated because photon detection is inefficient, as many events fall outside the sensitive area of the sensor. These concepts are discussed in more detail below where time resolutions considering all the events collected were studied in different configurations:

1. **At different OV**: figure 3.19 shows the time resolution of different sensors as a function of overvoltage; figure 3.20 shows the difference in resolution between irradiated and non-irradiated sensors as overvoltage increases. The time resolution improves as the overvoltage increases because the number of SPADs affected increases, with a difference of more than 25%;

2. **Comparison among irradiated sensors and not irradiated**: In figure 3.20, the change of timing resolution when without resin sensors are subjected to irradiation is visible. The most consistent effect of irradiation is to increase the dark count frequency, thus increasing the probability of observing events unrelated to the passage of the laser beam. This effect seems to deteriorate the timing resolution, since the not irradiated sensor show a better time resolution of 10% at 2 OV and of 18% at 4 OV. In the latter case, from the 165 ps of the irradiated sensors, the valued decreases to 135 ps for the not irradiated one;

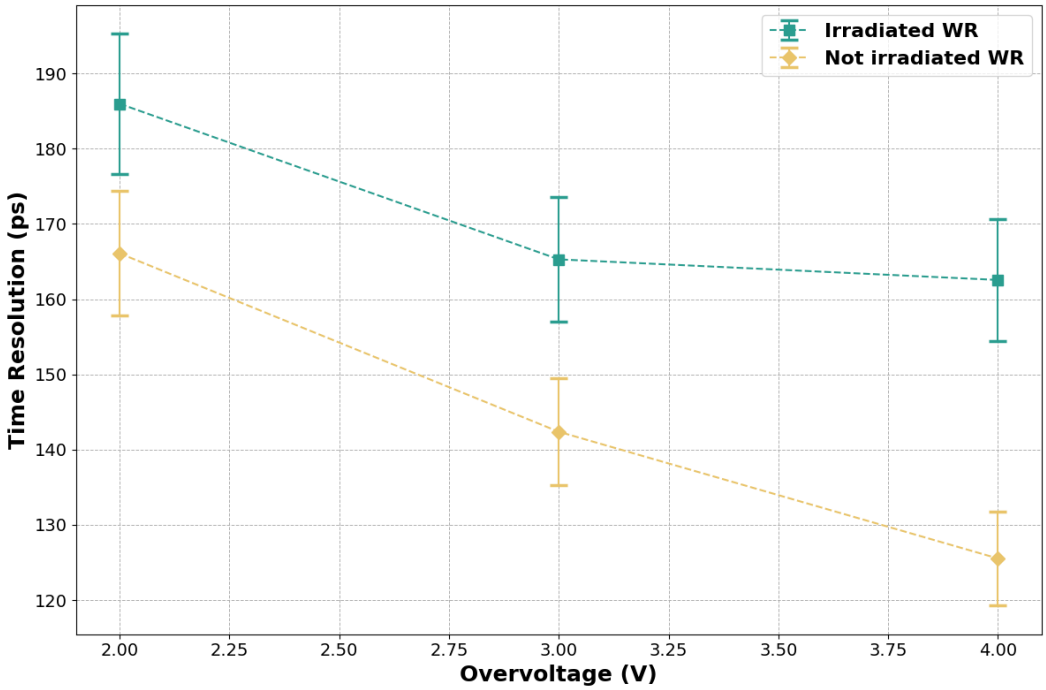

Figure 3.20: The difference in timing performance between a new and an irradiated sensor, both without resin.

3. **With filter or with diffuser**: Figure 3.21 shows the time resolution values using a filter, a diffuser or without either as a reference. The last configuration seems to provide the best results, most likely because the time resolution improves as the number of SPADs that contribute to the formation of the signal increases. In particular, the diffuser seems to include additional reflections and scattering processes that increase the probability of observing events that are not due to the laser trigger. The improvement in timing resolution for the configuration without any filter or diffuser is evident at 4 OV, where the value decreases from 240 ps (diffuser) to 130 ps;

4. **Comparison among NUV-HD and NUV-HD-MT**: In general, NUV-HD-MT sensors show better timing performance, as is shown in figure 3.22a. This is particularly evident for sensors with 1.5 mm resin, perhaps because greater isolation between pixels decreases noise events due to photon deflection in the resin. Among the NUV-HD sensors only the sensors with the epoxy resin show comparable performance with the NUV-HD-MT technology. The performance of the WR-L sensor is certainly affected by irradiation (at least 10^9 1 MeV/n_{eq} received during test beam campaigns), but the WR64 sensor, which has never received any charged particles irradiation, achieves values in line with what is expected;

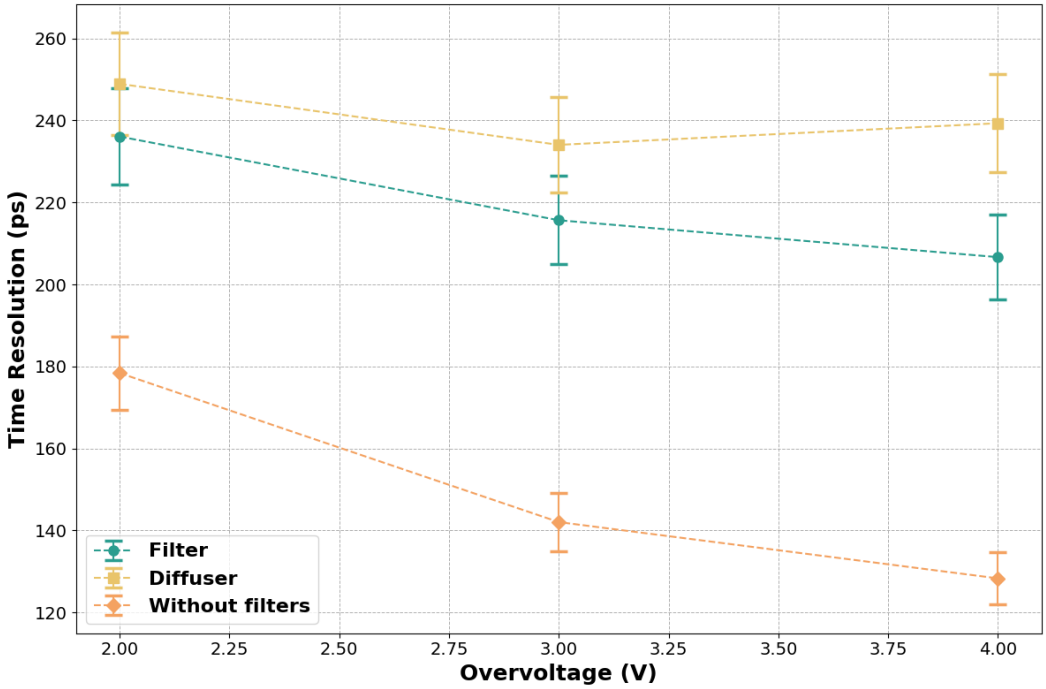

Figure 3.21: The effect on temporal resolution of using filters or diffusers in front of the laser photon source.

moreover, the timing performance of WR-L is better than sensors with protection layer of the same technologies. It is not possible to have a direct comparison with the previous prototype without resin before irradiation, however, even in the current situation the observed temporal resolution is still better than with the SR15B. In fact, the presence of the resin not only influences the path of the photons, but should also slightly modify the laser focus; measurements were made by changing the distance between the source and the sensor each time by an amount equal to the thickness of the resin, but this distance was not always suitable (an unfocused spot is very large and activates many SPADs) and it was difficult to find the most appropriate position. To better understand the difference between the two technologies, consider that SR15B achieves a resolution of 160 ps at 4 OV, while B15, of NUV-HD-MT technology goes down to 130 ps. E1A and WR64 achieve the lowest values for the two categories, both slightly above 120 ps. However, the standard technology sensors show a less linear trend with overvoltage, unlike the MT sensors in which resolution always increases as the applied voltage increases: the most obvious improvement can be seen in B15, which goes from 200 ps at 2 OV to 150 ps at 4 OV;

5. **Comparison among different types of protection layer resins**: Figure 3.22a shows the comparison between sensors with different resin coverage. In particular, the comparison is made between sensors with silicone resin (1.5 mm), epoxy resin (1 mm) and no resin. The silicone resin seems to return the higher resolution, perhaps also due to the greater thickness that introduces a photon scattering component. This is also confirmed by the plot in figure 3.22b, where the same comparison is shown for for SIPM of NUV-HD-MT technology; in this case the sensor with 1 mm resin has silicone resin, not epoxy. However, the two sensors with 1.5 mm resin are those with the worst temporal resolution. The fact that the resin introduces some photon scattering is also confirmed by the fact

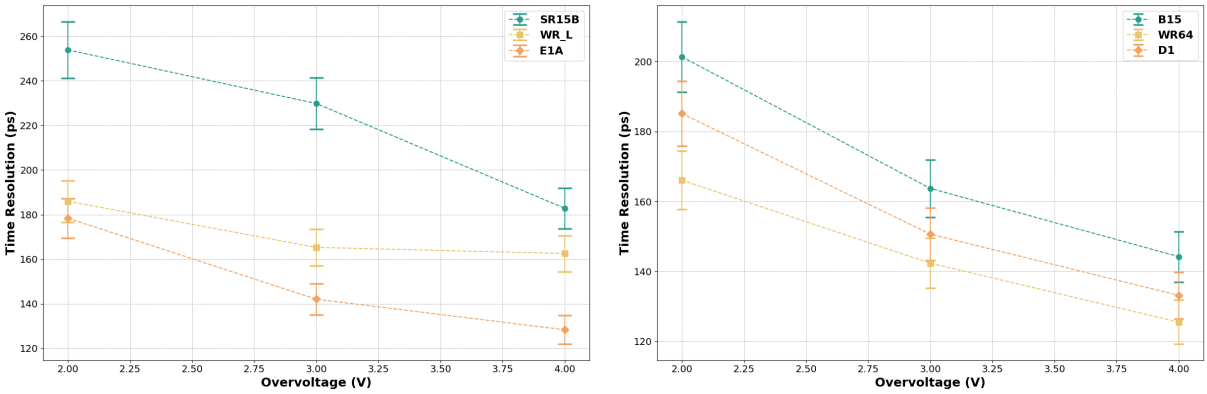

(a) (b)

Figure 3.22: The different sensor responses when covered by different types and different thicknesses of resin (or without resin) for NUV-HD SiPMs (a); the same comparison is shown for NUV-HD-MT SiPMs (b) but only by varying the resin thickness (silicon resin or without resin), since epoxy resin is not available for this technology.

that the sensors without resin have better time resolutions: the NUV-HD-MT sensor WR-64 reaches 120 ps at 4 OV, while the standard NUV-HD sensor WR-L reaches an higher value (160 ps) probably due to irradiation;

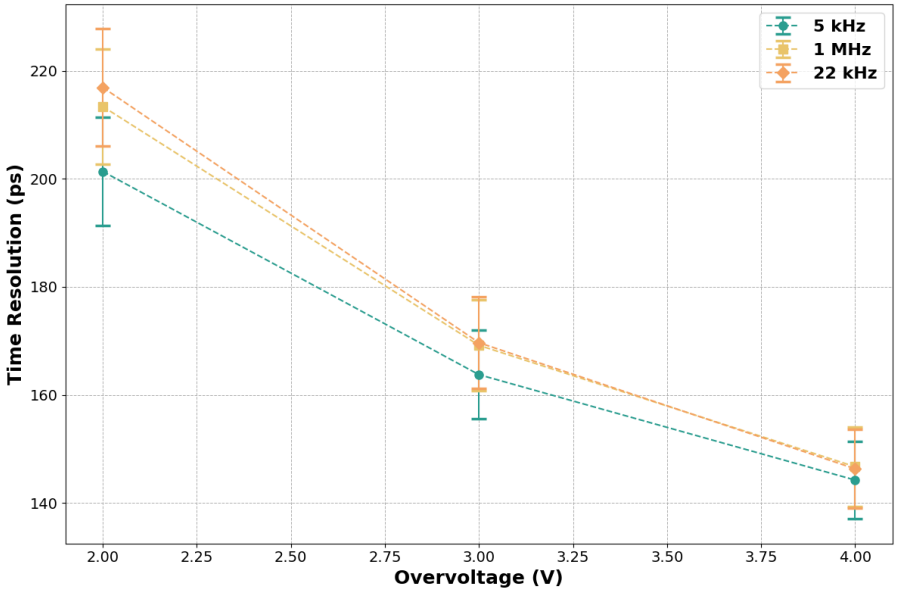

Figure 3.23: Figure shows the time resolution as the trigger frequency changes for the NUV-HD-MT B15 sensor.

6. **Comparison at different trigger frequency**: Figure 3.23 shows the timing resolution at different trigger frequencies for the NUV-HD-MT B15 sensor; the temporal resolution improves as the frequency decreases, as it is evident at 2 OV, passing from 215 ps at 1 MHz to 200 ps at 5 kHz. This is due to the fact that as the frequency at which the laser emits photons decreases, so does the probability of observing uncorrelated events, which thus constitute noise. The time distribution then, as can be seen in figure 3.23, also narrows as the frequency decreases: when the trigger frequency gets closer to the DCR, the number of noisy events increases. Finally, the difference at 4 OV is negligible.

3.2.3.1 Time resolution as a function of fired SPAD

The following section aims to analyse how timing resolution changes as a function of the number of SPADs hit; in general, a well-focused laser source should hit a few SPADs, possibly only one, to study single-photon temporal resolution. In fact, sensors without resin not only show better temporal performance, but also fewer SPADs hit, indicating a more focused source; this configuration is then assumed to be correct also for sensors with the protection layer, where some scattering effects enter. However, even if the laser spot is smaller than the pixel area, it is difficult to achieve this configuration, mainly due to the scattering that photons undergo when passing through the resin. In general, as shown in figure 3.24, the time resolution generally improves as the number of pixels hit increases. Usually, as the overvoltage increases, not only does the signal amplitude increase, but it is also more likely to observe more pixels being turned on, especially in sensors with resin. The improvement of time resolution both with OV and with the number of SAPDs fired is shown in figure 3.24a for the NUV-HD-MT technology, where it reaches 120 ps. In standard NUV-HD technology sensors (figure 3.24b), however, the trend in resolution with the number of SPADs seems less linear, although in general, resolution improves as the number of SPADs hit increases; it also improves as the applied voltage increases. The more discontinuous trend in the figure 3.24b is perhaps due to the lower isolation between SPADs; however at 4 OV, the trend becomes more stable, and the resolution stabilizes at around 160 ps.

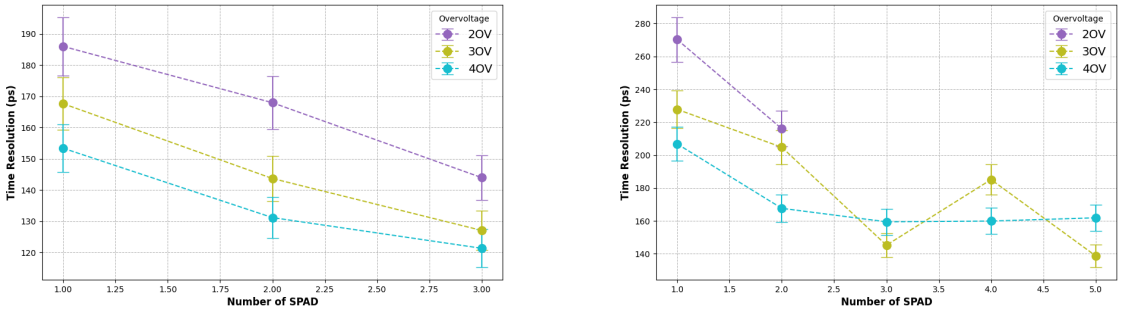

(a) (b)

Figure 3.24: Time resolution as a function of the number SPADs fired for a NUV-HD-MT sensor with 1.5 mm resin for different overvoltages (a); the same plot for a NUV-HD sensor with 1.5 mm resin (b).

Figure 3.25 shows the time resolution as a function of number of SPADs fired for different sensors, both NUV-HD-MT (a) and NUV-HD (b) at 4 OV; in general, the sensors with 1 mm of resin shows better performance than those with 1.5 mm of coverage, as had already been observed 2.

In figure 3.25a we see how the resin-free sensors of the NUV-HD-MT technology offer the best temporal resolutions despite the fact that there are only two SPADs hit, reaching values down to 110 ps, better of the 15% than sensors with 1.5 mm of resin; the fact that the number of SPADs hit does not increase with overvoltage could indicate that the laser was well focused and hit at most two SPADs, while still reaching a very good resolution value. In addition, we observe that NUV-HD-MT sensors, which have more isolated pixels, have fewer pixels hit, possibly for the better isolation guaranteed by the technology (reduction of Cross Talk CT). In figure 3.25b, on the other hand, we can observe how the sensor with the epoxy cover offers very good timing performance; we also note that in the case of the epoxy cover we observe many more pixels affected, with again decreasing time resolution as the number of SPADs that

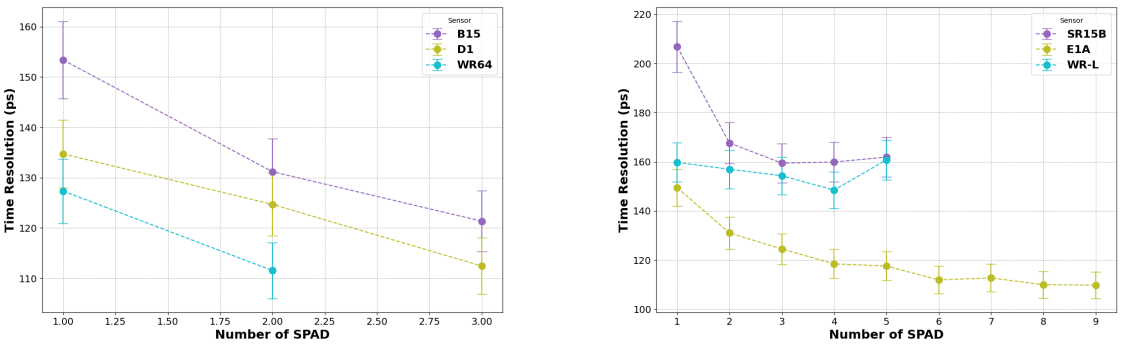

(a) (b)

Figure 3.25: Comparison of time resolutions of NUV-HD-MT sensors at 4 OV with different coverage and different resin thicknesses as the number of hit pixels changes (a); the same plot is shown for NUV-HD sensors (b) at 4 OV at varying resin thickness (1 mm in silicon, 1.5 mm in silicon or no resin). For both the technologies, any filter or diffuser was used.

have fired increases. The resolution reaches 110 ps with 9 SPADs fired; it also evident a difference of 40 ps at 5 SPADs fired compared to SR15B (160 ps for the latter).

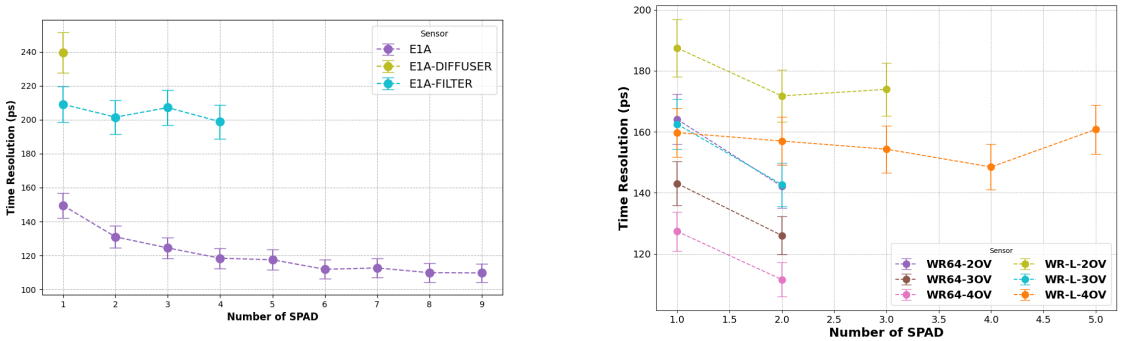

(a) (b)

Figure 3.26: Comparison of timing resolution as a function of the number of SPADs for different configurations in which a filter, a diffuser or nothing, at 4 OV had been applied in front of the sensor (a); comparison at different OV for an unirradiated NUV-HD-MT sensor and an irradiated NUV-HD sensor without resin varying the overvoltage (b).

Finally, figure 3.26a shows the temporal resolution as a function of the number of SPADs hit even when the filter or diffuser is placed between the sensor and the laser source; since the photons are deflected or absorbed, we see that the number of pixels hit is lower. In addition, the resolution values worsen even of the 36% and uncertainties increase due to the few events recorded; in particular, the use of the diffuser makes performance much worse because it deflects the photons beyond the sensitive area of the sensor. In figure 3.26b, on the other hand, we see the comparison between an unirradiated NUV-HD-MT sensor and an irradiated NUV-HD sensor; as expected, the timing performance is better in the former case, passing from 160 ps for the irradiated sensor to 110 ps for the not irradiated at 4 OV. A less stable behaviour is also visible in the former, with the resolution values that seem not always improving as the number of SPADs affected increases: however, due to large uncertainties (indicating that many events were removed during analysis due to the increased noise caused by the irradiation) it cannot be excluded that the behaviour is in any case compatible with what is expected.

3.3 Charged particles beam

In the following section, the results obtained by irradiation from charged particles with a 10 GeV/c MIPs (Minimum Ionizing Particles) beam at the T10 beamline of the Proton Synchrotron (PS) beam facilities at CERN will be analysed; the beam was mainly protons (πs at lower energies). The apparatus is shown in figure 3.27. mainly protons (pions at lower energies)

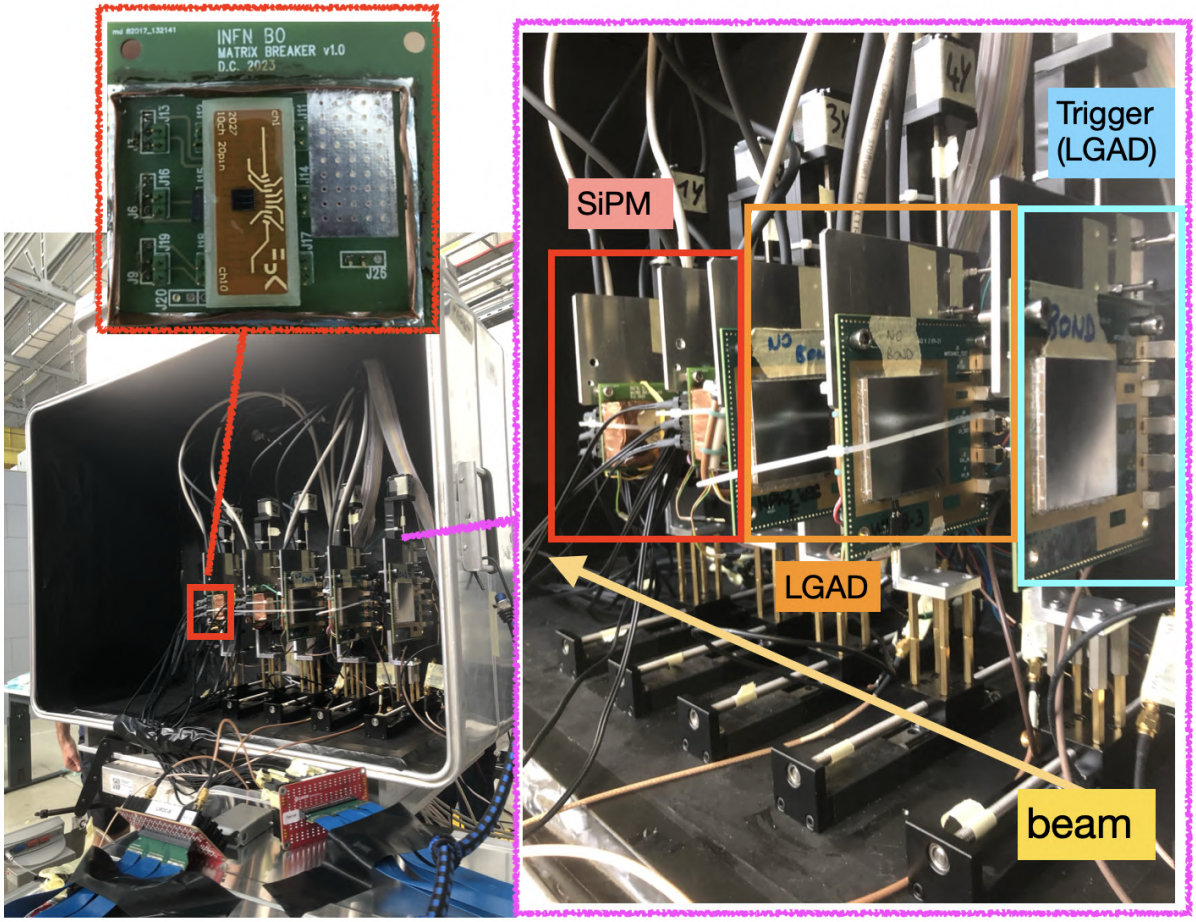

Figure 3.27: Schematic of the setup used at CERN beam facilities for charged particle beam studies. Only two LGADs are acquired at the oscilloscope, one as a trigger (blue) and the other as a time reference (one of the two in the orange box), respectively. The digital readout, on the other hand, requires all five sensors.

The preliminary analysis is the study of amplitudes and waveforms, where it is evident that irradiation by charged particles produces much larger signals than the laser source. Furthermore, the temporal resolution is studied for different sensor categories. In the final section, a comparison in the case of a beam at an energy of 1.5 GeV is also included (in this case, the beam composition is slightly different, see 3.3.5). Several sensors were analysed for this study: the SiPM-MT A1 and A3 with 1 mm and 3 mm resin, respectively, and the NUV-HD standard SR15D, SR3G and SR1H with 1.5 mm, 3 mm and 1 mm resin, respectively; the latter was acquired in comparison to a sensor WR-L without resin where the passage of charged particles induces no Cherenkov light. The telescope was made of four sensors: two SiPMs under test and two LGAD detectors (1x1 mm^2 area 50 μm thickness or 25 μm of thickness and 1.3x1.3 mm^2 area); the latter are used as trigger for the beam particles and as reference to evaluate

the time resolution of the SiPM, respectively. The whole setup was enclosed in a dark box at room temperature. It is worth noticing that during the tests, the temperature ranged between 30 and 38 degrees which is higher compared to the characterization temperature usually employed for SiPMs. For the cooling, Peltier cells are coupled to each sensor. The SiPMs signals were independently amplified by two Lee39+ [62] with gain factor of about 40 dB. The trigger was defined as the coincidence of the two LGADS in the telescope. At each trigger, all four waveforms were stored using a Teledyne LeCroy Wave-Master SDA 816Zi-A oscilloscope [63]. As already described in the 3.2 section, acquisition takes place in the form of waveforms in a given time interval, which are then analysed offline by adjusting the baseline and imposing cuts on the signal region to be studied.

3.3.1 Amplitude distribution

The amplitude distributions for the NUV-HD-MT sensors are shown in figure 3.28 for the sensor A1 with 1 mm resin (a), and the A3 with 3 mm resin (b). As expected, the charged particles induce greater signals as the resin thickness increases: the distribution for sensor A3, is shifted towards greater amplitude values, also above 1.4 V; moreover, in the latter case it is much more evident how the distribution widens as the overvoltage increases. In general, for sensor A1 the peak of the distribution is shifted towards lower amplitude values, as is evident in particular when looking at the blue curve in figure 3.28a: at 2 OV the peak of the distribution is quite below 1 V. However, higher signals also induce greater noise, as can be seen in the small peak at low amplitudes (around 200 mV) visible in 3.28b, which is instead absent in (a).

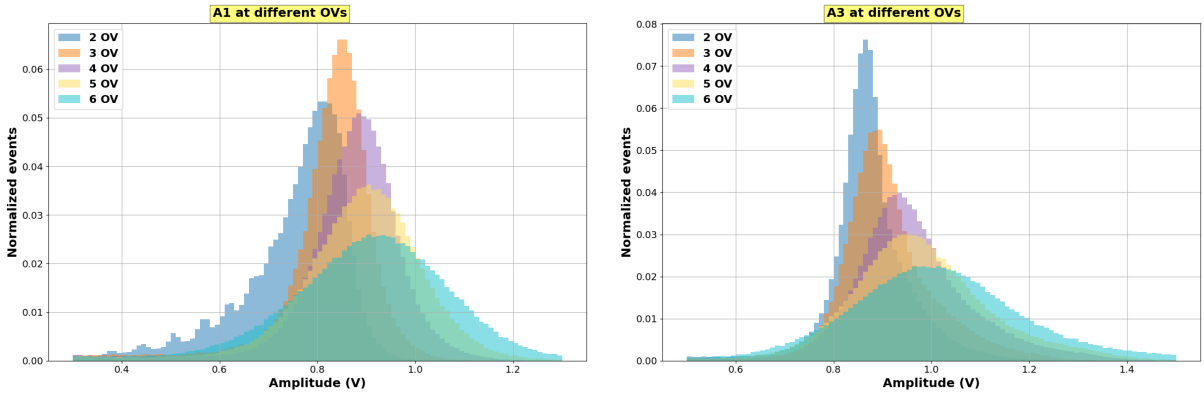

(a) (b)

Figure 3.28: Distribution of amplitudes for NUV-HD-MT A1 and A3 sensors, with 1 mm (a) and 3 mm (b) resin, respectively.

Similarly, the distribution of amplitudes for the standard NUV-HD sensors with 1.5 mm and 3 mm resin is shown in figure 3.29a and figure 3.29b, respectively; again, the distribution of the SR3G SiPM is wider and shifted towards higher amplitudes. The peak is around 900 mV for SR15D and aroud 1 V for SR3G. Also, for both sensors the distribution widens as the overvoltage increases because the signals become larger.

Finally, figure 3.30 shows the amplitude distributions for a sensor without resin (a) and for a sensor with 1 mm of resin (b). In the first case (a), due to the absence of the resin, we see that the amplitudes of the signals are very small and unlike the previous cases, the sensor is not in saturation so the individual SPADs affected are visible.

In fact, without the resin, the charged particle does not produce Cherenkov radiation and events with more than one SPAD activated are due to intrinsic noise (2). On the

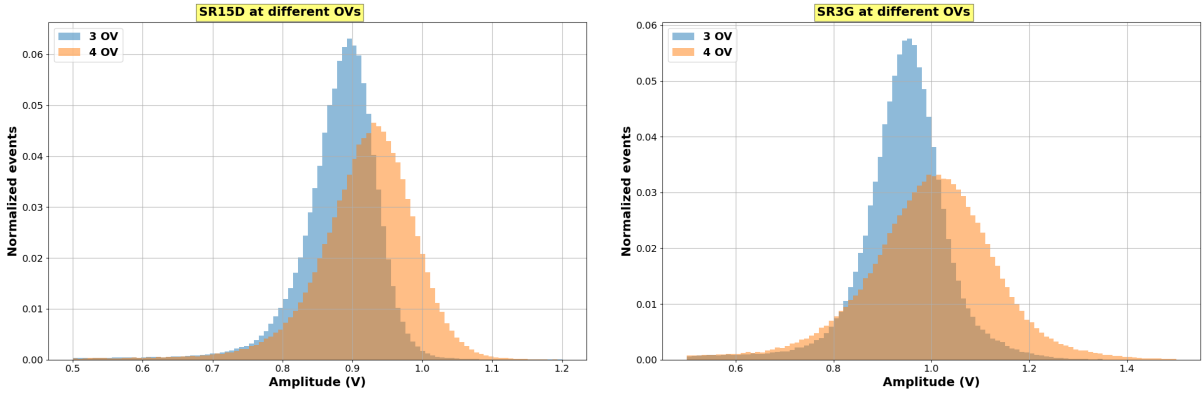

(a) (b)

Figure 3.29: Distribution of amplitudes for standard NUV-HD SR15D and SR3G sensors, with 1.5 mm (a) and 3 mm (b) resin, respectively.

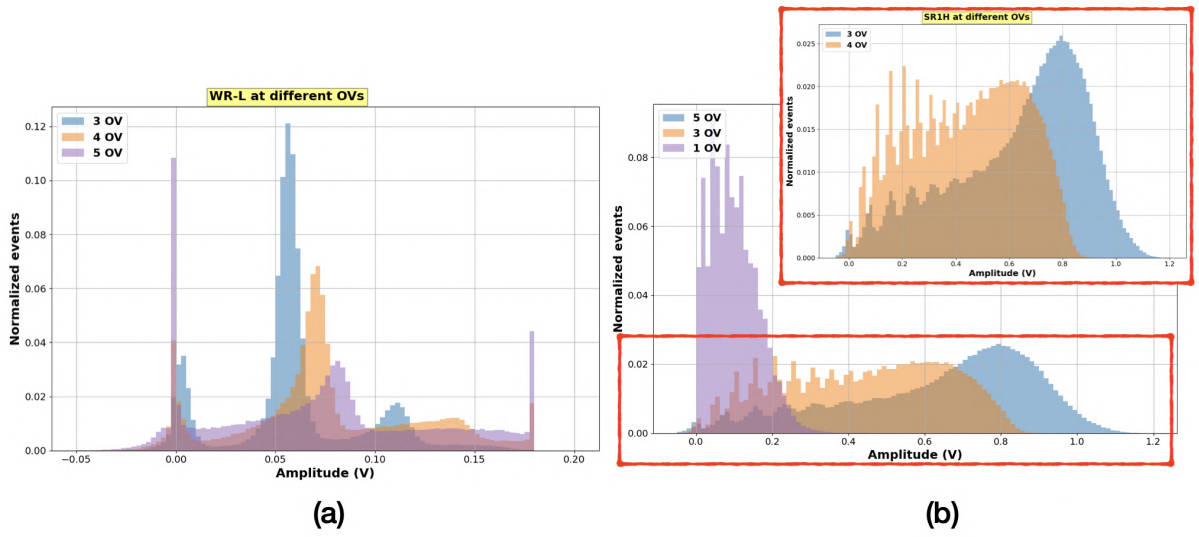

(a) **(b)**

Figure 3.30: The distribution of amplitudes for standard NUV-HD WR-L and SR1H sensors, with no resin (a) and 1 mm of resin (b) respectively, is shown in the figure. A zoom of the SR1H sensor distribution for voltage values exceeding breakdown is also shown in (b).

other hand, figure 3.30 (b) shows the distribution for the sensor with 1 mm of resin: in one case it shows three different voltages (b), one of which is very close to the breakdown voltage; in fact, we can see that the amplitudes are much smaller than for the other two voltages, and that the interval in which the events are distributed is very narrow, slightly exceeding 200 mV. On the contrary, in (b) also the zoom of the distributions of the amplitudes at the two voltages that exceed the breakdown voltage is shown; as expected, the distribution widens towards higher amplitude values, even above 1 V, indicating also that there are a lot of fired SPADs. In all three cases, even for the SR1H sensor, unlike those examined previously, the peaks associated with the SPADs affected are visible, indicating that the sensor was not completely saturated. Unlike a beam of photons, which is usually better collimated, a charged particle beam produces a cone of Cherenkov photons that activates several pixels and we observe a majority of events at higher amplitudes: it is no longer possible to distinguish peaks from around 9 affected pixels onwards. However, being able to distinguish peaks at a few hit SPADs allows us to study how the temporal resolution varies with the number of pixels hit.

3.3.2 Noise analysis

To understand how noisy a sensor is in presence of beam [1], we analyse the background distribution, obtained as signals of lower amplitude above the baseline in the region preceding the particle's true signal: this is usually calculated in the preceding 10 ns as given in equation 3.3.1.

$$rms_{Bkg} = \sqrt{\frac{A_{Bkg}^2}{N_{points}} - \frac{A_{Bkg}^2}{N_{points}^2}} \tag{3.3.1}$$

where A_{Bkg} is the amplitude calculated in the 10 ns preceding the signal and N_{points} is the number of points in the waveform chosen to perform the computation.

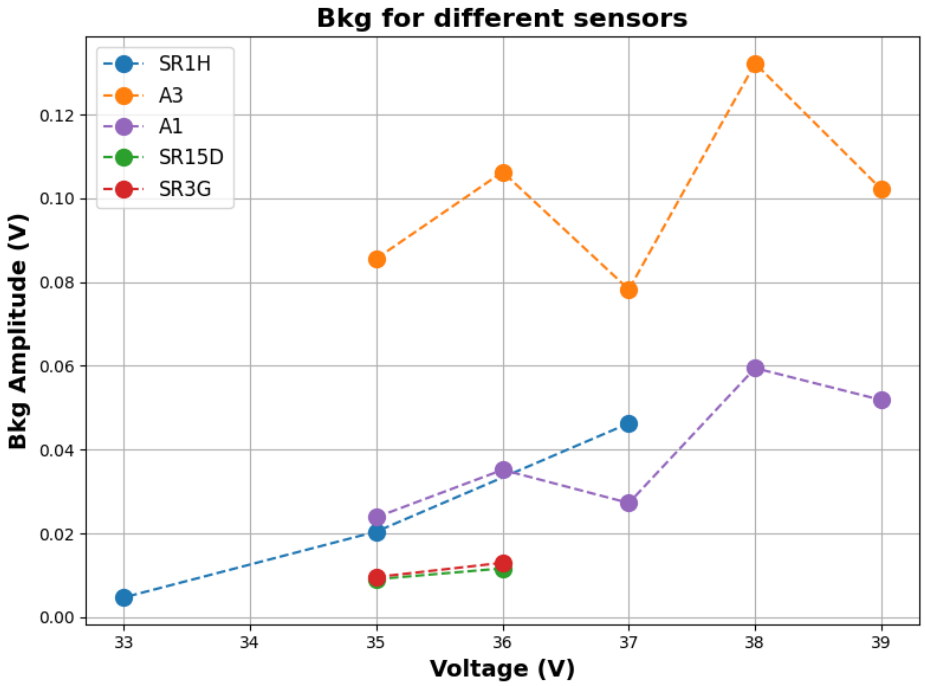

Figure 3.31: A comparison of the Root Mean Square (RMS) of the background distribution for different sensors as the applied voltage changes is shown in the figure for both the NUV-HD and NUV-HD-MT categories.

In figure 3.31 the root mean square (rms) of the background distribution, from which the baseline has been subtracted, is evaluated. As expected, it appears that sensor A3, of the NUV-HD-MT type, is the noisiest; in general, sensors with metal trench show higher signals but accompanied by more noise than standard NUV-HD. The SR1H sensor, despite having less resin than SR15D (1 mm vs. 15 mm), shows a higher rms value, comparable with A1; on the other hand, the performance of the sensor with 3 mm of SR3G resin reflects what is expected, i.e. it is slightly higher than that of SR15D. For standard NUV-HD sensors, the rms of the background seems to increase with voltage, because as the signal amplitude increases, so does the noise; this is not true for NUV-HD-MT, because we observe a minimum at 4 OV and the value at 6 OV is lower than that at 5 OV for both sensors in this category. This helps us in finding the correct range to work at: at 4 OV, the sensor's behaviour seems particularly stable.

[1] The DCR is a measure of the sensor noise in total darkness, whereas the background distribution is calculated in the region preceding a particle signal.

The fact that at 6 OV the rms no longer increases, but rather slightly decreases, simply indicates that the sensor's behaviour remains substantially stable at high OV.

3.3.3 Charged distribution

From the amplitude distribution, it is also possible to obtain the distribution of the charge deposited in the sensor, using equation 3.3.2, where j is a variable that identifies each point within the time window containing the signal, and N_{waves} indicates the number of points per waveform.

$$Q = \sum_{j=1}^{j} = N_{waves} \cdot A_j \cdot C_{SiPM} \tag{3.3.2}$$

The expected trend of the charge distribution is similar to that of the amplitude distribution but scaled by a factor equal to the sensor's capacitance.

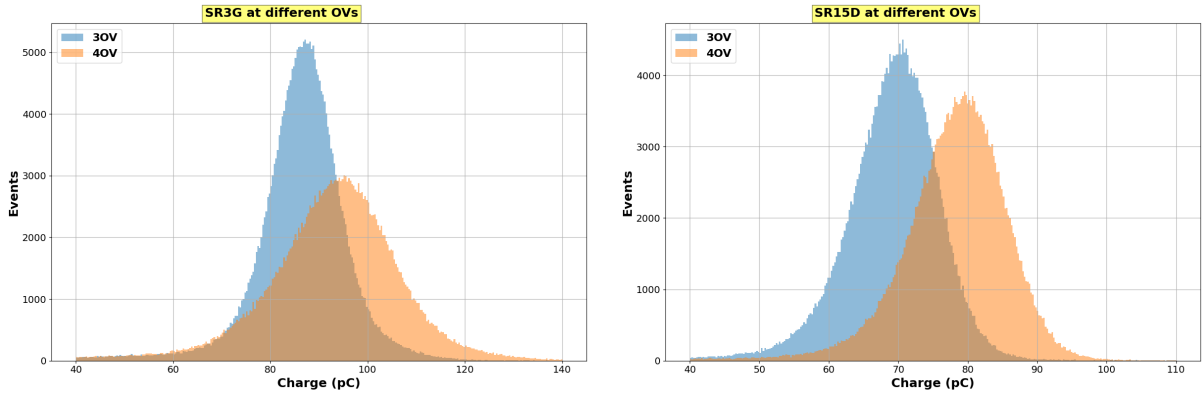

(a) (b)

Figure 3.32: The charge distribution is shown at different overvoltage for standard NUV-HD sensors with 3 mm resin (a) and with 1.5 mm resin (b).

It is also important to note that the distributions shown in figures 3.32a-3.32b and 3.33 are the result of the signal output from two amplification stages, consisting of two Lee39 amplifiers in series; the resulting amplification is about 40 dB, which corresponds to an amplitude gain factor as shown in equation 3.3.3, where A_V is the amplification in decibels. Figure 3.32a-3.32b shows the distributions for the sensor with 1.5 mm resin, SR15D, and 3 mm resin, SR3G; in both cases, the distribution broadens as the overvoltage increases, but the peaks corresponding to the SPADs are not visible. The charge distribution of SR3G sensor is shifted towards higher charge values, especially increasing the bias applied, since the charge particle crossing a thicker resin layer produces a larger signal. For this sensor, is also more evident the widening of the distribution with the overvoltage respect to SR15D. The charge distributions for the sensor without resin, WR-L, and the sensor with 1 mm of resin, SR1H, are shown in figure 3.33 at different overvoltages: even in this case, the distribution broadens as the OV increases, because the deposited charge increases. This effect is particularly noticeable for the SR1H sensor, where the distribution at 1 OV is much narrower and more peaked; this is reasonable since at 1 OV, we expect little charge to be deposited. Since the charge distribution reflects the amplitude distribution, the peaks corresponding to the SPADs are also visible here. The charge deposited in the sensor without WR-L resin is very little, as the charged particle encounters no medium in which to

emit Cherenkov photons and thus produce a visible signal. In fact, we see that compared with the sensor with SR1H resin, it reaches as much as 70 pC in deposited charge, whereas WR-L does not even exceed 10 pC.

$$A_V = \frac{V_{out}}{V_{in}} = 10^{\frac{A[dB]}{20}} \tag{3.3.3}$$

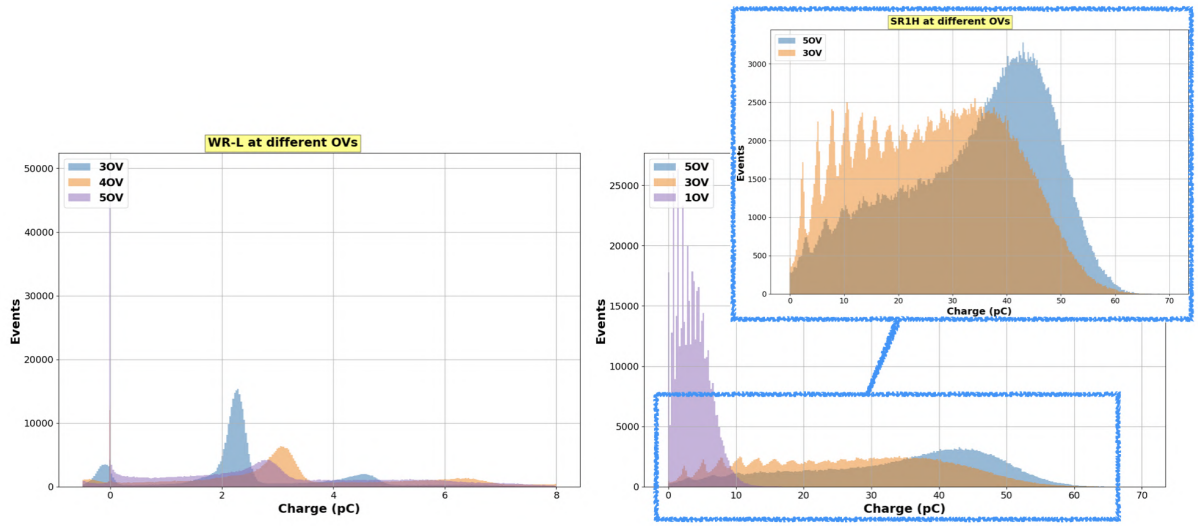

Figure 3.33: The charge distribution is shown at different overvoltage for standard NUV-HD sensors with no resin on the left and with 1 mm resin on the right.

3.3.4 Time resolution

The time resolution of SiPMs is obtained from the distribution of the difference between the time when the sensor's signal exceeds a fixed threshold and the time when the signal of the LGAD used as time reference reaches 50% of its amplitude. The time resolution is the width of the gaussian fit to this distribution, from which the time resolution of the LGAD is subtracted in quadrature; the latter is refered as reference, and it is 32 ps for the NUV-HD-MT SiPMs analyzed and 27.5 ps for the standard NUV-HD. Furthermore, when possible, it is also interesting to analyse how the resolution varies as the number of pixels affected increases. The time at which the signal cross the threshold is obtained according to equation3.2.2. It is important to note that the times populating the histogram are calculated on the rising edge of the signal when the corresponding amplitudes cross the fixed threshold value: for very sharp signals, one would expect to have few events below the threshold if the threshold is low, but many more events, and thus wider distributions, as the threshold increases. In the following section, the following situations are analysed:

1. **SiPM NUV-HD-MT at different overvoltages:** the time resolution values for this type of sensor are extracted at different overvoltages, as they are characterized by the ability to extend the operating range. However, despite the increased isolation that should provide more stable performance, they exhibit very large and noisy signals, deteriorating the time resolution at higher overvoltages. In general, it seems that 4 OV is a good working point. Finally, the signals are very large: the sensor is in saturation, and we are unable to distinguish the peaks

related to the hit SPADs, so we cannot calculate the time resolution as a function of the SPADs.

2. **SiPM NUV-HD with different resin thicknesses:** two standard NUV-HD sensors were analyzed at 3 OV and 4 OV, where the sensor's behavior is stable and not very noisy, with 1.5 mm and 3 mm of resin. In this case as well, the sensor with more resin has larger signals, but also a noisier behavior, making it more difficult to identify a trend in time resolution. However, the standard technology seems to have better timing performance compared to the more isolated one, which perhaps suffers from the slightly reduced fill factor.

3. **SiPM NUV-HD with and without resin comparison:** the samples without resin are not sensitive to the passage of charged particles and it is expected one SPAD fired; events with multiple hits are due to sporadic noise. However, the fact that particles passing through them do not produce photons results in cleaner and less noisy signals on the subsequent sensor, where the SPADs are visible: the time resolution can therefore be studied as a function of the hit SPADs for a sensor with 1 mm of resin.

3.3.4.1 SiPMs NUV-HD-MT

Figure 3.34 shows the time distribution for NUV-HD-MT SiPMs at 6 OV (a and b) and at 2 OV (c and d) for sensors with 1 and 3 mm resin at different fixed thresholds, respectively. At 2 OV we see that A1 (figure 3.34a) and A3 (figure 3.34b) have two contrasting behaviours: in the first case the number of events decreases as the threshold increases, while in the second case the trend is opposite. For A1, this is due to the fact that the distribution widens and therefore fewer events populate the peak; for A3, on the other hand, having wider (but also noisier) signals, the number of events increases with the threshold because the signals are very spiky: as the threshold increases, these events are included in the time distributions. The distributions at 6 OV (figures 3.34c for A1 and 3.34d for A3) have a similar trend to that of A1 at 2 OV: in general, as the threshold increases, points with large amplitudes are also included in the histograms, thus widening the distributions, which therefore lose events in the main peak. For A3, as the amplitudes are very large, we notice in figure 3.34d that even at low thresholds the distribution has few events, as the signals have a very steep slope and we find few points with low amplitudes. Moreover, as the voltage increases, we expect the resolutions to improve because the distributions become narrower: this is true for the A1 sensor, which is not excessively noisy; however, the A3 sensor at 6 OV has a particularly noisy distribution which is also very wide, thus worsening the resolution.

The values of the time resolutions as the thresholds vary are shown in figure 3.35, for sensor A1 in (a) and for sensor A3 (b).

For sensor A1 in figure 3.35a, the resolution improves as OV increases and worsens as threshold increases. The only exception is at 5 OV, where the resolution has high values, even over 100 ps; it remains fairly stable between 60 ps and 80 ps at 6 OV, although the lowest value of 50 ps is reached at 4 OV. Due to its very noisy behaviour, the trend is more complicated for sensor A3 in figure 3.35b: at high OV, the resolution improves as the threshold increases, because the signals are very high. At lower overvoltage, the resolution worsens as the threshold increases, probably because noise events also enter. In this case, the best values are reached at 2 OV, even though we do not go below 70 ps; however, at this voltage, the resolution deteriorates severely as the threshold increases, even reaching 140 ps. At high overvoltage in general,

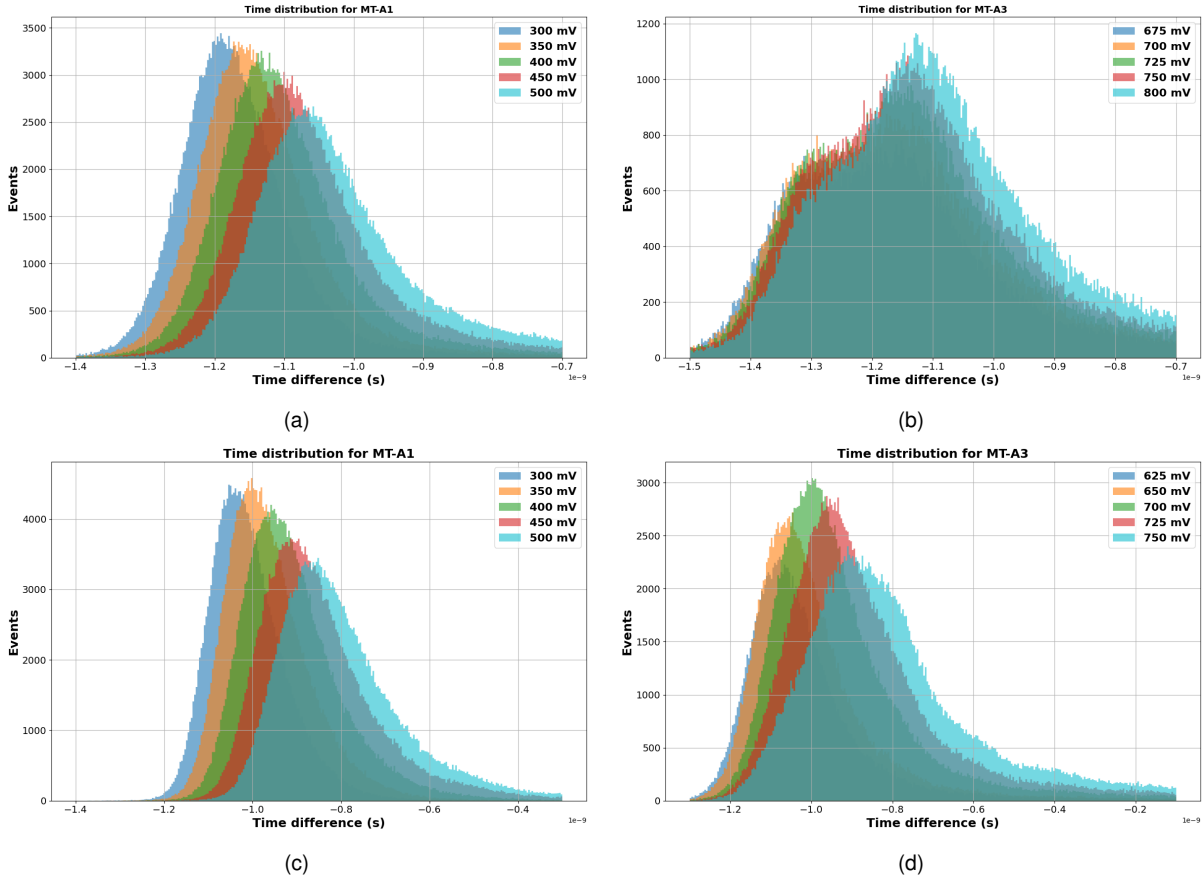

Figure 3.34: Time histograms as the fixed threshold changes at 6 OV (a and b for A1 and A3 sensors, respectively) and at 2 OV (c and d for A1 and A3 sensors, respectively) are shown in the figure.

behaviour remains more stable and values vary less with thresholds, although resolutions exceed 100 ps at both 5 and 6 OV. Uncertainties on resolutions, on the other hand, were calculated by analysing several datasets belonging to different test beams; for each dataset, the percentage error was calculated as given in equation 3.2.3.

The percentage error was averaged over different datasets (first at varying OV for the same sensor, then at varying sensor). By repeating the same procedure on different data sets, an error of 11% was assumed, as this value is the most recurrent as a result of the calculations explained above. Since similar calculations also returned a similar value for other sensor types (10% for LGADs), it was assumed to be a reasonable value.

The fits of the distributions are shown in figure 3.36 for the NUV-HD-MT sensors for A1 (left) and A3 (right); the fit is more problematic in the latter case due to the very noisy distribution.

3.3.4.2 Standard NUV-HD sensor: SR15D and SR3G

The time distributions for different fixed thresholds were also analysed in figure 3.37 for standard NUV-HD sensors with 3 mm of resin SR3G (a) and 1.5 m of resin SR15D (b). In contrast to the previous sensors, these show much less noisy behaviour with a very narrow distribution; this is due to the fact that the NUV-HD-MT SiPMs, due to the presence of the metal trench, can work over a wider range of voltages, resulting in wider signals. Standard NUV-HDs, on the other hand, have cleaner signals, even though the voltage they can observe is reduced.

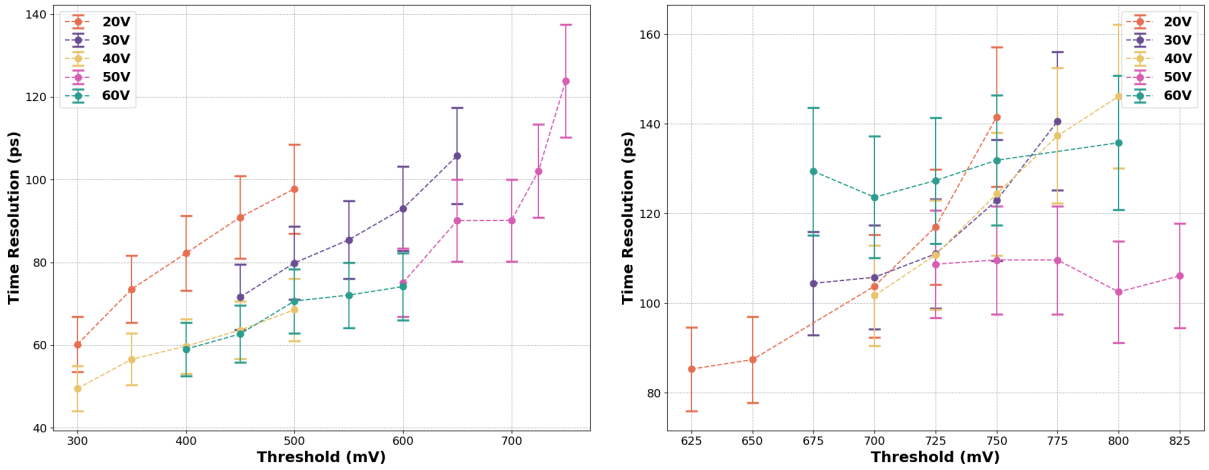

(a) (b)

Figure 3.35: The figure shows the trend of temporal resolution as the fixed threshold changes for sensor A1 (a) with 1 mm of resin and for sensor A3 with 3 mm (b) as the fixed threshold applied varies.

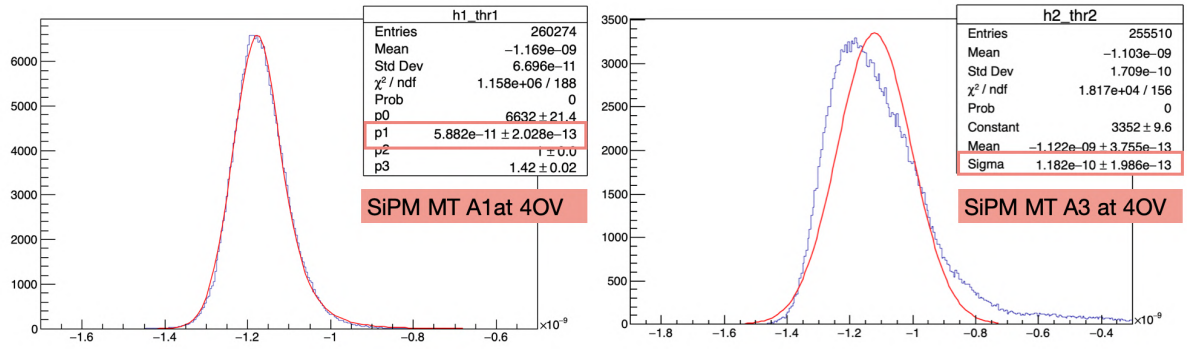

Figure 3.36: Figure shows the fit on the histograms of temporal resolution for NUV-HD-MT sensors with 1 mm resin (left) and with 3 mm resin (right) at 4 OV.

However, the time resolution seems to benefit from this behaviour, as is shown in figure 3.38 for several fixed thresholds: the thresholds are also lower than for NUV-HD-MT because of the smaller signals. From the figure 3.38a we observe that for the SR15D sensor the resolution increases as the threshold increases at both 3 OV and 4 OV because the number of events entering the distribution increases (the threshold is exceeded from below); however, at 4 OV, the value remains more stable, going from around 40 ps to 45 ps (the resolution exceeds 60 ps at 35 V). The trend is also similar for the SR3G sensor (3.38b) at 4 OV where the resolution reaches a maximum at 45 ps as the threshold increases, then decreases. At 3 OV, on the other hand, the trend is opposite, because the resolution reaches a minimum around 37 ps and then begins to increase again up t 40 ps: this is due to the shape of the signal, which probably has smaller amplitudes than at 4 OV. As is evident from figure 3.39, the fit on this type of distribution is also much simpler and seems to fit the data very well. Comparing with what has been observed before, it seems that the time resolutions reach their minimum value around 4 OV, where the noise does not degrade the distribution too much.

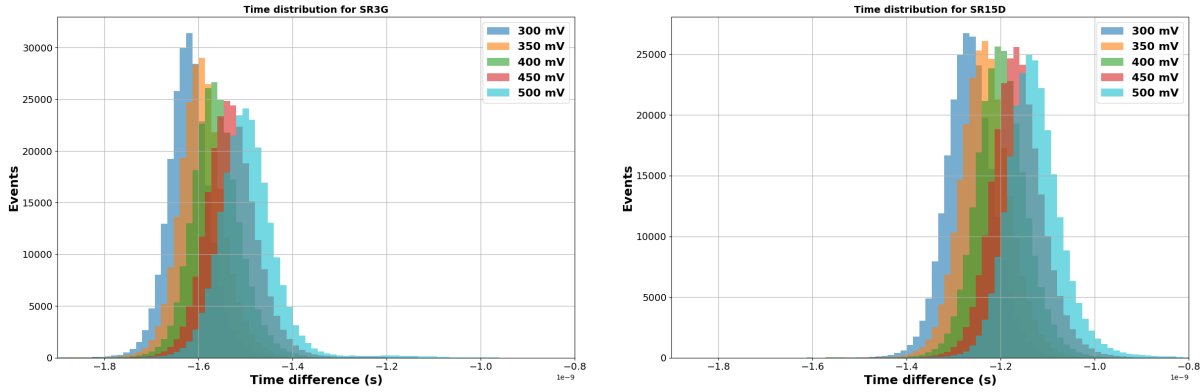

(a) (b)

Figure 3.37: Time distributions as the fixed threshold changes for SR3G, standard NUV-HD with 3 mm resin (a) and SR15D with 1.5 mm resin (b) sensors at 36 V, which correspond approximately to 4 OV.

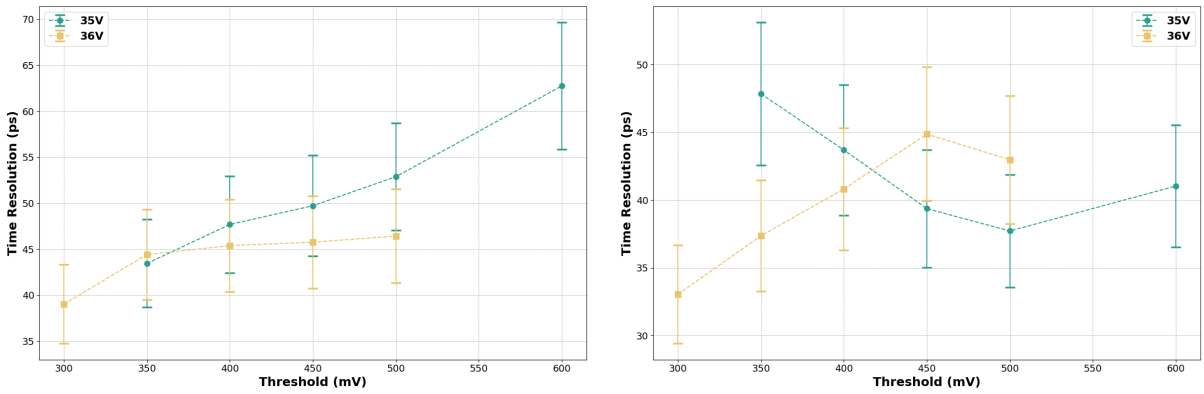

(a) (b)

Figure 3.38: Shown in the figure is the time resolution trend as the fixed threshold changes for standard NUV-HD SiPMs SR15D with 1.5 mm resin in (a) and for SR3G with 3 mm resin in (b) at 35V and 36 V (3 OV and 4 OV respectively).

3.3.4.3 Effect of the resin: standard NUV-HD SR1H and WR-L

Finally, the temporal resolution is analysed for the standard NUV-HD sensor SR1H compared with a without resin sensor, the WR-L; in this case, the SiPM was not fully saturated and SPADs were visible, so the resolution was calculated as the number of SPADs affected varied. It must be emphasised, however, that although SPAD-related peaks are visible in the amplitude distribution of SR1H, most events occur with many SPADs switched on, and it is still difficult to distinguish the first SPADs switched on.

Finally, the amplitude associated with a SPAD for SR1 sensors in general appears to be different from that associated with WR due to different characteristics within the sensor, although this aspect is still well worth investigating. The time distributions at 2 OV and at 4 OV for WR-L (a and b) are shown in the upper part of figure 3.40, while SR1H at 2 OV and at 4 OV are shown below (c and d). For both sensors, as the voltage increases, the number of activated SPADs increases, but for the sensor without resin (figures 3.40a and 3.40b), it is not possible to observe more than 3 fired pixels, as expected. For the sensor with resin (figure 3.40c and 3.40d), on the other hand, we can distinguish up to 8 pixels hit before the sensor goes into saturation, which corresponds to 8 peaks in the amplitude distribution. We also observe that as the voltage increases, the events for a higher number of SPADs increase, as seen in the peak at 7 SPADs in the figure 3.40d. How the timing resolution varies as a function of the number of

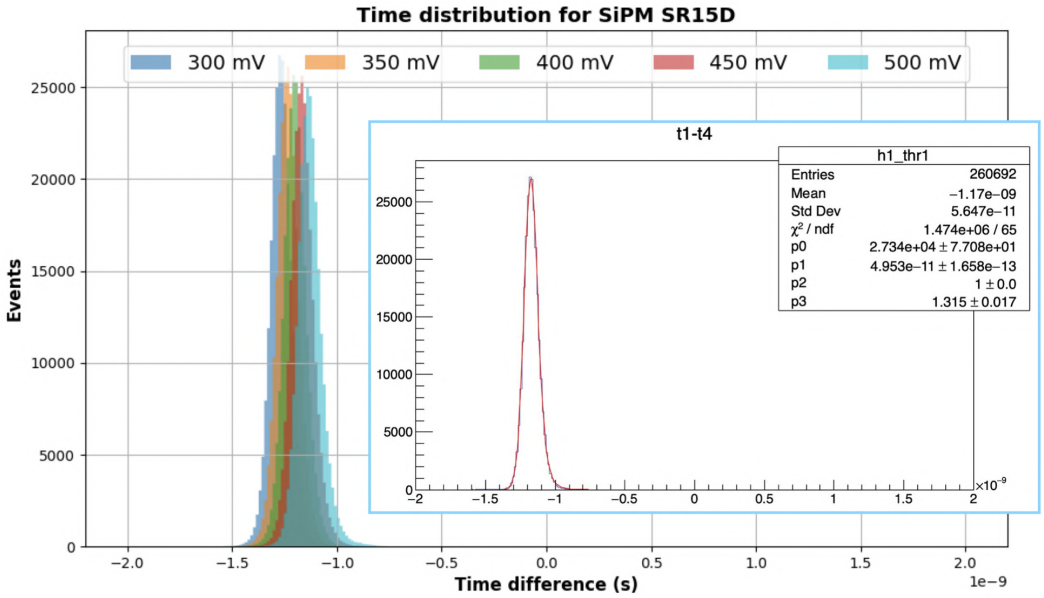

Figure 3.39: Shown in the figure is the fitted time distribution for standard NUV-HD SiPMs SR15D with 1.5 mm at 4 OV.

SPADs hit is shown in figure 3.41: for the SR1H sensor (3.41a) the resolution improves as the number of pixels hit increases, also because the associated number of events increases. The resolution gets better of a factor 6 at 9 SPADs fired, even if the reached value is not optimum (slightly below 100 ps). This is the opposite of what happens with a photon laser source: with charged particles, the Cherenkov cone activates many pixels and the number of events increases as the number of SPADs hit increases, because the signals are much greater; with photons, on the other hand, the beam is well collimated so it is rare to hit many pixels, so the timing resolution also deteriorates. With the sensor without resin, on the other hand (figure 3.41b the distinction between charged particles and photons does not exist, so not only do we have few SPADs hit but also fewer events as the number of SPADs increases, so the temporal resolution tends to get worse. It is difficult to detect a trend with only a few SPADs affected, also because the resolution values do not vary much in the range between 100 and 200 ps, as was already observed in the laboratory with the laser source.

3.3.4.4 The Constant Fraction Discrimination method for NUV-HD-MT sensors

The temporal distributions reported for SiPMs belonging to the NUV-HD-MT category were also analysed using the Constant Fraction Discrimination (CFD) method, in which the temporal resolution is evaluated when the signal exceeds a certain percentage of the signal; in particular, the temporal resolutions were analysed with 9 thresholds, starting from 10 % and reaching 90 % of the signal. Again, the time resolution is obtained as the standard deviation of the time distribution, which in turn is the result of the equation 3.3.4, where b is the percentage, j is a temporary variable indicating the binning of the waveform's points saved on the oscilloscope. The percentages from 10% to 90% are contained in the array $CFDTh[b]$ and $fact = CFDTh[b]/100;$; again the time is calculated within the rising edge when $amp_j < amp_{max} \cdot fact$, where amp_{max} is the maximum amplitude within a waveform.

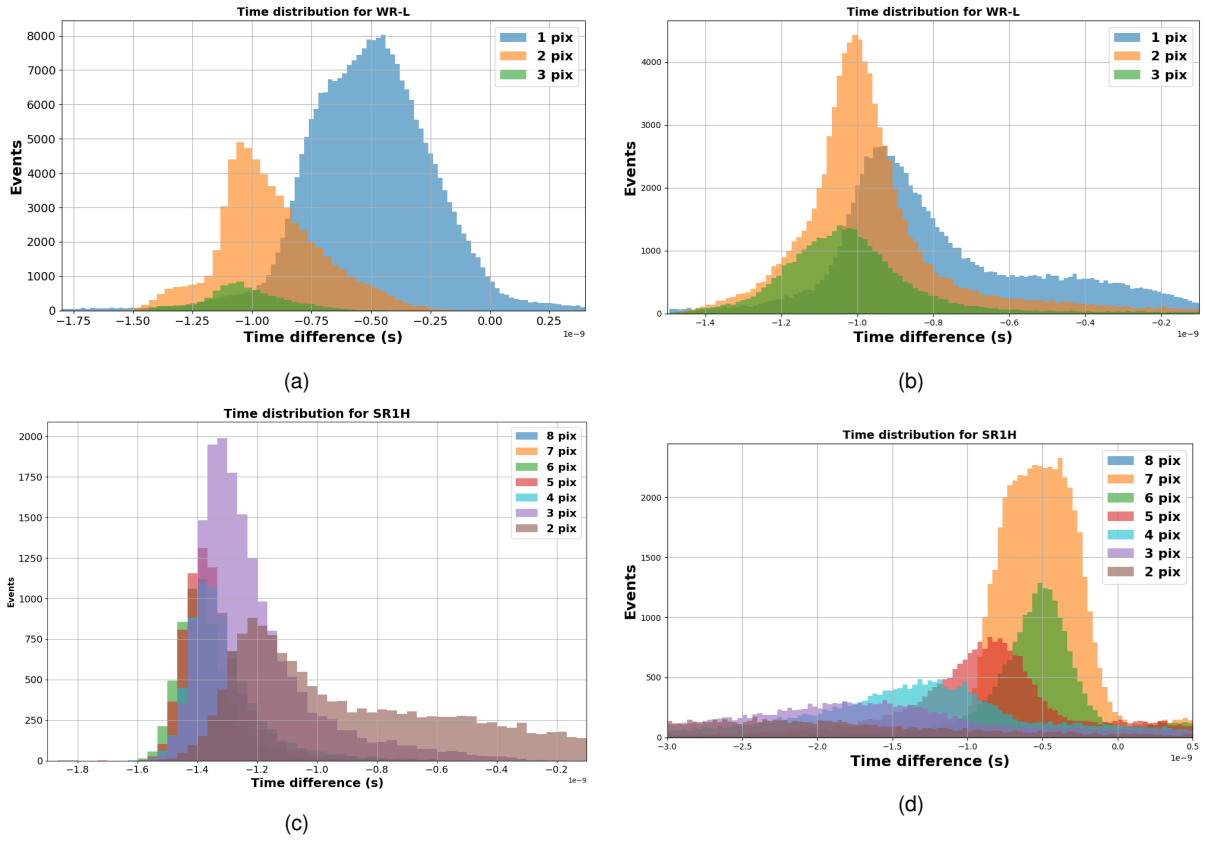

Figure 3.40: Shown are the fixed-threshold time distributions for the standard NUV-HD sensors without resin WR-L at 3 OV (a) and 5 OV (b) (with thresholds at 50 mV and 100 mV, respectively) and for the sensor with 1 mm SR1H resin at 3 OV (c) and 5 OV (d) (50 mV thresholds for both).

$$timeTh[b] = time_j + \frac{(time_{j+1} - time_j)}{(amp_{j+1} - amp_j)} \cdot (amp_{max} \cdot fact - amp_j) \tag{3.3.4}$$

The time distributions obtained are shown in figure 3.42 at 6 OV for the sensors A1 (3.42a) and A3 (3.42b) and at 2 OV (A1 in figure 3.42c and A3 in 3.42d, respectively). At low CFD percentages the distributions get broader since the jitter contribution is greater at the beginning and at the end of the signal, where the signal's shape is less steep. Furthermore, at high CFD, especially for the NUV-HD-MT sensors, the shape of hte distributions becomes less Gaussian, further degradating the time resolution. The measured values of time resolution obtained with the CFD analysis are reported in figure 3.43. The general trend that can be observed is that the resolution reaches a minimum for percentages between 40% and 60% for the sensor with 1 mm resin A1 (figure 3.43a). The minimum value observed is about 60 ps, and the trend does not seem to change a lot with increasing voltage; only in the case of 2 OV do we obtain an extremely high resolution value (130 ps) at 90% CFD, but in general the curves seem to be quite stable at all overvoltage. For the A3 sensor (figure 3.43b), on the other hand, at all overvoltages we observe a minimum in resolution at 80% of CFD. Here too, the minimum seems to be around 60 ps; we also note that all the curves have a fairly constant trend except for those referring to 5 OV and 3 OV: in the latter case, it is only at 30% CFD that the resolution starts to have reasonable values around 100 ps. In the former case, on the other hand, the temporal resolution approaches 100 ps only beyond 60% CFD, thus exhibiting behaviour that is not as in line as expected.

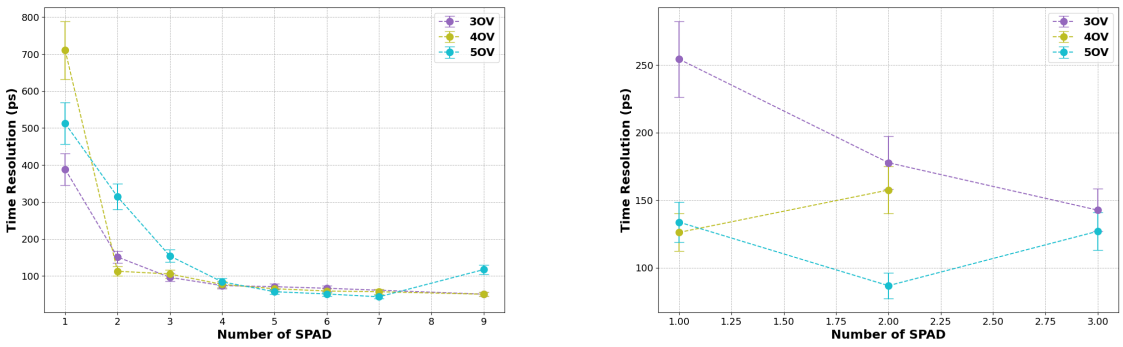

(a) (b)

Figure 3.41: Shown in the figure is the trend of temporal resolution as the affected SPADs change for standard NUV-HD without resin sensors with 1 mm of resin SR1H (a) and for the sensor without resin WR-L (b).

3.3.5 Charged particle beam at 1.5 GeV/c

The following paragraph presents a comparison in both amplitude and temporal resolution for the sensors without resin, WR-E, and those with 1 mm thick resin, SR1A; both are sensors from the NUV-HD standard category. The sensor's temporal resolution should not depend on the momentum of the incoming beam particles since it depends on the intrinsic characteristics of the sensor, such as gain and the electric field. In fact, at both 1.5 GeV/c and 10 GeV/c, the energy deposited by a Minimum Ionizing Particle (MIP) is similar because we are in the Fermi plateau, which is the region of the Bethe-Bloch curve where the energy deposition increases very slowly [64]. In contrast, the amplitudes depend on the energy of the beam because Cherenkov radiation is only emitted when the particle is travelling faster than light in the medium; we therefore expect the distribution of amplitudes at lower energies to be shifted towards lower values, as we are approaching the momentum threshold below which particles no longer emit photons and the number of fired SPADs decreases. Finally, by selecting the energy of the beam we modify the composition of the beam: at higher energy it is mainly composed of protons and pions (70/20%), while at lower energies it has a high positron content.

3.3.5.1 Amplitude distribution

Figure 3.44a shows the comparison between the signal amplitudes at 1.5 GeV/c and 10 GeV/c for the sensor without resin, WR-E; the distributions are comparable, as expected. The amplitude range is very limited because charged particles do not emit Cherenkov radiation due to the absence of the resin layer: only a few SPADs are triggered, due to sporadic noise events or photons emitted by electrons crossing the air between two planes. Since the signals have limited amplitudes, the peaks corresponding to the hit SPADs are recognisable.

For the sensor with resin, SR1A, the amplitude distributions are shown in figure 3.44b; only in the 1.5 GeV/c distribution has the peaks corresponding to some hit SPADs recognizable, although both distributions have most events at amplitude values near 1 V, with many SPADs hit. However, the slight difference in the distribution is easily explained: Cherenkov radiation is emitted when the particle's velocity exceeds that of light in the medium, so it depends on the particles momentum. However, the number of photons emitted does not depend on the energy of the photons themselves. So,

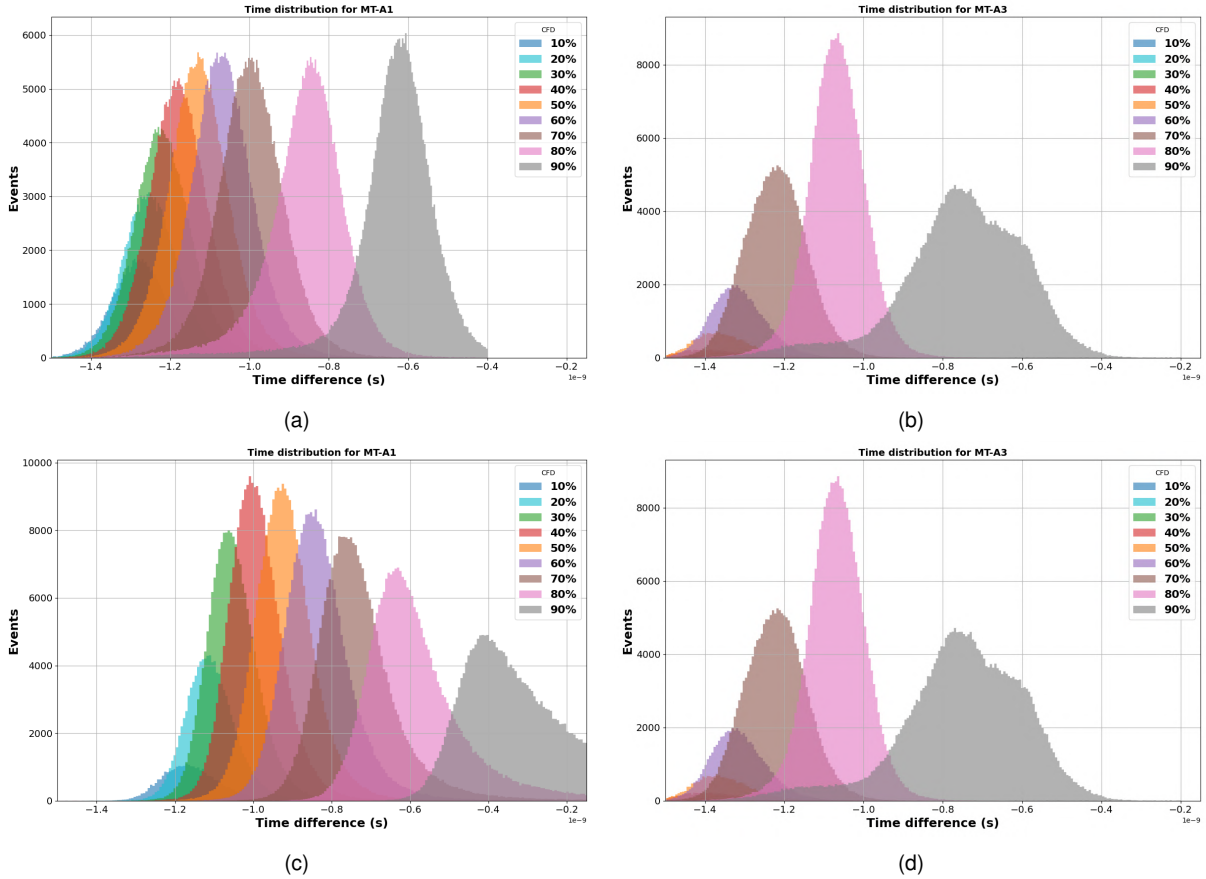

Figure 3.42: Time histograms at varying CFD percentage at 6 OV (a and b for A1 and A3 sensors, respectively) and at 2 OV (c and d for A1 and A3 sensors, respectively) are shown in the figure.

even though the amount of deposited charge does not change significantly, the number of photons produced increases with momentum, shifting the amplitude distribution to higher values. Finally, it is interesting to note that the two distributions are both peaked around the same value, around 550 mV: this is due to the fact that the number of photons emitted by an electron of 1.5 GeV/c in 1 mm of resin is the same as that emitted by protons and pions of 10 GeV/c.

3.3.5.2 Time Resolutions

The timing resolution of a silicon sensor depends on its distribution of arrival times, which in turn is calculated based on the time at which the signal crosses a certain threshold. For this reason, the temporal resolution does not depend on the energy, because the signal amplitude is determined by the sensor's internal characteristics, and the energy deposited by a charged particle does not change when varying the beam momentum from 1.5 to 10 GeV/c. The temporal resolutions obtained are shown in Figure 3.45a for the WR-E sensor, without a resin coating, and in figure 3.45b for the SR1A sensor, with 1 mm of resin, as a function of the fixed threshold. Although the values vary slightly with changes in beam energy, no significant discrepancies are observed either in the trend or the values reached; this is particularly true for SR1A, where the resolution worsens as the threshold increases: it passes from 60 ps to 100 ps at 10 GeV/c, but varies only of 10 ps at 1.5 GeV/c. For WR-E, however, the trend as a function of the threshold is less linear, but for both energies, we observe a minimum at 20 mV. Moreover, at 10 GeV/c, the lowest value achieved is 80 ps, but at 1.5 GeV/c the resolution also drops to 70 ps. A direct comparison of the time resolution provided

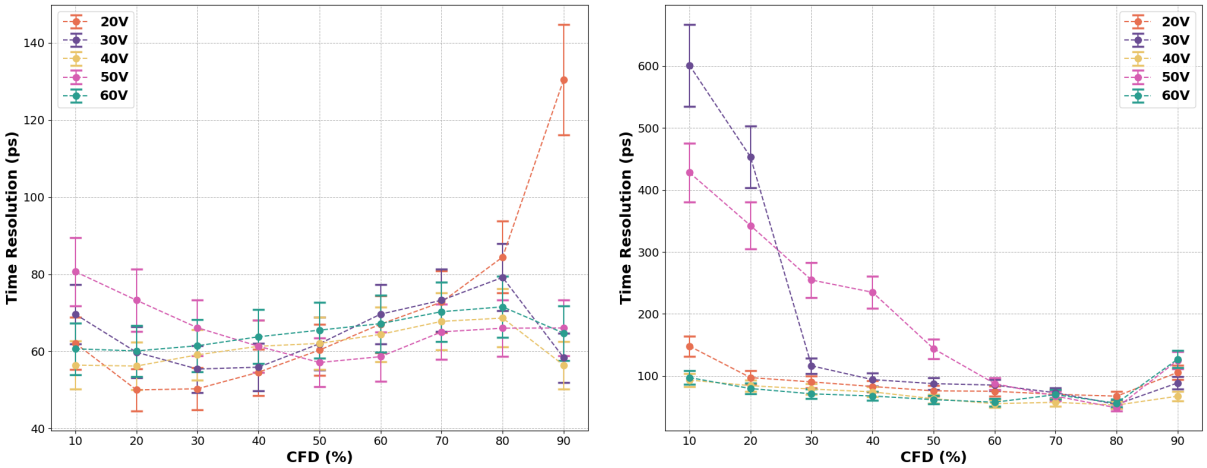

(a) (b)

Figure 3.43: Shown in the figure are the time resolutions at varying applied voltage for the NUV-HD-MT sensors as a function of the percentage of CFD applied, for the sensor with 1 mm of resin (a) and for the sensor with 3 mm of resin (b).

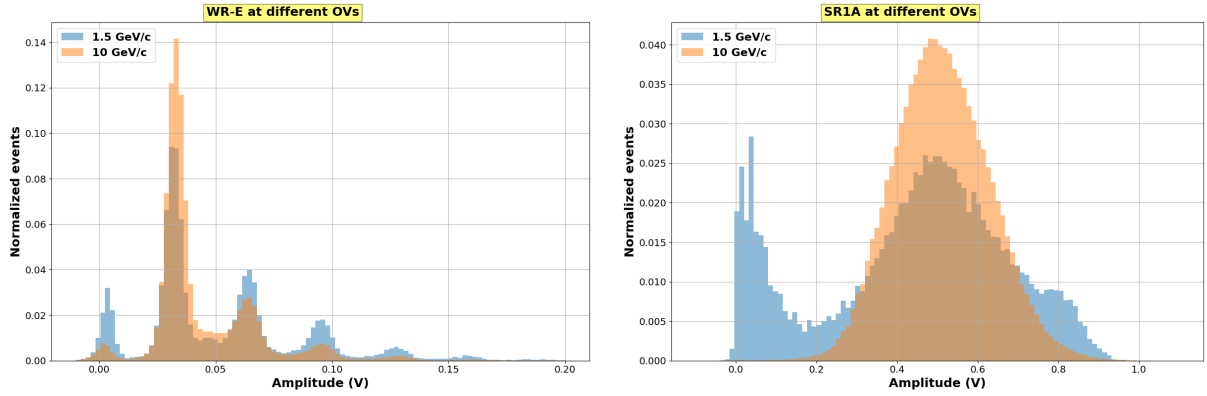

(a) (b)

Figure 3.44: Amplitude distribution for the sensor without resin WR-E for beam momentum of 1.5 GeV/c (a); the same plot for the sensor with 1 mm of resin SR1A (b). Different scale on the x-axis are used for the two plots.

by the two sensors is difficult because the thresholds chosen are very different, with those of SR1A being much higher than those of WR-E.

Once the threshold at which the resolution is minimal has been identified, we can study the trend of the resolution as a function of the number of SPADs hit (figure 3.46). This study is only possible with WR-E because the peaks corresponding to the SPADs are not recognizable for SR1A (or if they are, as in the case of 1.5 GeV/c, they are not well-defined enough to make cuts with good statistics). The trend at the two energies is similar: both have a minimum for 4 SPADs hit, with values dropping below 50 ps. It should be noted that for sensors without resin, the number of events decreases as the number of SPADs hit increases, as it is unlikely to have events involving many SPADs. The time resolution improved as the number of SPADs affected increased, as expected; events with SPADs affected greater than 5 were removed because the statistics were not sufficient and the observed trend was not reliable.

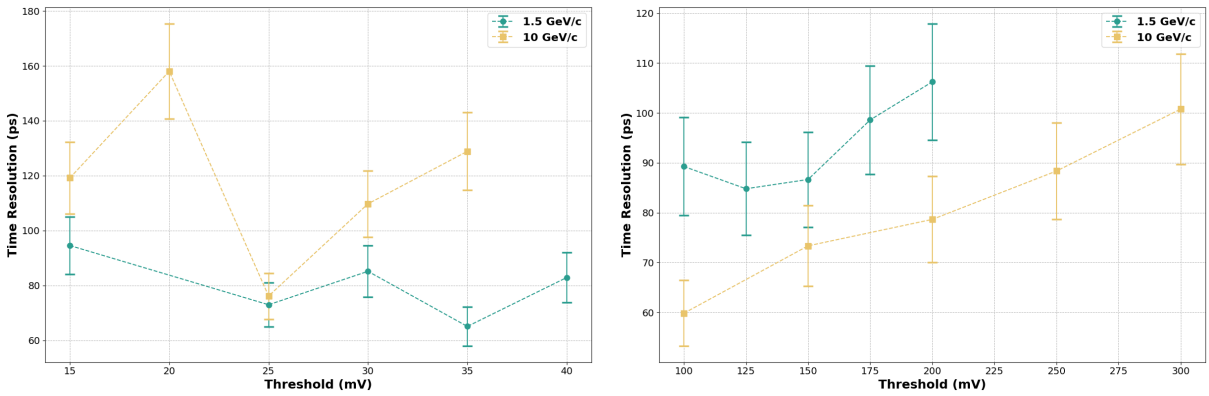

(a) (b)

Figure 3.45: Time resolution as the fixed threshold varies for the sensor without resin WR-E (a) and with 1 mm of resin SR1A (b).

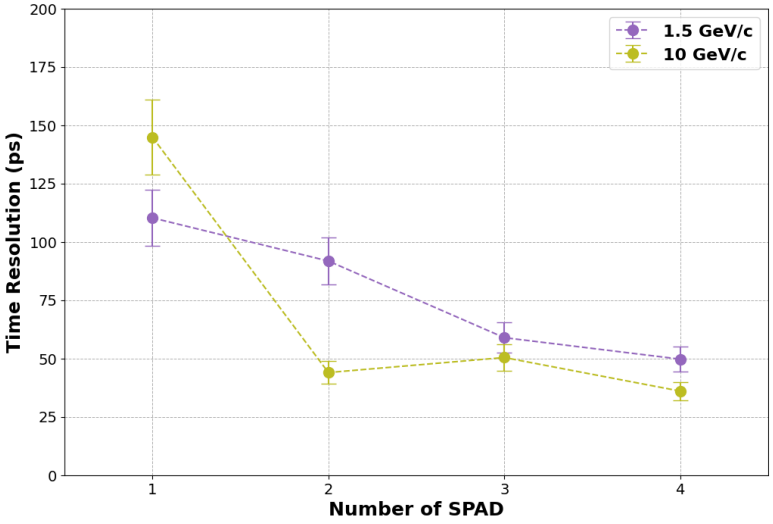

Figure 3.46: Time resolution as a function of the number of SPADs fired for the standard NUV-HD sensor without resin WR-E; the values at high number of SPADs are not reported since they are statistically not reliable.

3.4 Preliminary measurements with digital readout

The choice of which sensor to use in an experiment also requires the study of its integration into the complete readout chain. In the case of SiPMs, a system consisting of the Lidar Readout Chip (LiROC), a front-end ASIC developed by weeroc [65] providing signal discrimination and digitalisation, followed by the picoTDC which returns also the measure of the time the signal was above the threshold, is currently under study. The system consists of two Lirocs (A and B), each with 64 channels, and a picoTDC with a single channel resolution of 3 ps [65]; of the 64 channels, 8 can be read by the oscilloscope in analogue mode. The entire system is shown in figure 3.47, while a schematic of the entire readout chain is shown in figure C.1 in the appendix C.2. The readout of an event works with two triggers: the first one is the beam spill, while the second is the signal given by the first LGAD of the telescope. The LIROC first amplifies and shapes the signal, then it discriminize it. Following this, the picoTDC, which is a time to

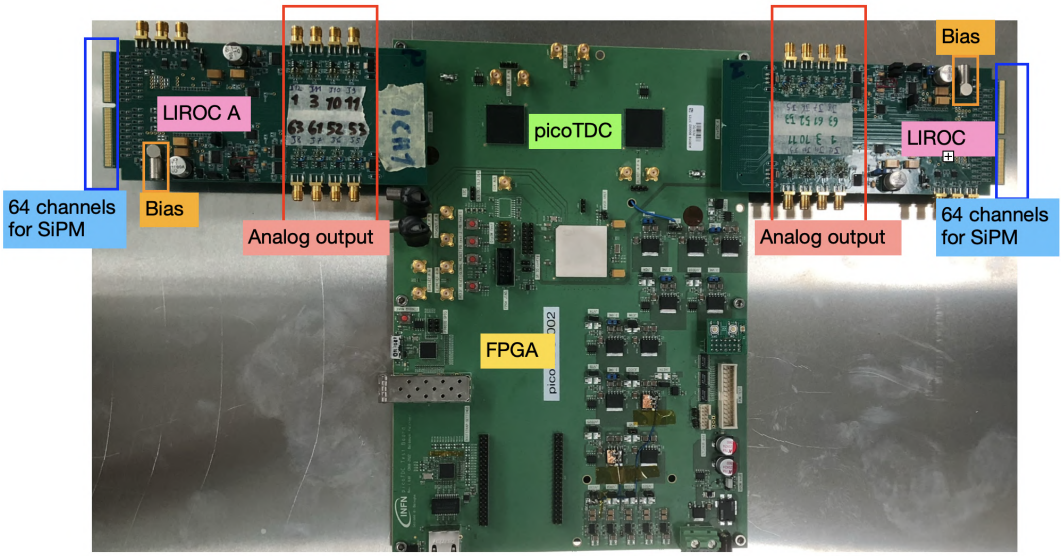

Figure 3.47: The circuit components of the LIROC are shown in the figure.

digital converter, gives the rising and falling time hits of the signal (more details in the appendix C.2).

3.4.1 Amplitude distribution

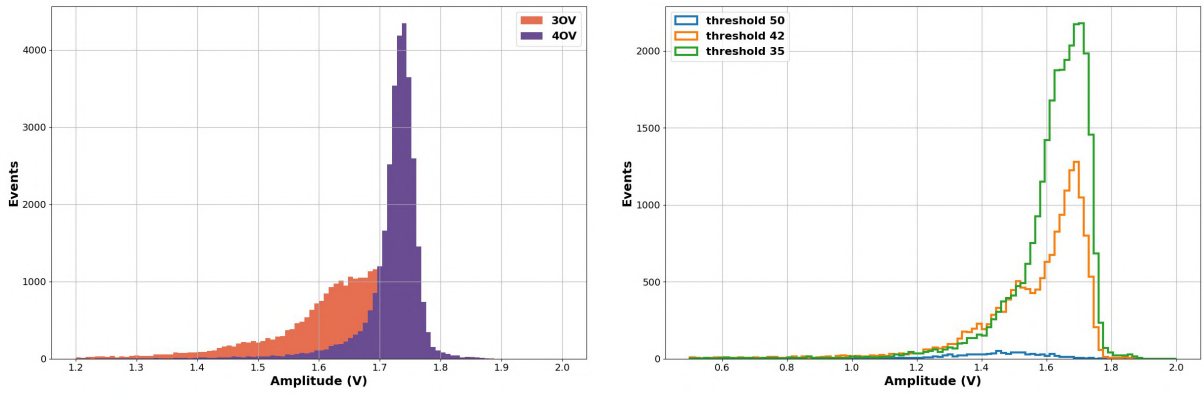

(a) (b)

Figure 3.48: (a) The amplitude distribution obtained with the analog readout after discrimination (output from LiROC) is shown in the figure for the standard NUV-HD sensor SR15B at 3 and 4 OV. (b) The change in distribution as the discrimination threshold changes at 3 OV, maximum laser intensity.

The distribution of amplitudes is studied by evaluating the response of the sensor to a laser source of photons by varying both the intensity of the beam and the discrimination threshold. The analogue acquisition of the amplitudes output by Liroc show us that it is possible to appreciate a distribution around about 1.7 V. As is shown in figure 3.48, the distribution narrows as the overvoltage increases. The distribution in the figure 3.48 is obtained with a maximum laser intensity and a threshold of 35 mV at 3 OV and 55 mV at 4 OV. The choice is usually made within a range starting from the point at which the signal can be clearly distinguished from noise (minimum threshold) until no more signals are observed (maximum threshold); the two thresholds mentioned above were the two minimum thresholds at that voltage. Figure 3.48 also shows the ampli-

tude distribution at 3 OV as the threshold changes: the number of events decreases as the discrimination threshold increases, as expected. The number of observed events decreases as the laser intensity decreases as shown in figure 3.49. As the tune decreases, the thresholds needed to observe the signals also decrease, as expected, and the distributions appear wider. The amplitude studies were done at fairly high values of laser intensity since at the lowest value very few events were observed. The choice of a suitable threshold is also problematic in this case because low thresholds are required to to have high efficiencies in real experimental applications, but this reduces the Signal-to-Noise ratio SNR.

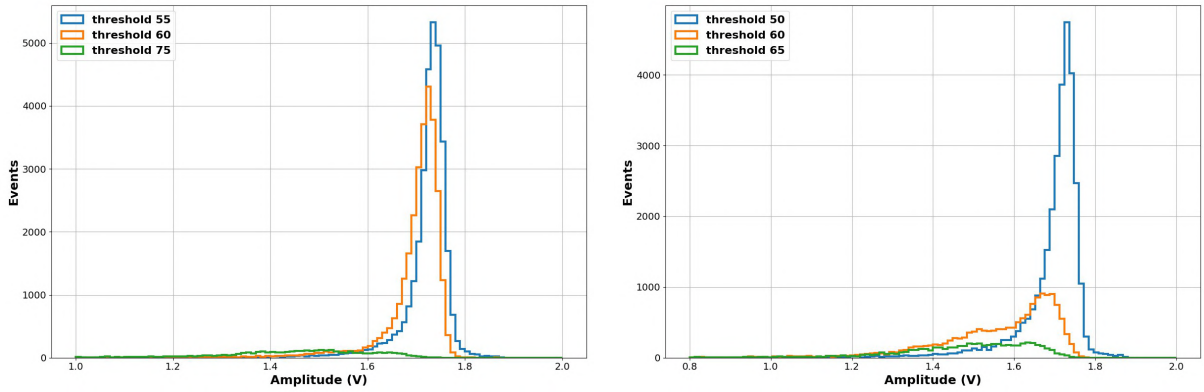

(a) (b)

Figure 3.49: A comparison of amplitude distributions at different thresholds for the standard NUV-HD sensor SR15B at the laser maximum intensity (a) and at an intermediate intensity (b) at an overvoltage of 4 OV is shown in the figure.

3.4.2 Time over Threshold

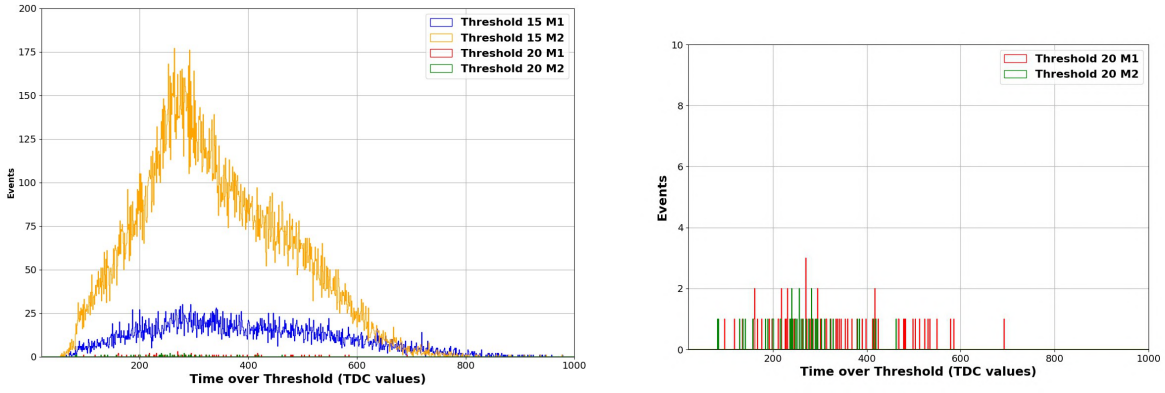

(a) (b)

Figure 3.50: (a) A measurement of Dark Count Rate (DCR) for two standard NUV-HD SiPM matrices with 1.5 mm resin (SR15-7 and SR15-10, M2 and M1 respectively) at varying discrimination threshold is shown in the figure. (b) Zoom on the ToT of DCR is reported for an increased threshold.

The width of the output signal of the picoTDC represents the time the signal remains above the thresholds, i.e. the Time over Threshold (ToT), which is computed as the dfference between the rising edge and the falling edge of two consecutive hits and it is a proxy for the analog signal amplitude. The preliminary analysis consists of a dark count measurement, where the sensor signal is acquired in total darkness and an

attempt is made to match the time over threshold for signals with only one pixel hit. This measurement was made on two standard NUV-HD arrays, SR15D-7 and SR15D-10, at two different thresholds, 15 and 20 mV at 2 OV. As shown in figure 3.50, the number of observed events decreases as the threshold increases; moreover, one of the two matrices seems to respond less than the other, because it is less noisy. A preliminary measure of the time above threshold is shown in figure 3.51 as the thresholds varies; obviously, as the threshold increases, the time spent above threshold decreases.

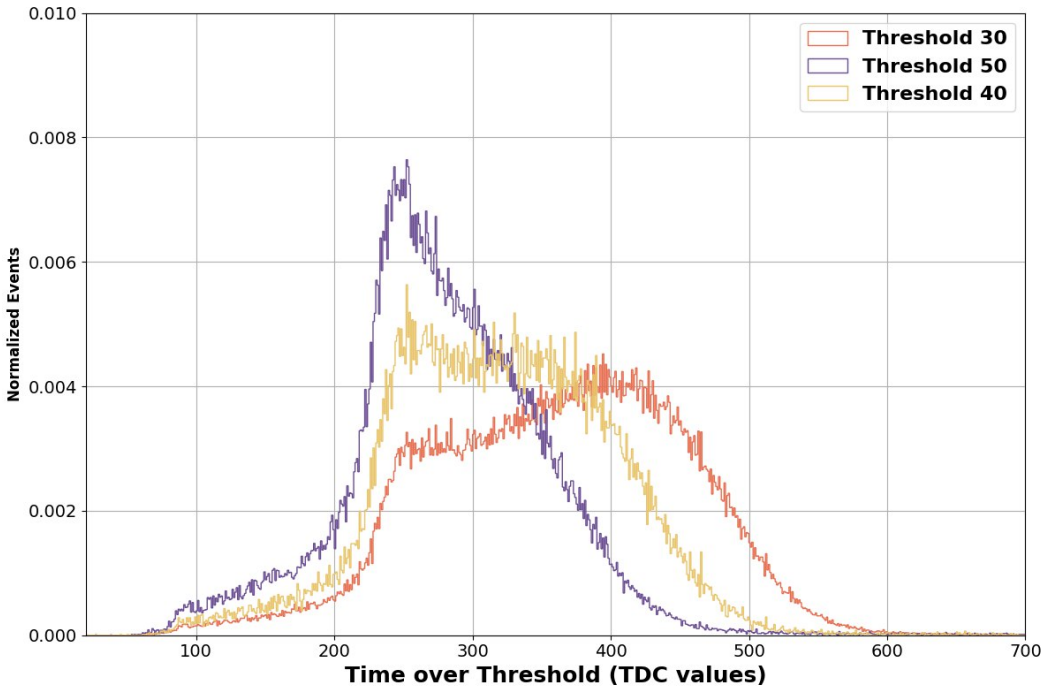

Figure 3.51: The time over threshold of the standard NUV-HD SiPM matrix with 1.5 mm resin M1 (SR15-10) at varying discrimination threshold is shown in the figure.

Conclusions

This thesis work focuses on the characterization of specific silicon sensors, the Silicon PhotoMultipliers (SiPMs), for the outer time-of-flight layer of the future ALICE 3 experiment. These sensors are traditionally used as photodetectors, as they are sensitive even to single photons; however, it has recently been demonstrated that they can also be used for direct charged particle detection, thanks to the emission of Cherenkov radiation in the protective resin layer placed on the sensor. The characterization of these sensors is thus based on measurements using both photons and charged particle beams at various energies. The analyzed samples belong to two categories of sensors manufactured by FBK: Near UV High Density SiPMs (NUV-HD standard) and NUV-HD-MT with metallic trenches between the SPADs.

The preliminary analysis is based on measurements of current and capacitance as a function of the bias applied and of the Dark Count Rate (DCR), which consists of measuring in total darkness how often the sensor emits a signal. These measurements allows for a comparison of behavior before and after irradiation. From the current analysis the of the breakdown voltage V_{BD}: for both the sensors' technologies, the value is around (32.5 $\pm$0.1) V. However, irradiated sensors seem to reach much higher current values compared to non-irradiated ones. From the CV curves, it was observed that irradiation modifies the sensors doping profile, decreasing the concentration, particularly in the surface region of the gain layer. From the measurement of the DCR, finally, we observe a typical rate of 1 MHz/mm^2 for never irradiated sensors, which increases of a factor of 10 irradiation of 10^9 1 MeV/n$_{eq}$, but we expect a more evident effect as the amount of radiation increases. Although the NUV-HD-MT sensors were designed to improve the isolation between pixels in order to strongly suppress optical crosstalk, in the tests carried out they did not demonstrate to perform better than standard SiPMs, with a DCR for non-irradiated sensors hovering around 1 MHz/mm^2. The value observed for irradiated sensors is around 5 MHz/mm^2, but the amount of irradiation is estimated to be smaller respect to standard NUV-HD.

The resolution measurements with the laser source aimed to extrapolate the SPTR (Single Photon Time Resolution): for this reason, both a filter and a diffuser were used to limit the number of photons hitting the sensor and also to increase the statistics when fewer SPADs were firing. The obtained resolution values are quite high, spacing from 100 ps to 200 ps, although this is compatible with expectations from this type of measurement. The best value obtained for temporal resolution is 110 ps for the NUV-HD-MT sensor without resin, where we also observed the lowest number of SPADs affected, i.e. 2; for the NUV-HD sensor with an epoxy resin cover we also achieve good values between 130 ps and 110 ps. The use of the filter and diffuser degrades the obtained resolution value: the diffuser, in particular, expands the laser spot by an angle of 45°, while the filter absorbs photons, likely introducing scattering phenomena that deviate their trajectory. This introduces noise events that involve multiple SPADs and degrade the measurement.

The temporal resolution measured with charged particle beams, however, can reach

values below 50 ps: in this case, thanks to the production of Cherenkov photons, many more SPADs are activated, and the resolution seems to improve precisely with the number of SPADs hit. In general, it is not always possible to study the trend of resolution as a function of the number of SPADs hit because sometimes the sensor saturates, and we cannot distinguish the peaks related to single SPADs in the amplitude distribution. When the sensor was saturated, the temporal resolution was studied as a function of a fixed threshold. The best value of time resolution was achieved by NUV-HD sensors with 3 mm of resin (about 35 ps), while for NUV-HD-MT sensors the values found were worse, between 50 and 120 ps. The thresholds chosen correspond to the amplitude of 5-10 SPADs hit and generally, the results are better at lower thresholds. By varying the beam energy, moving from momenta of 10 GeV/c to 1.5 GeV/c, the amplitude distribution changes because at lower momenta we approach the Cherenkov radiation emission threshold, but the resolution does not change, remaining independent of energy.

Finally, these sensors were also tested with a full digital readout chain, consisting of a Lidar ReadOut Chip (LiROC) front-end ASIC, which discriminates signals and sends them to the picoTDC for digitization and precise time measurements. The amplitudes were studied through the LiROC analog outputs, to observe how the number of acquired events varies with the threshold: as expected, events decrease as the threshold increases. Lastly, the Time over Threshold (ToT) information provided by the picoTDC was extracted using beam measurements, again as a function of the threshold, to assess the reasonableness of the measurements taken with this full-digital readout: as expected, as the threshold increases, the ToT decreases.

Appendix A

More on ALICE 3

A.1 Electromagnetic calorimeter

The electromagnetic calorimeter (Ecal) is designed to cover the rapidity range of $-1.6 < \eta < 4$, i.e. the entire central region of the barrel plus a forward region. Most of the rapidity range will be covered by a sampling calorimeter, while a part of the central barrel will be covered by existing $PbWO_4$ crystals for the measurement of χ_C and soft direct photons. The resolution depends on the energy of the photons according to the parameterisation:

$$\frac{\sigma_E}{E} = \frac{a}{E} \bigoplus \frac{b}{\sqrt{E}} \bigoplus c \tag{A.1.1}$$

at low energies, the noise term $\frac{a}{E}$ and the stochastic term $\frac{b}{\sqrt{E}}$ dominate; the latter comes directly into play for a number of observables, such as the direct production of photons at low p_T, the measurement of radiation decays the measurement of radioactive decays of strange hyperons and quarkonia states that require to detect soft photons in the range $\approx 10\ Mev - 1\ GeV$ which in turn requires a stochastic term $b \approx 0.02 GeV^{1/2}$ and a cell size of $\approx 2cm\ x\ 2cm$ (see picture A.1).

The central barrel ECal is placed between the RICH detector and the magnet cryostat and it has an inner and outer radius of $1.15\ m$ and $1.45\ m$, respectively; since it is 7 m long, it is possible to cover the range of pseudorapidity $|\eta| < 1.6$. The endcap is composed of a disk with an inner radius of $0.16\ m$ and an outer one of $1.8\ m$. It is located downstream of the forward RICH at $z_{ECal} = 4.35\ m$ and covers the pseudorapidity interval $1.6 < \eta < 4$. The sector providing the precision energy measurement provides coverage of $\Delta\phi = 2\pi$ for azimuth angle, and $|\eta| < 0.33$ for pseudorapidity, corresponding to $|z| < 0.64\ m$ in length.

To discuss the implementation in more detail from a technical point of view, the sampling barrel calorimeter consists, in the simplest configuration, of a stack of alternating layers of lead and plastic scintillator $1.44\ mm$ and $1.76\ mm$ thick, respectively. The length ($l = 246\ mm$) is given by a stack of 76 layers providing 20 radiation lengths χ_0 and a stochastic term of $b = 0.11\ GeV^{1/2}$; 30 000 cells with a cross-sectional area of $30\ x\ 30\ mm^2$ and a tapered shape are required to obtain a projective geometry. For the endcap, on the other hand, there are 95 layers of $1.44\ mm$ lead sheet and $1.76\ mm$ scintillator for a total of $25\ \chi_0$, a thickness of $304\ mm$ and a stochastic term $b = 0.11\ GeV^{1/2}$; the total number of cells is 6000, with a cross-sectional dimension of $40\ x\ 40\ mm^2$. The high-resolution segment consists of lead tungstate $PbWO_4$ crystals with a cross section of $22\ x\ 22\ mm^2$ and a length $l = 180\ mm$, resulting in 20 χ_0. The expected number of cells for this segment will be ≈ 20000, organised in a cylindrical array of 320 cells in the azimuth direction and 62 cells in the longitudinal direction.

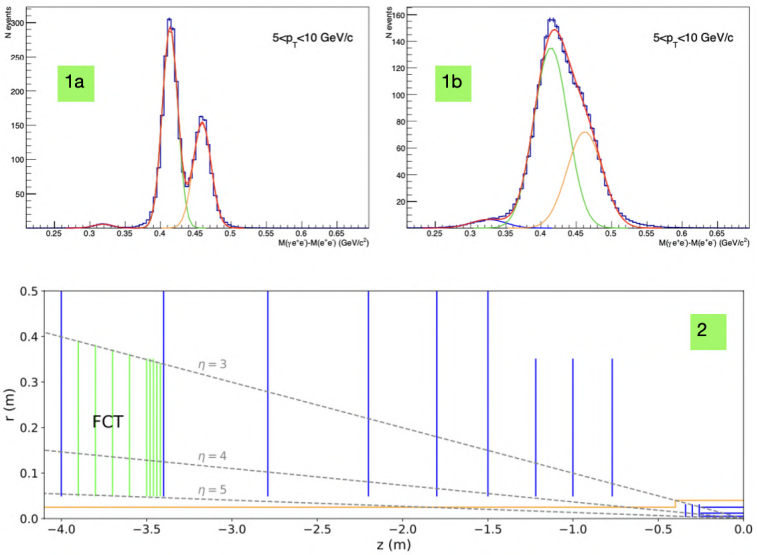

Figure A.1: The picture shows the invariant mass difference spectra of decay $\chi_{cJ} \rightarrow J/\Psi\gamma$ assuming different stochastic term: $b = 0.02\ GeV^{1/2}$ (1a) and $b = 0.05\ GeV^{1/2}$ (1b). In the second panel, the layout of the Forward Conversion tracker (FCT) is shown; the silicon disk are represented in blue.

A.2 Muon identification

The muon identifier is mainly used to reconstruct quarkonia states (in particular charmonia) down to $p_T = 0$ in the muon channel; the muon identifier therefore acts as a muon tagger for the reconstructed particles in the tracker. It is located outside the magnetic field and consists of chambers that track charged particles passing through the $1\ kt$ hadron absorber. The good efficiency in reconstructing charmonia states up to $p_T = 0$ in a rather wide rate range is based on the ability to reconstruct muons down to $p_T \approx 1.5\ GeV/c$ at $\eta \approx 0$; from simulations it appears that an absorber thickness of 70 cm at $\eta = 0$ and a good granularity of $\Delta\phi\ \Delta\eta = 0.02\ x\ 0.02$ are sufficient to reconstruct muons efficiently. The choice to use resistive plate chambers (RPC) for the muon system was made possible by the moderate charged particle rate $3\ Hz/cm^2$ and the pad size of $50 - 60\ mm$. However, it is considered to implement scintillator rods equipped with wavelength-shifting fibres; it is planned to use two layers of crossed scintillator rods ($5\ cm$ wide) with a spacing of $20\ cm$.

Photons with transverse momentum up to $p_T \approx 2\ MeV/c$ are measured by the Forward Conversion Tracker (FCT), as they can only be accessed by exploiting the Lorentz thrust in the forward direction, which allows photon energies $E_\gamma \approx 50\ MeV$ at $\eta = 4$. The photons are measured by exploiting their conversion into e+/e- pairs, which requires reconstructing electron moments down to a few MeV/c; a magnetic field perpendicular to the forward direction is exploited to achieve good resolution. The FCT performance study was done at position $z \approx 3.4\ m$ with a dipole field component $B_y \approx 0.3\ T$. In order to measure electrons of a few MeV (to which, in a magnetic field, correspond curvature radii of about 10 cm), an array of tracking layers (silicon disks) with a layer spacing of about 2 cm is used; in reality, other disks with a greater spacing are also provided to ensure good resolution for electrons with a higher momentum. Hence, 9 silicon disks are planned installed around the beam pipe in the direction of travel to cover the pseudorapidity range $3 < \eta < 5$ (figure A.1). Furthermore, the measurement of low p_T photons is not limited by statistics, so the silicon disc of the ALICE 3 tracker directly in front of the FCT can act as an active photon converter, also providing

tracking information at the conversion point. This eliminates the need for a dedicated converter, which would degrade the energy and resolution of the pointing due to multiple scattering and energy loss, although it would increase the conversion probability and could be considered for the study of rare channels. As far as implementation is concerned, the basic solution is to use the same sensors in the silicon discs as are used in the tracker, in order to achieve very thin layers and thus minimise the material and impact of multiple scattering. The area to be instrumented is $3.6\ m^2$, and silicon sensors are therefore the most likely solution for the FCT tracking areas.

Technological challenges focus on optimising the design of the beam tube and vertex detector to avoid shallow crossing angles; in order to avoid excessive bremsstrahlung, it is crucial to limit the amount of material in front of the FCT to less than $10\%\ \chi_0$. Selecting interactions at a large distance from the nominal interaction point could reduce the obstruction of the FCT by the vertex detector: for this purpose only collisions in the tail of the z-vertex Gaussian are analysed. For a collision at z=0 only particles with a pseudorapidity greater than $\eta = 5$ do not pass through the detector's vertex containment vessel; however, in order to reduce the available statistics by about a factor of 50 the FCT analysis is limited to events with a z-vertex displaced by more than 10 cm in the direction of the FCT. For these events, in fact, the particles coming from the primary vertex do not cross the containment vessel for pseudorapidity values greater than $\eta = arcsinhrz = 4.6$, where $r = 0.5\ cm$ is the radial distance of the containment vessel from the beam axis and $z = 25\ cm$ is the distance of the edge of the containment vessel from the displaced vertex. As far as bremsstrahlung is concerned, it can also be removed at the analysis level by imposing the absence of an electron track in the vicinity of the reconstructed photon. The creation of a large tracking area with extremely small material thicknesses requires careful study, particularly to achieve flat and stable geometries. Perhaps the latter could be increased by deviating precisely from flat geometry. Another interesting aspect is that the geometry currently being considered must cover an area larger than the size of individual wafers and therefore requires interconnection between sensors.

A.3 Magnets and infrastructure

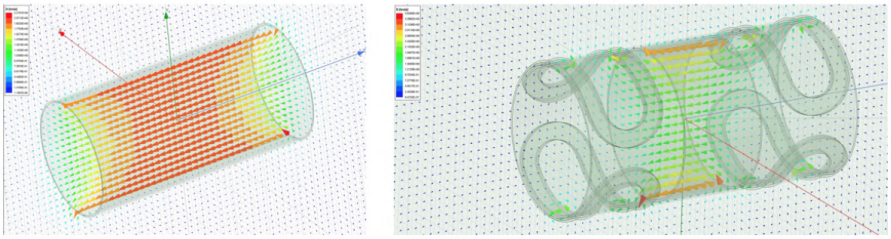

Figure A.2: In the picture are displayed two different configuration for the magnet system: to the left, the solenoid; to the right, the solenoid plus dipoles.

In figure A.2 are shown two different design for the superconducting magnet; the simplest configuration corresponds to a solenoidal coil over the full length of 7.5 m with additional windings at the coil end, resulting in a current density higher of 50%. The second configuration is made by a central solenoidal of 2 m length with a dipole magnet on both sides; the presence of dipole meganets improves the momentum spectroscopy in the rapidity range $2 < \eta < 4$. The solenoid magnet and dipoles have the same radius,

thus facilitating installation and maintenance without having to move part of the magnet system. Both magnets provide a solenoid filed up to $2\ T$ and so a field integral of up to $2\ T\ m$ at low values of η; however, increasing the values of η, the dipoles field integral reaches $1\ T\, m$, with a peak for the field of $\approx 0.5\ T$. To make a comparison, for muons of $p_T = 1\ GeV/c$, which is the multiple scattering limit, the first configurations provides a momentum resolutions of $0.6 - 1\%$ up to $\eta = 2$ but increases to 5% at $\eta = 4$; the second one, on the other hand, gives a momentum resolution of 1% at $\eta = 4$ with a small degradation the region between the solenoid and dipole field, for $1.2 < \eta < 2.2$.

A.4 Initial state

From the initial states, multiplicity can be derived, defined as the sum of the number of charged hadrons in a wide momentum range. It is connected to the impact parameter b which cannot be derived directly: multiplicity is large when b is small, that is, in central collisions where the number of N_{part} participants grows and consequently so does the number of particles produced. Thus, multiplicity is also an indication of the centrality of the collision, which is extremely useful since many properties of the system, as the energy densities and the lifetimes, depends on it. The multiplicity reveals also information about the entropy: if the system evolves without viscous effect, entropy is conserved; on the contrary, entropy is created during the evolution and the multiplicity provides an upper limit for the entropy of the initial states. Ultra peripheral collisions (UPCs) are a good tool to investigate initial states: typical the value of b is large, grater than the nuclear diameter. In this kind of collisions nuclei are separated such that short-range strong interactions are highly suppressed (and QGP cannot be created) so only photons-mediated interactions are possible. Measuring the differential cross sections of of light and heavy vector mesons as the ρ_0 and the J/Ψ the momentum distribution of partons inside the nucleon can be derived (the PDFs).

A.5 Hadronic phase

The hadronic phase of heavy-ion collision is analysed via several insights on:

- Measuring know hadron spectra and ν_n at intermediate p_T are sensible to the coalescence process in the hadronisation of quarks, competing with the fragmentation processes. In this p_T range the coalescence enhances the baryon production and increases ν_n more than for mesons.

- The chemical freeze-out temperature T_{chem} can be investigated by the measures of the total yields of specific particles by the integration of the equation 1.2.1, in case of particle which do not decay strongly or electromagnetically. On the opposite, strongly decay resonances can provide information about the duration of the hadronic phase: their decay products undergo elastic scattering which causes an emptying in the resonance yields, since the kinematic of the decaying products is so altered that reconstruction becomes too challenging. To compensate, hadron-hadron interactions in this phase can give rise to regeneration processes for resonances.

- Final state hadron-hadron interaction is also studied via the femtoscopic correla-

tion function, which is derived experimentally as:

$$C(k^*) = \frac{N_{pairs}(same\ event)}{N_{pairs}(background)} \tag{A.5.1}$$

where k^* is the invariant momentum difference between pairs; the numerator refers to pairs produced in the same collision, while the denominator is obtained by background hypothesis of not-correlated pairs and it is such that $C(k^*) = 1$ in absence of event correlations. At low p_T, femtoscopic correlation is the result of quantum correlation sensitive to the size of the system at the freeze-out, or to final state hadron-hadron interaction.

- Finally, from the slope of hadron spectra the kinetic freeze-out temperature T_{kin} is derived.

A.6 Study on bottonium states: suppression and small regeneration effects

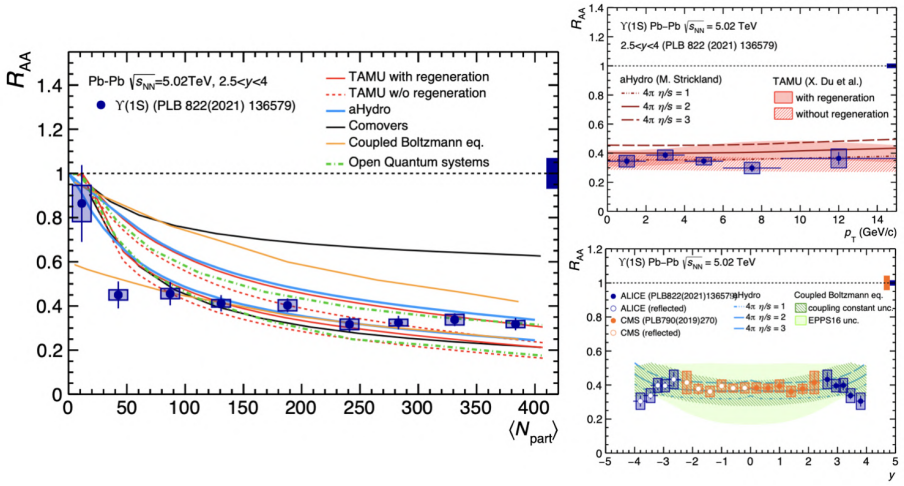

Figure A.3: In the left panel of the picture is reported the nuclear modification factor for inclusive $\Upsilon(1S)$ as a function of N_{part}, compared to calculation; in the right panel the inclusive $\Upsilon(1S)$ nuclear modification factor is reported as a function of the transverse momentum and rapidity, compared to calculations.

From the data collected at the LHC, it is evident that Υ states are suppressed (figure A.3, left), as pronounced as their binding energy is large[27]. Measurements performed by ALICE of R_{AA} as a function of $\langle N_{part} \rangle$ suggests a prompt set in of the suppression of Υ(1S) already in semi-peripheral collisions. R_{AA} is also analysed in function of rapidity and transverse momentum (figure A.3, right)[28]: the p_T dependence is very weak, as well as the rapidity one, which becomes more evident only in the region $3 < y < 4$. What is interesting to notice is that models are able to describe the R_{AA} dependence on rapidity quite well at midrapidity, but they predict the opposite trend at forward rapidity if compared to data. This should be connected to the presence of important regeneration effects, which on the other hand has never been observed (so if they are present, must be small); another process that could lead to the observed behaviour is a significant energy loss causing the shrinking of the rapidity distributions in Pb-Pb collisions: however the models that implement this effect reproduce a smaller decreasing in R_{AA} than observed. For more details on the topic, look at [29].

Appendix B

A deeper insight into NUV-HD-MT SiPM

B.1 NUV-HD-MT SiPM

The NUV-HD-MT SiPMs are a type of sensors belonging to the Low CrossTalk (Low CT) category; they are very common in applications that require minimizing the probability of direct CT, such as in the case of the Cherenkov Telescope Array. The latter must detect the light emitted by cosmic radiation in the atmosphere and require a good Photon Detection Efficiency (PDE) in the range between 300 and 600 nm. The first prototypes included the insertion of a polysilicon layer in the silicon dioxide trench, so that the final structure would be SiO_2-PolySi-SiO_2. This structure offers two benefits: on the one hand, photons attempting to escape from the pixel are reflected back to the cell where they originated; additionally, the polysilicon reduces the transmittance of these photons to adjacent cells. The reduction in Fill Factor is usually compensated by an increase in the applied overvoltage, as shown in figure B.1.

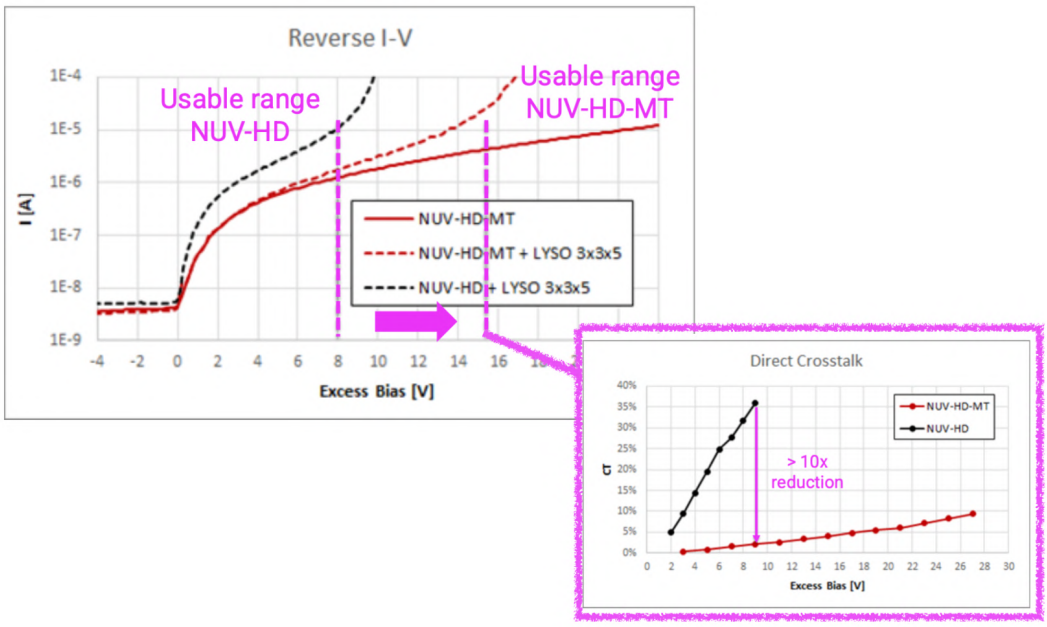

Figure B.1: The typical inverse current curve of NUV-HD-MT category sensors is shown in the figure; a reduction in optical cross talk levels is visible in the zoom.

Even though polysilicon offers a good reduction in photons transmitted to adjacent

cells, the introduction of metallic trenches at the edges of the cells should provide total reflection of the photons, resulting in a further reduction of crosstalk. However, it is difficult to completely eliminate crosstalk because there are countless paths that photons can take to reach neighboring cells.

B.2 More on time resolution for NUV-HD technology

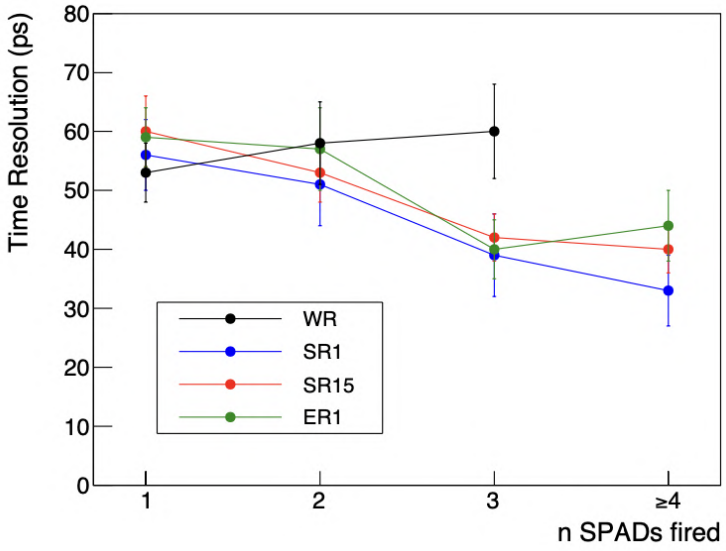

Figure B.2: In the picture the timing resolution is evaluated both for WR sensor and for sensors with the protection layer; the latter shows a better time resolution, improving with the number of SPADs fired; the WR resins sensor show the opposite behaviour [53].

Time Resolution: In figure B.2 time resolution is studied both for sensor with and without resin; the presence of the protection layer leads to value of 30-40 ps, a value that decreases if the number of fired spads increases. For WR sensors the behaviour is different: multi-SPADs events are less probable so, increasing the number of SPADs, they display a different trend, not showing any improvement; however, time performances with only one pixel fired are similar to other SiPM sensors. A possible explanation lies on the fact that in WR sensors multiple SPADs event are only due to CT while in resin-covered SiPMs multi-SPAD events are due to the passage of a charged particle.

Appendix C

More on experimental results

C.1 SiPMs breakdown voltages

This section shows the breakdown values for all analysed sensors; in table C.1 are reported the BD values for the standard NUV-HD sensors, while in table C.2 are reported the NUV-HD-MT prototypes.

Sensor type	*Sensor name*	*Resin*	*BD values (V)*
NUV-HD	SR15D	Silicon	(32.6 ±0.1)
	SR1H		(32.5 ±0.1)
	SR3G		(32.1 ±0.1)
	WR-E	No Resin	(32.7 ±0.1)
	E1C	Epoxy	(32.1 ±0.1)

Table C.1: In the picture are shown the breakdown values for standard NUV-HD sensors analyzed.

Sensor type	*Sensor name*	*Resin*	*BD values (V)*
NUV-HD-MT	B15	Silicon 1.5 mm	(32.9 ±0.1)
	C15		(33.0 ±0.1)
	D15		(32.7 ±0.1)
	B1	Silicon 1 mm	(32.9 ±0.1)
	C1		(33.0 ±0.1)
	D1		(32.9 ±0.1)
	B3	Silicon 3 mm	(32.9 ±0.1)
	C3		(33.0 ±0.1)
	D3		(32.8 ±0.1)
	W63	No resin	(32.9 ±0.1)
	W64		(32.9 ±0.1)

Table C.2: In the picture are shown the breakdown values for NUV-HD-MT sensors analyzed.

C.2 Digital read-out: LiROC

The Lidar ReadOut Chain (LiROC) is an ASIC chip designed to manage 64 SiPMs through 64 channels, each with its own discriminator and amplifier. The 64 devices are connected to a common cathode, and it is possible to provide 64 independent

$V_{bias,i}$ values starting from a common V_{bias}. In each channel, a small programmable offset can be set on the anode, which adjusts the $V_{bias,i}$ for the individual sensor. The offset that can be applied to each channel can vary within a range from 395 to 672 mV in 4.4 mV steps, so the SiPMs connected to the various channels must have similar characteristics. Regarding discrimination, 64 independent thresholds can be applied at 17 bits, all with the same sign, so it is not possible to use sensors with opposite polarity. The circuit diagram is shown in figure C.1; the board on which the FPGA is mounted (which contains the settings needed to configure LiROC) can connect two LiROC chips and two picoTDCs, for a total of 128 channels.

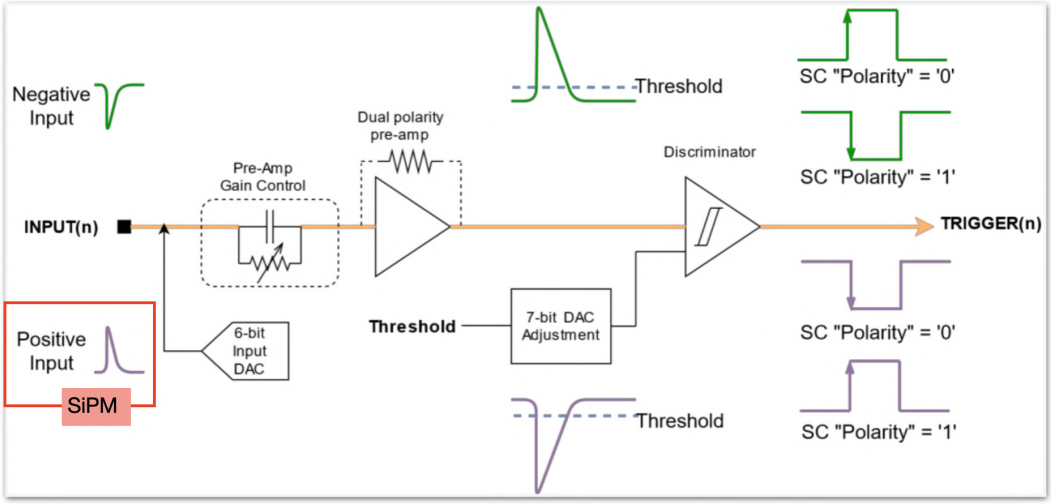

Figure C.1: The readout chain consisting of the discrimination (LiROC) and digitization (picoTDC) is shown in the figure.

The signal digitization is performed by the picoTDC: when a trigger is present, the picoTDC searches back in its memory for a compatible event. However, as shown in figure C.2, a trigger causes a delay, and it is important that the acquisition window is fully contained within the memory.

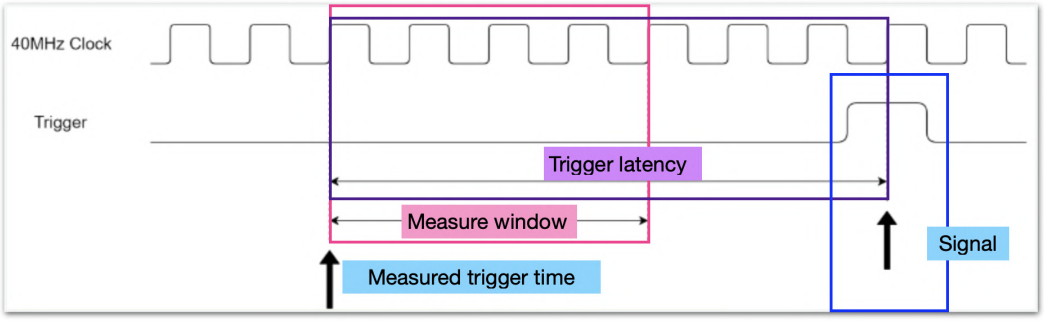

Figure C.2: The memory operation of the picoTDC when a particle passes through is shown in the figure; the acquisition window must be contained in the maximum latency window.

C.2.1 ToT for different channels

In this section, a comparison is made between the different responses of the LiROC channels to the same event. By using a SiPM matrix, consisting of 9 sensors in parallel,

each with an independent output, it is possible to observe the difference in the number of events detected by the various sensors. In figure C.3, we can see that not all sensors detect the same number of events. However, it should also be noted that to align the matrices, the central SiPM was taken as the reference, namely channel 8 and channel 20 of the two devices under study. These two channels, in fact, show a higher number of events. This is particularly evident from the plot in figure C.4, where the Time over Threshold (ToT) does not seem to vary much from channel to channel (although some slight variation is visible), but the main change is in the number of detected events. The fact that the time above the threshold does not show substantial differences is an indication that, by appropriately adjusting the threshold for each channel, it is possible to obtain similar responses from the picoTDC, provided that we are observing channels that behave similarly and do not require setting very different thresholds.

The difference in the number of events becomes more pronounced in figure C.3 as the discrimination threshold increases: the number of detected events is halved when going from a threshold of -30 mV to -40 mV, although we do not observe a substantial difference in the number of events detected when moving to -50 mV, possibly because the threshold was already sufficiently high.

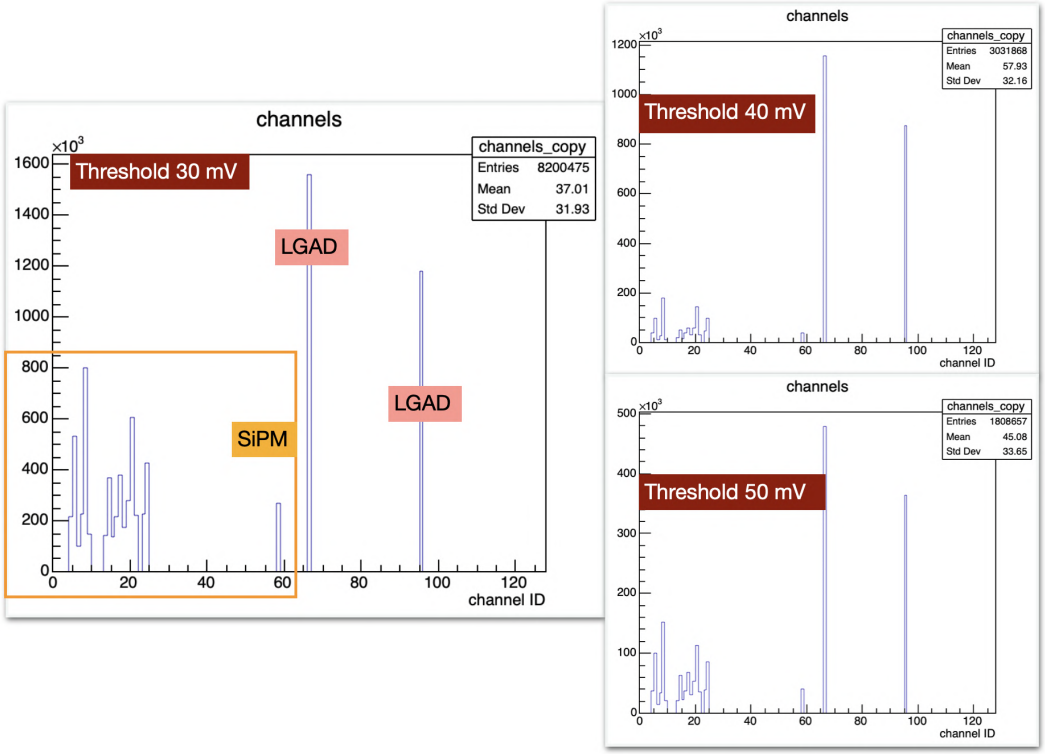

Figure C.3: Response of different LiROC channels to a particle beam of energy 10 GeV/c at varying discrimination threshold for two different SiPM arrays.

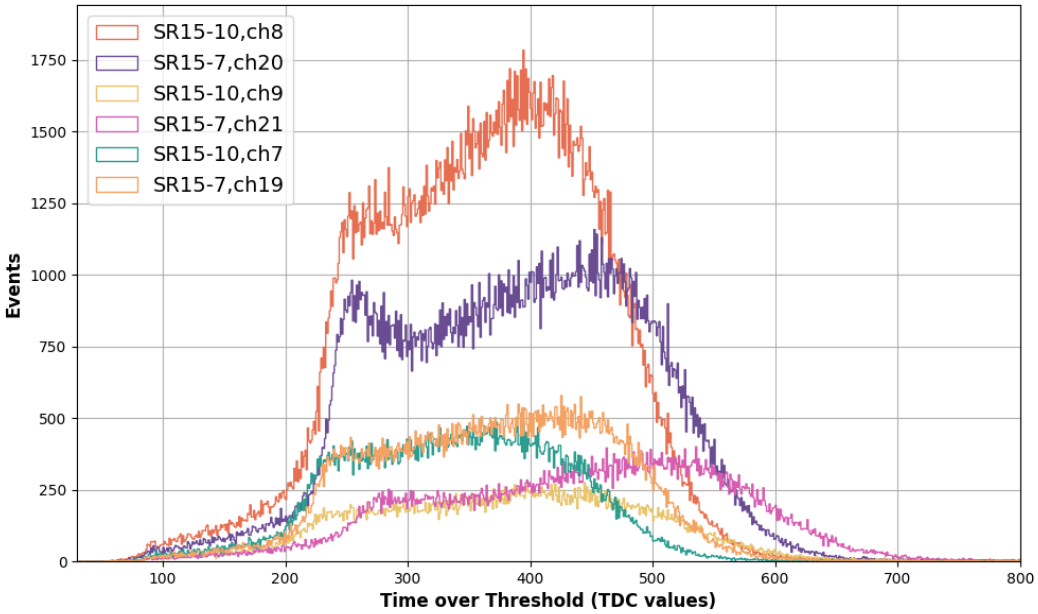

Figure C.4: Time above threshold observed for different channels at a threshold of -30 mV for two different SiPM arrays.

Bibliography

[1] N. Cabibbo and G. Parisi, Exponential Hadronic Spectrum and Quark Liberation, Phys. Lett.B 59 (1975) 6769.

[2] E. V. Shuryak, Theory of Hadronic Plasma, Sov. Phys. JETP 47 (1978) 212219.

[3] HotQCD Collaboration, A. Bazavov et al., Equation of state in (2+1)-flavor QCD, Phys. Rev. D 90 (2014) 094503, arXiv:1407.6387 [hep-lat].

[4] S. Borsanyi, Z. Fodor, C. Hoelbling, S. D. Katz, S. Krieg & K. K. Szabo, Phys. Lett.B730, 99 (2014),arXiv:1309.5258.

[5] HotQCD Collaboration, A. Bazavov et al.,Phys. Rev. D90, 094503 (2014)arXiv:1407.6387.

[6] D. Oliinychenko, L.-G. Pang, H. Elfner, and V. Koch, Microscopic study of deuteron production in Pb-Pb collisions at $\sqrt{s_{NN}} = 2.76\ TeV$ via hydrodynamics and a hadronic afterburner, Phys. Rev. C 99 (2019) 044907, arXiv:1809.03071 [hep-ph].

[7] X. Xu and R. Rapp, Production of Light Nuclei at Thermal Freezeout in Heavy-Ion Collisions, Eur. Phys. J. A 55 (2019) 68, arXiv:1809.04024 [nucl-th].

[8] V. Vovchenko, K. Gallmeister, J. Schaffner-Bielich, and C. Greiner, Nucleosynthesis in heavy-ion collisions at the LHC via the Saha equation, Phys. Lett. B 800 (2020) 135131, arXiv:1903.10024 [hep-ph].

[9] A. Andronic, P. Braun-Munzinger, K. Redlich, and J. Stachel, Decoding the phase structure of QCD via particle production at high energy, Nature 561 (2018) 321330, arXiv:1710.09425 [nucl-th].

[10] F. Becattini, M. Bleicher, T. Kollegger, T. Schuster, J. Steinheimer, and R. Stock, Hadron Formation in Relativistic Nuclear Collisions and the QCD Phase Diagram Phys. Rev. Lett. 111 (2013) 082302, arXiv:1212.2431 [nucl-th].

[11] J. Steinheimer, J. Aichelin, and M. Bleicher, Nonthermal p/π Ratio at LHC as a Consequence of Hadronic Final State Interactions, Phys. Rev. Lett. 110 (2013) 042501, arXiv:1203.5302 [nucl-th].

[12] P. Alba, V. Vovchenko, M. Gorenstein, and H. Stoecker, Flavor-dependent eigenvolume interactions in a hadron resonance gas, Nucl. Phys. A 974 (2018) 2234, arXiv:1606.06542 [hep-ph].

[13] C. Bierlich, G. Gustafson, L. Lönnblad, and A. Tarasov, Effects of Overlapping Strings in pp Collisions, JHEP 03 (2015) 148, arXiv:1412.6259 [hep-ph].

[14] J. Cleymans, P. M. Lo, K. Redlich, and N. Sharma, Multiplicity dependence of (multi)strange baryons in the canonical ensemble with phase shift corrections, Phys. Rev. C 103 (2021) 014904, arXiv:2009.04844 [hep-ph].

[15] ALICE Collaboration, S. Acharya et al., Anisotropic flow of identified particles in Pb-Pb collisions at $\sqrt{s_{NN}} = 5.02\ TeV$, JHEP 09 (2018) 006, arXiv:1805.04390 [nucl-ex].

[16] R. Fries, B. Muller, C. Nonaka, and S. Bass, Hadronization in heavy-ion collisions: Recombination and fragmentation of partons, Phys. Rev. Lett. 90 (2003) 202303, arXiv:nucl-th/0301087.

[17] W. Zhao, C. M. Ko, Y.-X. Liu, G.-Y. Qin, and H. Song, Probing the Partonic Degrees of Freedom in High-Multiplicity p-Pb collisions at $\sqrt{s_{NN}} = 5.02\ TeV$, Phys. Rev. Lett. 125 (2020) 072301, arXiv:1911.00826 [nucl-th].

[18] A. Andronic, P. Braun-Munzinger, M. K. Köhler, A. Mazeliauskas, K. Redlich, J. Stachel, and V. Vislavicius, The multiple-charm hierarchy in the statistical hadronization model, JHEP 07 (2021) 035, arXiv:2104.12754 [hep-ph].

[19] ALICE Collaboration, S. Acharya et al., Measurement of prompt D+s -meson production and azimuthal anisotropy in PbPb collisions at $\sqrt{s_{NN}} = 5.02\ TeV$, Phys. Lett. B 827 (2022) 136986, arXiv:2110.10006 [nucl-ex].

[20] ALICE Collaboration, S. Acharya et al., Constraining hadronization mechanisms with Λ_c^+ / D_0 production ratios in Pb-Pb collisions at $\sqrt{s_{NN}} = 5.02\ TeV$, arXiv:2112.08156 [nucl-ex].

[21] ALICE Collaboration, S. Acharya et al., Λ_c^+ production in pp and in p-Pb collisions at $\sqrt{s_{NN}} = 5.02\ TeV$, Phys. Rev. C 104 (2021) 054905, arXiv:2011.06079 [nucl-ex].

[22] ALICE Collaboration, S. Acharya et al., Λ_c^+ Production and Baryon-to-Meson Ratios in pp and p-Pb Collisions at $\sqrt{s_{NN}} = 5.02\ TeV$ at the LHC, Phys. Rev. Lett. 127 (2021) 202301, arXiv:2011.06078 [nucl-ex].

[23] ALICE Collaboration, S. Acharya et al., Measurement of D_0 , D^+ , D^{*+} and D_s^+ production in pp collisions at $\sqrt{s_{NN}} = 5.02\ TeV$ with ALICE, Eur. Phys. J. C 79 (2019) 388, arXiv:1901.07979 [nucl-ex].

[24] ALICE Collaboration, S. Acharya et al., Measurement of beauty and charm production in pp collisions at $\sqrt{s_{NN}} = 5.02\ TeV$ via non-prompt and prompt D mesons, JHEP 05 (2021) 220, arXiv:2102.13601 [nucl-ex].

[25] ALICE Collaboration, Measurements of inclusive J/Ψ production at midrapidity and forward rapidity in Pb-Pb collisions at $\sqrt{s_{NN}} = 5.02\ TeV$, to be submitted to Phys. Lett. B.

[26] M. Spousta and B. Cole, Interpreting single jet measurements in Pb + Pb collisions at the LHC, Eur. Phys. J. C 76 (2016) 50, arXiv:1504.05169 [hep-ph].

[27] S. Digal, P. Petreczky, and H. Satz, Quarkonium feed down and sequential suppression, Phys. Rev. D64 (2001) 094015, arXiv:hep-ph/0106017 [hep-ph].

[28] ALICE Collaboration, S. Acharya et al., Υ production and nuclear modification at forward rapidity in PbPb collisions at $\sqrt{s_{NN}} = 5.02\ TeV$, Phys. Lett. B 822 (2021) 136579, arXiv:2011.05758 [nucl-ex].

[29] ALICE Collaboration, The ALICE experiment A journey through QCD, arXiv:2211.04384 [nucl-ex].

[30] R. J. Fries, B. Muller, C. Nonaka, and S. A. Bass, Hadron production in heavy-ion collisions: Fragmentation and recombination from a dense parton phase, Phys. Rev. C 68 (2003) 044902, arXiv:nucl-th/0306027.

[31] ALICE Collaboration, B. Abelev et al., Production of charged pions, kaons and protons at large transverse momenta in pp and PbPb collisions at $\sqrt{s_{NN}} = 2.76\ TeV$, Phys. Lett. B 736 (2014) 196207, arXiv:1401.1250 [nucl-ex].

[32] C. Shen, U. Heinz, P. Huovinen, and H. Song, Radial and elliptic flow in Pb+Pb collisions at the Large Hadron Collider from viscous hydrodynamic, Phys. Rev. C 84 (2011) 044903, arXiv:1105.3226 [nucl-th].

[33] V. Minissale, F. Scardina, and V. Greco, Hadrons from coalescence plus fragmentation in AA collisions at energies available at the BNL Relativistic heavy-ion Collider to the CERN Large Hadron Collider, Phys. Rev. C 92 (2015) 054904, arXiv:1502.06213 [nucl-th].

[34] ALICE Collaboration, J. Adam et al., $K_0^*(892)$ and $\phi(1020)$ meson production at high transverse momentum in pp and PbPb collisions at $\sqrt{s_{NN}} = 2.76\ TeV$, Phys. Rev. C 95 (2017) 064606, arXiv:1702.00555 [nucl-ex].

[35] CMS Collaboration, A. M. Sirunyan et al., The production of isolated photons in PbPb and pp collisions at $\sqrt{s_{NN}} = 5.02\ TeV$, JHEP 07 (2020) 116, arXiv:2003.12797 [hep-ex].

[36] ALICE Collaboration, S. Acharya et al., Production of Λ and K_0^s in jets in p-Pb collisions at $\sqrt{s_{NN}} = 5.02\ TeV$ and pp collisions at $\sqrt{s} = 7\ TeV$, Phys. Lett. B 827 (2022) 136984, arXiv:2105.04890 [nucl-ex].

[37] Letter of intent for ALICE 3: A next-generation heavy-ion experiment at the LHC https://arxiv.org/abs/2211.02491

[38] Stefan Gundacker and Arjan Heering 2020 Phys. Med. Biol. 65 17TR01 The silicon photomultiplier: fundamentals and applications of a modern solid-state photon detector

[39] Acerbi F, Ferri A, Gola A, Cazzanelli M, Pavesi L, Zorzi N and Piemonte C 2014 Characterization of single-photon time resolution: From single SPAD to silicon photomultiplier IEEE Trans. Nucl. Sci. 61 267886

[40] Acerbi F, Ferri A, Zappala G, Paternoster G, Picciotto A, Gola A, Zorzi N and Piemonte C 2015 NUV silicon photomultipliers with high detection efficiency and reduced delayed correlated-noise IEEE Trans. Nucl. Sci. 62 131825

[41] Maes W, Meyer K D and Overstraeten R V 1990 Impact ionization in silicon: a review and update Solid-State Electronavailable online

[42] Seifert S, van Dam H T, Huizenga J, Vinke R, Dendooven P, Löhner H and Schaart D R 2009 Simulation of silicon photomultiplier signals IEEE Trans. Nucl. Sci. 56 372633

[43] Grodzicka-Kobylka M, Moszynski M and Szczesniak T 2019 Silicon photomultipliers in gamma spectroscopy with scintillators Nucl. Instrum. Methods Phys. Res. A 926 12947

[44] Klanner R 2019 Characterisation of SiPMs Nucl. Instrum. Methods Phys. Res. available online

[45] Nemallapudi M V, Gundacker S, Lecoq P and Auffray E 2016 Single photon time resolution of state of the art SiPMs J. Instrum.M.V. Nemallapudi et al 2016 JINST 11 P10016

[46] Moll M 1999 Radiation damage in silicon particle detectors PhD Thesis Hamburg University (DESYTHESIS-1999-040)

[47] Gola, A.; Acerbi, F.; Capasso, M.; Marcante, M.; Mazzi, A.; Paternoster, G.; Piemonte, C.; Regazzoni, V.; Zorzi, N. NUV-Sensitive Silicon Photomultiplier Technologies Developed at Fondazione Bruno Kessler. . Sensors 2019, 19, 308

[48] Piemonte, C.; Acerbi, F.; Ferri, A.; Gola, A.; Paternoster, G.; Regazzoni, V.; Zappala, G.; Zorzi, N. Performance of NUV-HD silicon photomultiplier technology. IEEE Trans. Electron Devices 2016, 63, 11111116. CrossRef

[49] Vinogradov, S.; Arodzero, A.; Lanza, R.C.; Welsch, C.P. SiPM response to long and intense light pulses. Nucl. Instrum. Methods Phys. Res. Sect. A 2015, 787, 148152

[50] Zappalà, G.; Acerbi, F.; Ferri, A.; Gola, A.; Paternoster, G.; Zorzi, N.; Piemonte, C. Set-up and methods for SiPM Photo-Detection Efficiency measurements. J. Instrum. 2016, 11, P08014. CrossRef

[51] Silicon Photomultipliers (SiPM). Available online

[52] Nemallapudi, M.V.; Gundacker, S.; Lecoq, P.; Auffray, E.; Ferri, A.; Gola, A.; Piemonte, C. Sub-100 ps coincidence time resolution for positron emission tomography with LSO: Ce codoped with Ca. Phys. Med. Biol. 2015, 60, 4635. CrossRef

[53] Understanding the direct detection of charged particles with SiPMshttps://arxiv.org/abs/2210.13244

[54] Carnesecchi, F., Sabiu, B., Strazzi, S. et al. Measurements of the Cherenkov effect in direct detection of charged particles with SiPMs. Eur. Phys. J. Plus 138, 788 (2023).

[55] https://eu.mouser.com/datasheet/2/400/z

[56] https://download.tek.com/manual/6487-901-01(B-Mar2011)(Ref).pdf

[57] arXiv:1605.01692v1 [physics.ins-det] 4 May 2016

[58] https://www.keysight.com/it/en/assets/7018-04256/data-sheets/5991-3890.pdf

[59] https://contentnktphotonics.s3-eu-central-1.amazonaws.com/Datasheets/PILAS/ALS Pilas DX.pdf?1632838010

[60] https://pdf.directindustry.com/pdf/standa/manual-translation-rotation-stages/35170-558253.html

[61] LabVIEWTM User Manual, National Instruments, 2003

[62] https://www.mouser.com/ProductDetail/Mini-Circuits/LEE-39%2B?qs=xZ%2FP%252Ba9zWqYZp5ZwZPFuXg%3D%3D&srsltid=AfmBOopjEnSTBfWcGHdCKwS_f8fQhsNVVXjhvUQ1ACxdwMIuDWbctLQH

[63] https://docs.rs-online.com/035e/0900766b8127e31c.pdf

[64] Groom, D.E., Klein, S.R. Passage of particles through matter. Eur. Phys. J. C 15, 163173 (2000).

[65] https://www.weeroc.com